SYNTHETIC POLYSACCHARIDE-MEDIATED BIOMIMETIC SYNTHESES OF INORGANIC MATERIALS

A Dissertation

Presented to the Faculty of the Graduate School

of Cornell University

In Partial Fulfillment of the Requirements for the Degree of

Doctor of Philosophy

by

Chao Zhong

August 2009

SYNTHETIC POLYSACCHARIDE-MEDIATED BIOMIMETIC SYNTHESES OF INORGANIC MATERIALS

Chao Zhong, Ph.D.

Cornell University 2009

Despite the importance of polysaccharides in biomineralization, their specific roles are not well understood and they have received very little attention in studies of biomimetic mineralization and the synthesis of biomimetic materials. The experiments reported in this dissertation were designed to advance the knowledge and understanding of the role of acid polysaccharides in biomineralization and biomimetic materials.

In the first experiment, maleic chitosan was synthesized using methanesulfonic/tolunesulfonic chitosan salts as organic-soluble precursors either in formamide or DMSO. The acid polysaccharide was then used as an organic template for the biomimetic mineralization of calcium carbonate.

Amorphous calcium carbonate (ACC) films were produced and stabilized in the presence of maleic chitosan. The films were formed through a process of colloidal self-organization, with nanoparticles less than 10nm being responsible for the self-organization. This study may provide insights into how ACC films are formed in the presence of additive/template systems and contribute to the understanding of biological mechanisms in ACC stabilization.

It was also found that maleic chitosan-mediated $CaCO_3$ spherulites with amorphous cores were obtained through a two-step process: First, ACC films were formed from which amorphous nanoparticles were deposited and stabilized to form

ACC cores. The cores then acted as nuclei for the radial growth of needle-like calcite subunits. The crystals thus combine the coexistence of calcite and ACC found in composite skeletal elements and the radially-ordered structure of spherulitic biominerals. These findings may provide new insights into spherulitic crystallization, particularly the formation of spherulitic biominerals in nature and lead to increased understanding and potential treatment of diseases in which amorphous cores have already been observed in spherulites, such as Alzheimer's disease and kidney stones.

In the second experiment, maleic chitosan-based hydrogels were prepared via photopolymerization and used as an organic matrix template for the growth of carbonated hydroxyaptite. Porous bonelike biocomposites were produced by using maleic chitosan/PEGDA hydrogels as 3D templates in conjunction with a modified simulated body fluid (SBF) mineralization approach. The study suggested that maleic chitosan-based hydrogel not only provides reactive sites for the binding of mineral phase, but also plays an important role in stabilizing amorphous inorganic nanophase at the early stage. It also implies that polysaccharide macromolecules, particularly acid polysaccharides like maleic chitosan, are potential scaffolds for the design of new bonelike biocomposites.

BIOGRAPHICAL SKETCH

Chao Zhong is a Ph.D. candidate in Fiber Science Program in the Department of Fiber Science and Apparel Design at Cornell University in Ithaca, NY. His Ph.D. advisor is Professor C. C. Chu. Prior to Cornell, Chao Zhong received his Bachelor in Materials Science and Engineering (MSE) from Tianjin University in 2001 and Master degree in Materials Science (Polymer science) from Beijing University of Chemical Technology in 2004. His Ph.D. research work focuses primarily on development of polysaccharide-based biomaterials, and using synthetic polysaccharides as organic templates for biomimetic mineralization of inorganic minerals. After receiving his Ph.D., he will assume a postdoctoral position at University of Washington, Seattle in the field of bionanotechnology, where he will focus on the development of bioinspired nanomaterials for biological sensing and green energy production.

To My Wife, Parents and Sisters

ACKNOWLEDGMENTS

My advisor, Professor Chin-Chang Chu, has provided me general guidance and support throughout my graduate studies at Cornell. Without his support, this work would not have been possible, and it has been a privilege to learn and to conduct biomaterials research in his laboratory. I am particularly grateful for the freedom and encouragement he gave me to explore my other research interests in biomineralization and the synthesis of biomimetic materials.

For mentoring me in these other research interests, I am deeply indebted to Professor Lara A. Estroff , who also permitted me to attend meetings of her own research group and met privately with me on several occasions to discuss my ongoing research. I particularly appreciate her warmth, her encouragement, and her accessibility to a graduate student who was not officially "hers."

I also deeply appreciate my other committee members, Professors Anil Netravali and Larry Bonassar for the suggestions and help they have given me.

The technical assistance from CCMR at Cornell University has been invaluable for the completion of my work: Dr. Mick Thomas trained me to use KECK SEM; Dr. Maura Weathers taught me to use XRD; Anthony Condo has taught me for NMR test, John Grazul provided me with full training and assistance in Microtomy and TEM.

I should also like to acknowledge earlier mentors: my undergraduate advisor, Professor Xubo Yuan at Tianjin University, who sparked my initial research interest in biomaterials; and my former advisors, Professor Ming-zhi Huang and Professor Jin Zhao, at Beijing University of Chemical Technology who guided my research in biopolymers.

I should also like to acknowledge my friends and fellow graduate students in both Professor Chu's and Professor Estroff's groups: Kai Guo, Guoming Sun, Mingxiao Deng, Hua Song, Jun Wu, Patti Lewis, Xuan Pang, Mingyu He, Hanying Li, Jason Dorvee, Ellen Keene, and others who provided help and suggestions.

Several friends outside of Cornell have made my studies and life in Ithaca enjoyable. Special gratitude goes to Professor Daryl Bem, a family friend who also provided useful guidance in scientific writing—including this dissertation.

The research work was partially supported by graduate student thesis funds from the College of Human Ecology at Cornell University and the Morgan Tissue Engineering Program.

Finally, my deepest love and sincerest gratitude go to my wife, my parents, and my two elder sisters. Without their love, support, understanding, and encouragement, I could not have begun and sustained my adventurous Ph.D. journey abroad. Their unwavering presence in everything I take on makes this long trip all worth it.

TABLE OF CONTENTS

LIST OF FIGURES

LIST OF TABLES

LIST OF SCHEMES

CHAPTER 1

INTRODUCTION: BIOMINERALIZATION AND THE SYNTHESIS OF BIOMIMETIC MATERIALS

The research reported in this dissertation was designed to contribute to two major goals: (1) Understanding the roles of acid polysaccharides on $CaCO_3$ nucleation and growth; and (2) achieving progress in the synthesis of biomimetic materials, with the goal of producing new bonelike biocomposites. This introductory chapter presents background information relevant to the research.

1.1 Biomineralization

The processes used by living organisms to form minerals are collectively called biomineralization. The study of biomineralization is multidisciplinary, spanning both the inorganic and organic fields. The processes of biomineralization are divided into two types based upon their degree of biological control: biologically *induced* mineralization and biologically *controlled* mineralization [1].

1.1.1 Biologically Induced Mineralization

Biologically induced mineralization is defined as the secondary precipitation of minerals that occurs as a result of interactions between biological activity and the environment [1]. Here the biological system generally has little control over the type and behavior of the deposited minerals, and the biological surfaces typically play the important role in the induction of mineral deposits. In some cases, cell surfaces directly serve as the locus for the initial nucleation and subsequent growth of mineral phase [1]. For example, in *Chara,* the crystals directly form in regions of the cell wall

that correspond to areas that are more alkaline [2]. In general, a typical feature of biologically induced mineralization is heterogeneity.

1.1.2 Biologically Controlled Mineralization

Biologically controlled mineralization, sometimes referred to as "organic-matrix mediated" mineralization, is more common in biological systems and produces the more interesting biominerals that have attracted the attention of biologists and material scientists such as bones, mollusk shells and animal teeth. Through this process, biological systems use a variety of strategies to exert control over the type, behavior, and final structures and properties of minerals, with organic macromolecules playing important functions in controlling their biomechanical and other properties.

Depending on their specific functions, macromolecules extracted from biominerals (even those from different taxa) are either functionalized soluble macromolecules or insoluble framework macromolecules. For carbonate and phosphate based minerals, the soluble macromolecules are usually referred to as "acidic macromolecules"; they are commonly rich in aspartic and/or aspartic and glutamic acids and some have phosphorylated serine and threonine residues [1]. Additionally, they often have covalently bound polysaccharides that are also acidic, being rich in carboxylate groups and sometimes sulfate as well [1]. These functionalized macromolecules have been commonly believed to modulate and mediate the nucleation, growth, and morphology of minerals. More recently, however, some researchers have pointed out that certain soluble macromolecules (e.g. proteins rich in glutamic acid and/or glutamine) may contribute to the stabilization of amorphous phase [3, 4]. As we shall see, the stabilization of amorphous calcium carbonate (ACC) as a precursor to several $CaCO_3$ biominerals is particularly central to this dissertation.

In contrast to the soluble macromolecules, the insoluble framework macromolecules vary considerably from one organism to another. This is exemplified by the presence of collagens in natural bone, polysaccharides like chitin and silk-like proteins in mollusk shells, and amelogenins in tooth enamels. They are usually insoluble in water and may provide microenvironments for mineral growth. They may also contribute to the mechanical properties of the formed minerals.

The two types of macromolecules described above are mainly composed of protein- and polysaccharide-based macromolecules, and these proteins and protein components are currently the focus of the most theories of biomineralization. It is a major claim of this dissertation, however, that another type of macromolecule, polysaccharides, may play as much or even more important functions in certain biominerals than has been appreciated so far. The involvement of polysaccharides in biomineralization actually appears very early in evolution [5]. As an example, the microbialites, evidence of some of the oldest life on earth, contain crystalline calcium carbonate minerals(mainly aragonite crystals) embedded in a polysaccharide-enriched organic matrix [5]. The following sections provide the relevant background about the polysaccharides and their possible roles in biomineralization.

1.2. Polysaccharides in biominerals

1.2.1 Polysaccharide Chitin

The most common polysaccharide associated with biominerals is chitin, a linear polysaccharide containing chains of β (1-4) 2-acetamido-2 -deoxy-D-glucopyranose residues [6, 7]. Although the occurrence of chitin is not necessarily associated with biominerals, its presence is crucial in biominerals, such as crustacean shells, carapaces and gastroliths, and mollusks shells [8]. Chitin exists as an insoluble organic component in many minerals of different biological systems and is observed in

two major forms, alpha-chitin and belta-chitin. Alpha-chitin chains show an antiparallel configuration in the *c*-axis, thereby having a highly ordered orthorhombic crystalline structure with extensive three-dimensional hydrogen bonding that gives rise to the rigid and insoluble properties of the polymer. Belta-chitin has a monoclinic crystal structure with a parallel polymer chain arrangement which does not favor the formation of along the *c*-axis but interchain hydrogen bonding between the C-6 hydroxyl groups does facilitate the incorporation of water molecules between the weakly interacting chains. Although the functions of chitin may vary from one species to another, it is generally believed to serve as an insoluble matrix for mineral deposition, to assist the orientation of minerals, and to strengthen their mechanical properties.

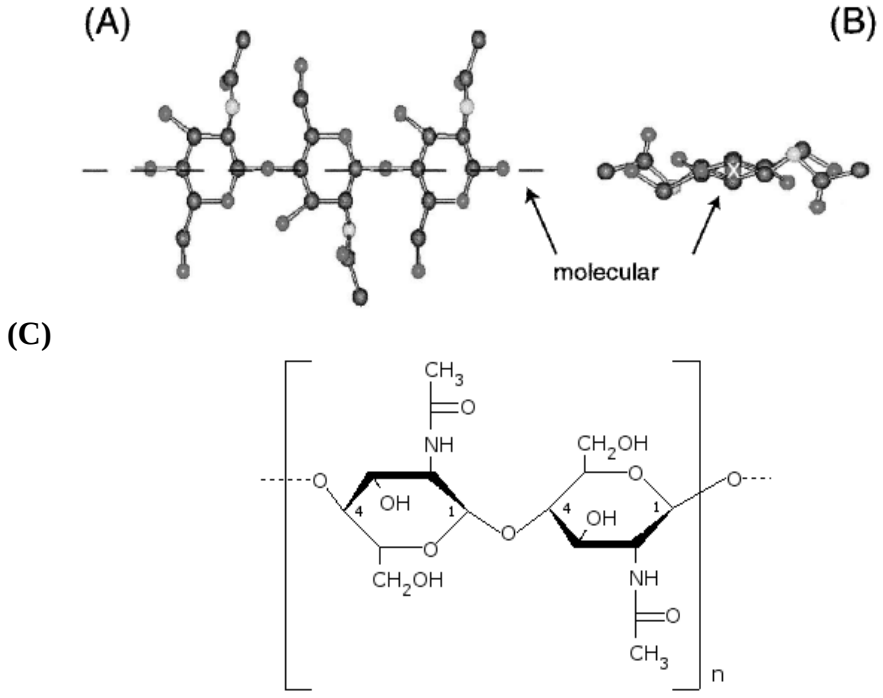

Figure 1.1 Schematic representation of the β (1-4) 2-acetamido-2-deoxy-D-glucopyranose residue, which constitutes the biopolymer chitin. The molecule is shown along two directions: (**A**) view normal to the molecular axis; (**B**) view along the molecular axis; (**C**) chemical structure of chitin (Reproduced from reference 6).

Chitin has been commonly found in association with calcium carbonate biominerals and, occasionally, apatite biominerals (e.g., the shell of Lingula unguis [9]). For example, the shell of the pink shrimp Pandalus borealis has a matrix of α-chitin associated with amorphous calcium carbonate [10]. The chitin is an integral part of the crystallized regions and therefore probably plays an important role in the deposition of calcium carbonate. In the nacre mollusk shell, the mineral phase forms inside a preformed organic matrix. The organic matrix is composed of thin layers of β-chitin sandwiched between two thicker layers of silk-like proteins onto which acidic macromolecules rich in aspartic acid are adsorbed [11]. The fiber axes of the chitin and the silk proteins are perpendicular to each other and aligned with the a and b axes of aragonite, one of the polymorphs of calcium carbonate [12]. Falini et al. reviewed chitin biomineralization covering the several known carbonate and phosphate-based biominerals that contain chitin and speculated on the possible roles of chitin in these biominerals [7].

In addition to the occurrence in carbonate and phosphate-based minerals, chitin has also been identified in other types of minerals. For example, the matrix of limpet teeth (composed of goethite crystals, α-FeOOH) consists of relatively well-ordered, densely packed arrays of chitin fibers, with only a few nanometers between adjacent fibers [13]. There are clearly no pre-formed compartments that control goethite crystal size and shape; rather, crystals push aside or engulf the fibers as they grow. These linear deposits of goethite appear to nucleate on the chitin fibers, thereby controlling the orientation of the crystals. In another study, Ehrlich et al. showed that chitin is a component of the outermost layer (cuticle) of the skeletal fibers of the demosponges by probing the internal proteinaceous (sponging) skeleton of two demosponges (Aplysina sp. and Verongula gigantea) [14]. FTIR, Raman spectra, and X-ray diffractograms consistently revealed that sponge chitin is much closer to the α-chitin

known from other animals than it is to β-chitin [14].

1.2.2 Acid Polysaccharides

One of the well-documented systems with respect to the association of acid polysaccharides with biominerals was based upon extensive studies on Pleurochrysis coccoliths, unicellular marine algae [15]. In this organism, 24 interlocking calcite crystals are assembled on the distal rim of an oval organic baseplate, and this construct is designated a cocolith (Figure 1.2). The initial crystallites appear to be tethered on the cocolith ribbon, which is composed of acid polysaccharides. The ribbon appears not as a filament but as a two dimensional band that probably serves as the site for calcite nucleation. Detailed information about the structures and biomineralization processes of coccolith can be found in several review articles [15-17].

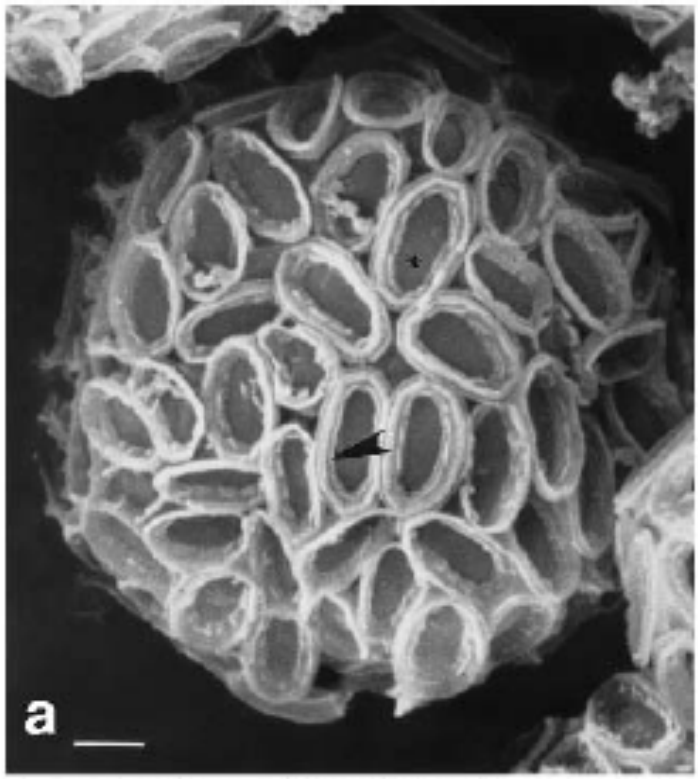

Figure 1.2. Cocolith structure (Reproduced from reference 14)

Three types of acid polysaccharides (labeled PS-1, PS-2 and PS-3) have been isolated and identified in *Pleurochrysis carterae*. PS-1 is a polyalduronic polymer that contains only a few uncharged glycosyl residues and has mainly alternating residues of D-glucuronic acid and D-galacturonic acid in a ratio of 1:3. PS-2 is the most abundant polysaccharide, composed of repeating sequences of D-glucuronic, *meso*-tartaric, and glyoxylic acids (Figure 1.3). PS-3, which makes up less than 2% of the *coccolith* polyanions and is predominantly a sulphated polymer of galacturonic acid. There are many other acidic polysaccharides reported in coccoliths whose chemical structures remain unknown [18].

The functions of these polysaccharides have also been assessed. PS-1 and PS-2 were found to be involved in ion accumulation and may have important roles in directing the deposition of calcite nanocrystals in the correct orientation to the base plate rim [19]. PS-3 was found to be localized at the interface between the first crystallites and the membrane of the mineralizing vesicle and was believed to be responsible for acquiring anvil-like crystals by growth of the first crystallites. Therefore, PS-3 may play important roles in crystal growth and shaping [20].

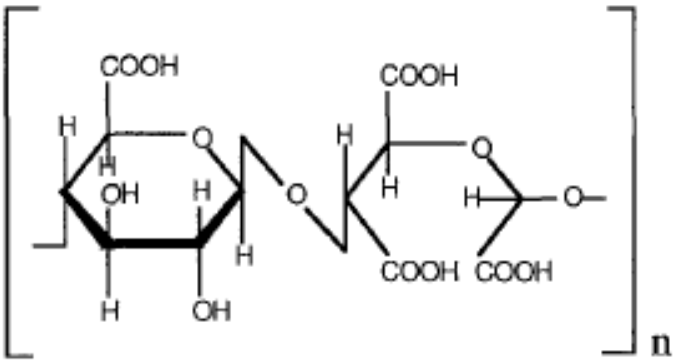

Figure 1.3. Chemical structure of the mineral-associated algal polysaccharide PS-2 (Reproduced from reference 17)

The occurrences of acid polysaccharides in $CaCO_3$ biominerals are by no means limited only to coccoliths. For example, using x-ray and electron microscopy, Benzerara el al. found that lake van microbialites are composed of living and/or fossilized microbes and nonbacterial-like aragonite crystals embedded together in a polysaccharide matrix [5]. Their observations suggest that the presence of the polysaccharide-based matrix—intimately associated with the aragonite crystals down to the nanometer scale—is responsible for the particular mineralogical features observed in Lake Van microbialites, i.e., clustered spherical aragonite crystals in the 30-to 100-nm size range, surrounded by biogenic organic phase-stabilized ACC phase. In earlier work from the same group, ACC was observed around nanometer-sized rodshaped calcite crystals surrounded by polysaccharides [21, 22], although their mechanism of formation and the exact functions of the organic phases remain to be explained.

The observations of acid polysaccharides involved in minerals can be extended to other non carbonate-based biominerals. For example, Banfield et al. identified an acidic exopolysaccharide other than a polypeptide as a new templating element of bacterial biomineralization [23]. The iron oxyhydroxide-encrusted biofilms, isolated from the surrounding groundwater, were found to comprise many polymer strands (filaments) with minerals located on the outside. Each of these filaments contained a thin, pseudo-single crystal core surrounded by a porous layer of nanocrystalline ferrihydrite (Figure 1.4). The major component of the organic polymer within this core of iron oxide filaments was acid polysaccharide (most likely alginate) and may function as a structure-directing component [23].

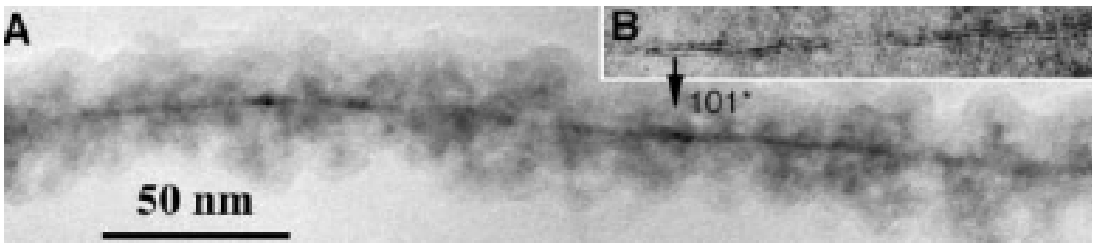

Figure 1.4. HRTEM images of natural FeOOH-mineralized filaments from the biofilm. (**A**) A filament showing overall structure of thin akaganeite core surrounded by amorphous and finely crystalline iron oxyhydroxide (Reproduced from Reference 23)

1.2.3 Other sugar-containing macromolecules

In addition to the pure polysaccharides, other sugar-containing macromolecules in association with biominerals have also been identified. These are usually glycoproteins, molecules that contain oligosaccharide chains (glycans) covalently attached onto the polypeptide backbone chains. When they are heavily glycosylated, glycoproteins are usually referred to as proteoglycans. Proteoglycans have a core protein with one or more covalently attached glycosaminoglycan (GAG) chain(s). The GAG chains are long, linear carbohydrate polymers that are negatively charged due to the occurrence of sulfate and uronic acid groups [24].

Glycoproteins and/or proteglycans exist as very small amounts of organic components (usually as intracrystalline macromolecules) in several $CaCO_3$ biominerals including but not limited to stony corals [25], avian eggshell [26], and sea-urchin larvae [27]. For example, sulfated glycoproteins were found in association with the calcification center of stony corals and are believed to play important roles in early stage mineralization [28], while those found in body spicule may contribute to the stabilization of amorphous calcium carbonate phase [29]. Generally, the chemical

structures of these sugar-containing macromolecules may vary from one species to another, and their specific functions in biominerals are not fully understood.

Table 1.1 Composition of bone organic matrix of vertebrate animals (Reproduced from reference 30)

Organics	Type of organics	100 (% dry weight)
Type I collagen	proteins	88.00
Osteonectin	glycoprotein	3.00
α 2- HS glycoprotein	glycoprotein	2.40
Osteocalcin	Proteins	1.80
Bone Sialoprotein		1.20
Osteopontin	glycoprotein	0.96
Decorin	Proteoglycan	0.84
Biglycan	Proteoglycan	
Micelles:		1.980
Dentin matrix Gla protein Matrix Gla Protein Thrombospondin Fibronectin		

Apatite-based biominerals are another important type of biominerals containing glycoproteins and/or proteglycans and are found in bones and teeth of mammals. Table 1.1 shows the major components of organic matrix found in bone [30]. Type I collagen and other non-collagen proteins account for approximately 90%

of the organic content. Accordingly, it is not surprising that they are the focus of most past and current theories about biopolymer-mediated bone mineralization.

In contrast, the glycoproteins and/or proteglycans constitute only a very small amount of the total organic components and have heretofore received very little attention. With the development of advanced analytical techniques, the structures and functions of polysaccharide components in bone minerals are now being more fully investigated. For example, several recent studies, based on *in vitro* [31], genetic[32], biochemical [33] and immunohistochemical methods [34, 35] all indicate that the polysaccharide components are vital in bone formation and in maintaining bone health, with possible roles in modulating mineral size and crystallinity [36].

A particularly pertinent recent study had probed the interface between organic and inorganic phase in equine bone using solid-state NMR (SSNMR) techniques [36]. Wise et al. revealed that molecular constituents of the organic-mineral interface are rich in polysaccharides (most likely glycosaminoglycan (GAG) sugars), rather than proteins as is widely assumed (Figure 1.5) [36]. Similar observations have also been identified at the interface between organic and inorganic phase in horse teeth (Figure 1.6) [37] and other calcified connective tissues, such as calcified atherosclerotic plaque[38] and calcified cartilage [39].

The close association of acidic polysaccharide components with these several phosphate-based minerals raises the possibility that polysaccharides (most likely GAGs) are universal participants in nonpathological formation of calcium- and phosphate-based biominerals in mammals [36]. These findings may alter an accepted concept of bone structural biology and exert a major impact on the pharmacological management of bone disorders as well as providing new strategies for the development of bone-like biomaterials and diagnostic biomarkers for disease.

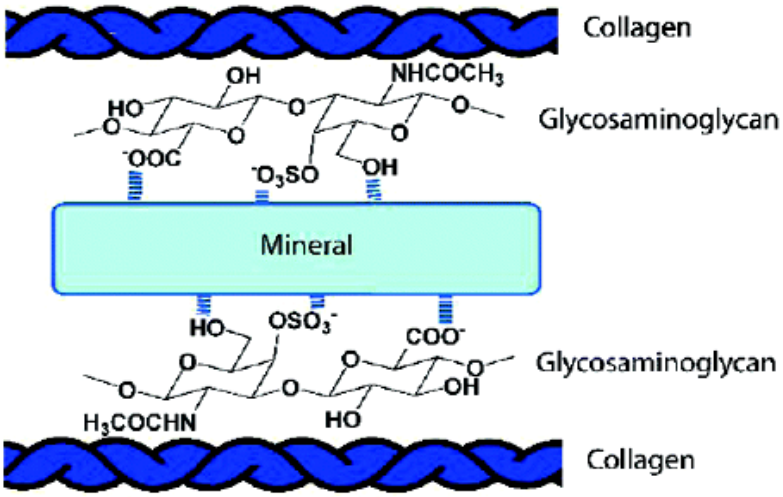

Figure 1.5. Schematic drawing shows that the predominance of polysaccharide (mainly Glycosaminoglycan) exists at the interface of mineral and organic phase in bone (Reproduced from reference 36).

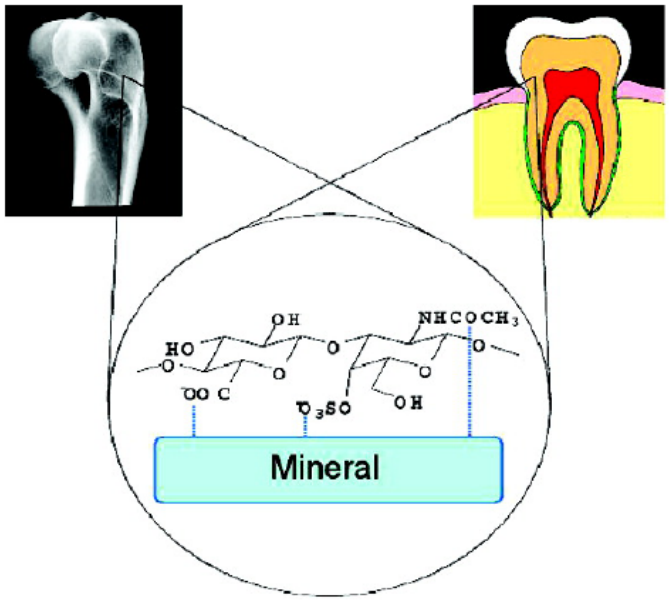

Figure 1.6. Schematic drawing shows that the organic-mineral interphase in teeth is dominated by polysaccharides (Reproduced from reference 37).

1.3 Crystallization through Amorphous Precursor Phases

In addition to organic matrix-mediated mineralization, crystallization that proceeds through an amorphous phase is another important process in biomineralization. The amorphous phase of $CaCO_3$ biominerals is usually referred to as "amorphous calcium carbonate" (ACC), one of the six forms of calcium carbonate under ambient conditions. The other five are all crystalline phases and include calcite, aragonite, vaterite, monohydrocalcite and calcium carbonate hexahydrate, with calcite and aragonite being by far the most widely produced forms of calcium carbonate in biology.[3]

Although unstable in its pure form, ACC can be stabilized and utilized by organisms for different purposes. For example, it can act as storage sites and mechanical supports for certain organisms [4]. It has even been reported that ACC can be used as transient precursors for the two major crystalline phases of $CaCO_3$, calcite and aragonite, with the investigators noting that organic macromolecules are one of the possible elements that may induce and stabilize the formation of biogenic ACC phase [3].

Perhaps the first convincing report to describe a transient ACC phase in biominerals was that by Beniash et al. in 1997, who examined spicule formation in sea urchin larvae [40]. This observation significantly changed the concept of mineral formation in this well-studied organism. Further work from this group has demonstrated that an amorphous precursor was utilized in the regeneration of the adult urchin spine [41], the formation of mollusk larval shell [42] and the teeth of sea urchins [43]. They suggest that deposition of transient amorphous phases may be a useful strategy for producing crystals with complex structures. More detailed information about ACC phase and its major roles in biomineralization and crystallization can be found in several excellent reviews [3, 4, 44].

The concept of an amorphous calcium phosphate precursor in bone formation appeared as early as 1960s [45], but the existing evidence was inconclusive. The recent findings concerning $CaCO_3$ biominerals, however, have sparked interest in searching for an amorphous precursor in the formation of apatite-based biominerals [46]. For example, Mahamid et al. recently identified an amorphous calcium phosphate precursor for fin bones of zebrafish (Figure 1.7) by probing the minerals freshly extracted from the distal end of the fin using TEM and SAED combined with cryo- SEM and ESB imaging techniques (shown in Figure 1.8) [47]. In addition, Beniash et al. showed that the newly formed murine tooth enamel mineral is amorphous calcium phosphate (ACP) that eventually transforms into apatitic crystals (Figure 1.9) [48]. These findings, in conjunction with previous studies on ACC precursors in $CaCO_3$ biominerals, suggest that the amorphous precursor strategy might be universal in the formation of biominerals [48].

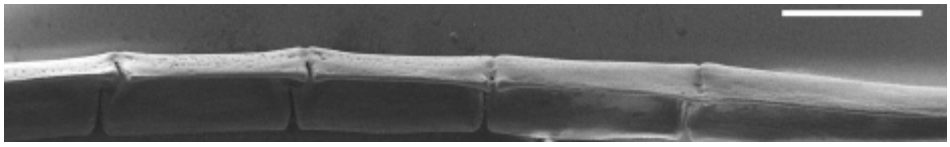

Figure 1.7. SEM image showing the fin bones of zebrafish (Reproduced from reference 47)

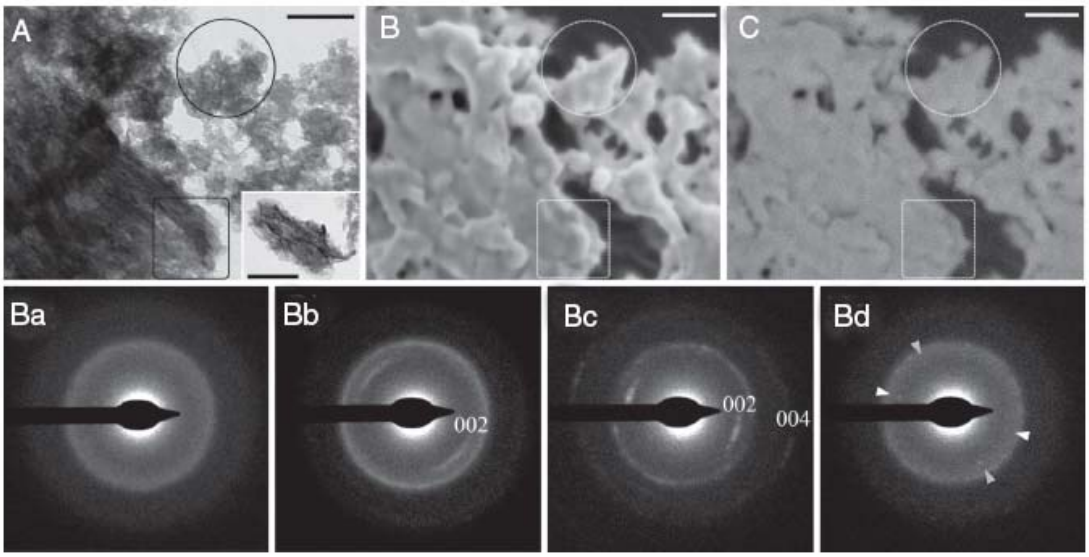

Figure 1.8. TEM and SAED correlated with SEM and ESB imaging of mineral freshly extracted from the distal end of the fin. (*A* and *B*) TEM micrograph of mineral particle aggregates and the corresponding SAED patterns showing amorphous scatter of diffuse rings (SAED, *B.a*). Area marked with a rectangle produces poorly crystalline diffraction (SAED, *B.b*), and particle in *Inset* produces a clear crystalline diffraction pattern (SAED, *B.c*), showing well defined reflections of the (002) and second order (004) apatite planes. SAED *B.d* corresponds to the encircled area examined after storage for 1 week at room temperature: As the particles begin to crystallize, diffraction spots with spacing of the (002) plane appear (arrowheads), implying conversion into a crystalline apatite phase. (*C*) High-resolution cryo-SEM of the same particle after examination in the TEM. (*D*) Corresponding ESB image, showing no distinguishable difference between the amorphous (encircled area) and crystalline (rectangular area) mineral parts (Scale bars 100 nm.) (Reproduced from reference 47).

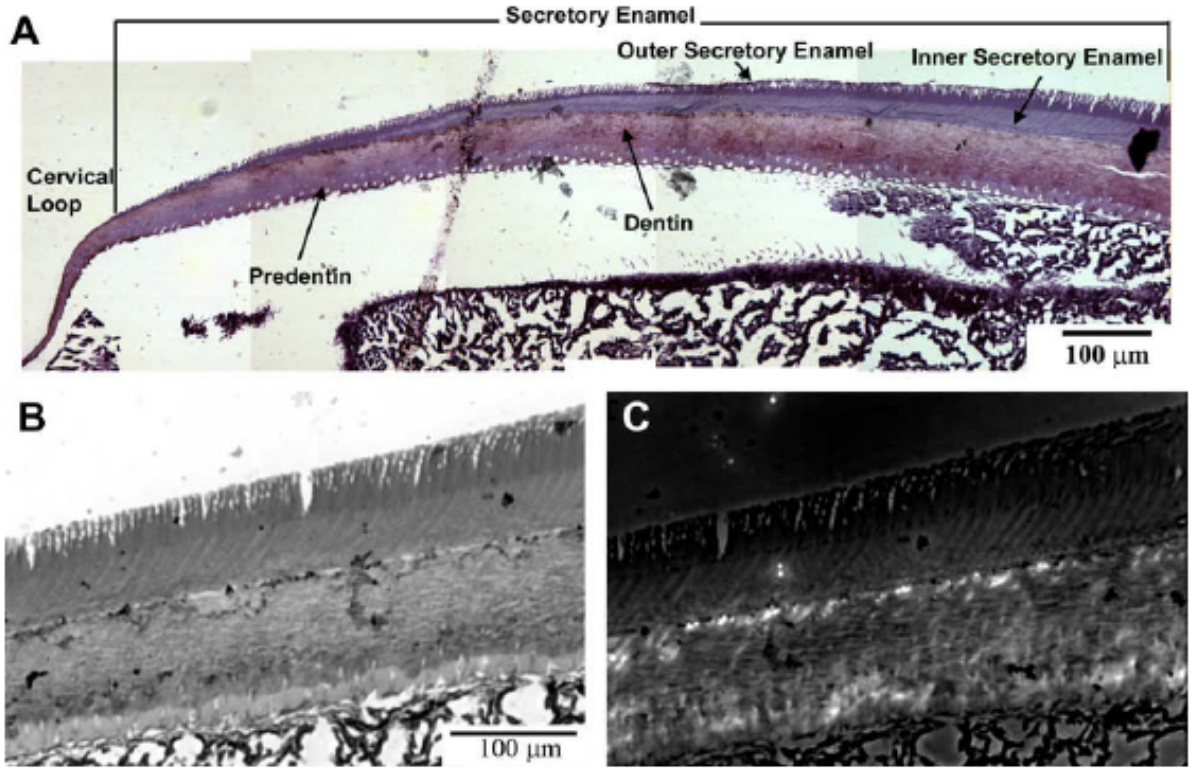

Figure 1.9. Light micrographs of semi-thin section of mouse incisor in the region of cervical loop stained with toluidine blue (A). Note differences in the shades of staining in the outer and inner secretory enamel. Micrographs in the bottom row are taken from the same area in bright field (B) and polarized light (C) modes. Note that the inner enamel layer is slightly birefrigent (Reproduced from Reference 48).

1.4 Biomimetic Materials Synthesis

Biominerals are advanced biogenic composite materials containing both inorganic minerals and organic macromolecules. By studying and understanding how nature constructs biogenic materials, materials scientists have initiated a paradigm shift in modern materials science and technology. For example, one of the important principles of biomineralization is the organic matrix-mediated mineralization. Inspired by this principle, researchers have used a variety of organic macromolecules, templates, and additives to mediate and control the growth and orientation of inorganic minerals, including carbonated apatite, silica, and calcium carbonate.

Several research groups have sought to understand the biomimetic growth of calcium carbonate in particular. For example, in the late 1990s', Aizenberg et al. introduced a new strategy for controlling the density and orientation of inorganic minerals by using micro-patterned self-assembled monolayers (SAMs) as 2-D templates [49-51]. Subsequently, Aizenberg et al. were able to fabricate mm-sized single calcite films via the transformation of metastable ACC films directly on the SAMs [52]. Using a polypeptide as the macromolecule to control $CaCO_3$ crystallization, Gower et al. discovered an unusual crystallization pathway which they called "polymer-induced liquid precursor''[53, 54]. Although the existence of this precursor is still being debated, the *in vitro* work itself provides insights into the stabilization of amorphous calcium carbonate (ACC) and suggests a possible new method for producing biomimetic inorganic materials. Gel-like materials have also been identified in several biominerals including calcium carbonate minerals(e.g. silk fibroin-like proteins in aragonitic nacreous layer of mollusk shells [55]). The Estroff group at Cornell University has recently begun a program for synthesizing bioinspired materials by growing inorganic minerals in gel (e.g. agarose gel) environments [56-59].

Other important work on the biomimetic growth of calcium carbonate include the Colfen group's use of block copolymers(e.g. poly(ethylene oxide)-b-poly(sodium 4-styrenesulfonate)) to control the growth of crystals, in particular mesocrystals (single crystal analogs) [60-62] and the Sommerdijk group's use of a variety of macromolecules including poly(propylene imine) dendrimer [63], Langmuir monolayers [64] and polypeptide analogs [65] as templates for the growth of $CaCO_3$ minerals. Both groups have recently sought to understand early stage crystallization of $CaCO_3$ based on the observation that amorphous calcium carbonate serves as a transient precursor for crystalline phases of $CaCO_3$ [66, 67].

In contrast with the substantial attention to $CaCO_3$, there is less work on the biomimetic synthesis of phosphate-based minerals using organic macromolecules as additives or templates. (This might be due to the difficulty of achieving hydoxyapatite crystallization and growth.) Most of this work is directed to the synthesis of bone-like biocomposites with an eye toward potential bone engineering applications. One of the important contributions is the work of the Stupp group in utilizing self-assembling peptide amphiphile (PA) nanofibers as the template for the growth of nano apatite crystals [68, 69]. Other work includes the use of collagen [70], other peptidic biopolymers such as fibronectin [70], synthetic polymers such as poly(hydroxyacids) (e.g. poly-L-lactic acid [71]), polycaprolactone [72], dendrimers [73] and polymeric hydrogels(e.g. poly(2-hydroxyethyl methacrylate) (pHEMA) hydrogel) [74, 75] as organic templates for the synthesis of apatite-like minerals. The Stupp group has recently reviewed biomimetic systems for hydroxyapatite mineralization [76].

Finally, researchers have utilized similar strategies to produce a variety of inorganic materials and organic/inorganic hybrid composites using proteins and other macromolecules as templates. Naik et al. has recently reviewed protein- and peptide-directed syntheses of inorganic materials [77].

1. 5 Motivations and Goals

As described above, most research efforts on the synthesis of biomimetic materials have focused on the development of novel functional proteins and polypeptide and polymeric protein analogs and their use as templates for the growth of minerals or the synthesis of inorganic materials. More generally, proteins are the major focus of most theories about biomineralization. In contrast, the roles of polysaccharides have received very little attention. This same protein-oriented strategy has also characterized the efforts to synthesize inorganic minerals and to develop biomaterials that might treat bone defects or serve as bone engineering scaffolds.

Despite this neglect, there is increasingly evidence that polysaccharides may play an important role in many biominerals. For example, recent evidence showed that polysaccharides are predominantly present at the organic-mineral interfaces in phosphate-containing minerals (e.g., horse bones and teeth), which may implicate sugar components (mainly GAGs) in maintaining the health of bone [36].

Accordingly, this dissertation is directed toward the development of synthetic polysaccharide templates for the biomimetic syntheses of inorganic materials. The two main goals are:

1) To design and synthesize a synthetic polysaccharide, maleic chitosan, to enable the biomimetic growth of $CaCO_3$ minerals and to use this as an *in vitro* model for understanding the roles of acid polysaccharide in the nucleation, growth, and morphology of biominerals.

2) To design and prepare maleic chitosan/PEGDA hydrogels and to use these hydrogels as templates for the biomimetic synthesis of porous bone-like biocomposites in order to produce potential bone engineering scaffolds.

Scheme 1.1 displays the general strategies and goals of this dissertation.

Scheme 1.1. General Strategies and Goals of this Dissertation

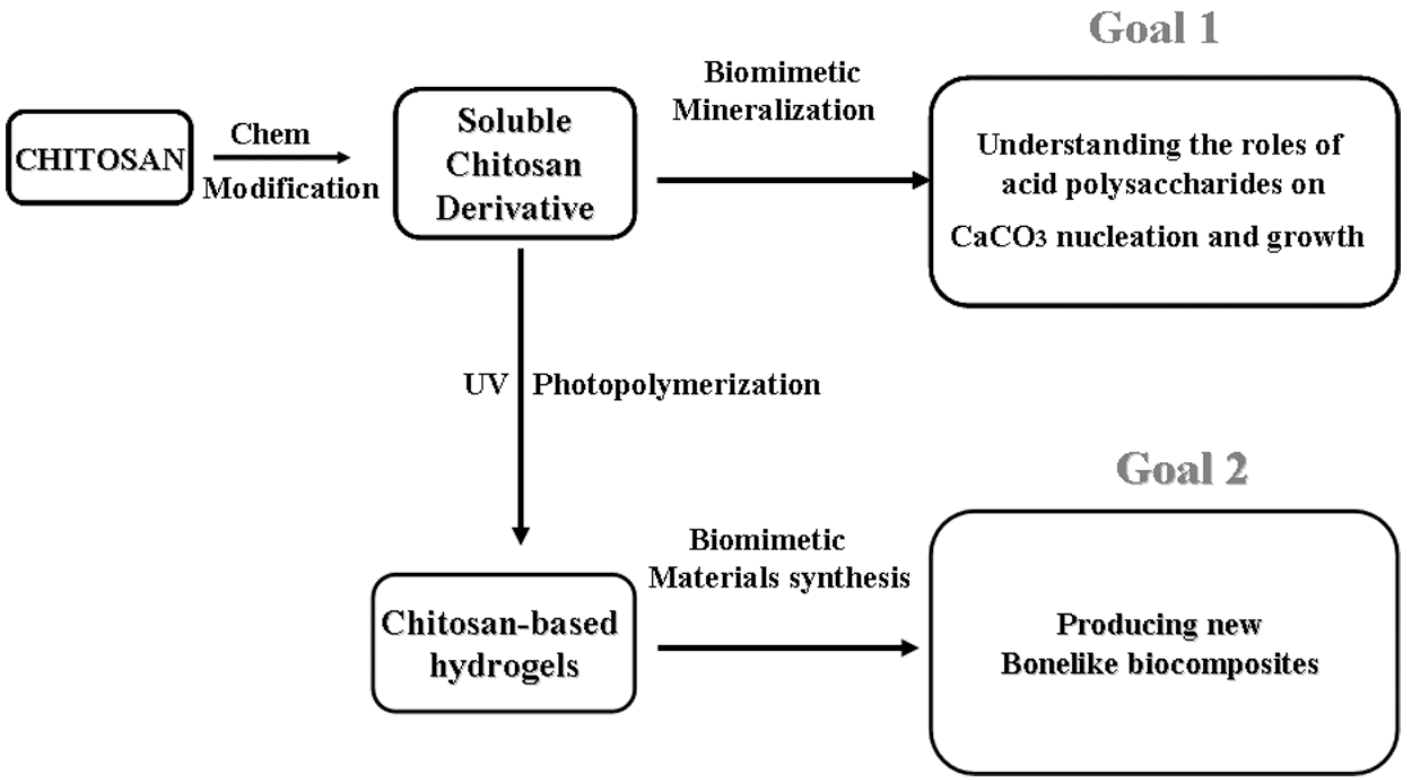

REFERENCES

1. Weiner HALaS, editor. *On Biomineralization*: Oxford University Press, USA, 1989.

2. Spear DG, Barr JK, Barr CE. Localization of hydrogen ion and chloride ion fluxes in nitella. *Journal of General Physiology* 1969;54(3):397-&.

3. Addadi L, Raz S, Weiner S. Taking advantage of disorder: Amorphous calcium carbonate and its roles in biomineralization. *Advanced Materials* 2003;15(12):959-970.

4. Weiner S, Levi-Kalisman Y, Raz S, Addadi L. Biologically formed amorphous calcium carbonate. *Connective Tissue Research* 2003;44:214-218.

5. Benzerara K, Menguy N, Lopez-Garcia P, Yoon TH, Kazmierczak J, Tyliszczak T, et al. Nanoscale detection of organic signatures in carbonate microbialites. *Proceedings of the National Academy of Sciences of the United States of America* 2006;103(25):9440-9445.

6. Muzzarelli RAA, editor. *Chitin*: New York: Pergamon Press, 1977.

7. Falini G, Fermani S. Chitin mineralization. *Tissue Engineering* 2004;10(1-2):1-6.

8. Arias JL, Fernandez MS. Polysaccharides and Proteoglycans in Calcium Carbonate-based Biomineralization. *Chemical Reviews* 2008;108(11):4475-4482.

9. Iijima M, Moriwaki Y. Orientation of apatite and organic matrix in lingula-unguis shell. *Calcif Tissue Int* 1990, 47(4):237-242.

10. Mikkelsen A, Engelsen SB, Hansen HCB, Larsen O, Skibsted LH. Calcium carbonate crystallization in the alpha-chitin matrix of the shell of pink.

shrimp, Pandalus borealis, during frozen storage. *Journal of Crystal Growth* 1997, 177(1-2):125-134.

11. Weiner S, Traub W. Macromolecules in mollusk shells and their functions in biomineralization. *Philosophical Transactions of the Royal Society of London Series B-Biological Sciences* 1984;304(1121):425-434.

12. Weiner S, Traub W. X-ray-diffraction study of the insoluble organic matrix of mollusk shells. *Febs Letters* 1980;111(2):311-316.

13. Sone ED, Weiner S, Addadi L. Biomineralization of limpet teeth: A cryo-TEM study of the organic matrix and the onset of mineral deposition. *Journal of Structural Biology* 2007;158(3):428-444.

14. Ehrlich H, Maldonado M, Spindler KD, Eckert C, Hanke T, Born R, et al. First evidence of chitin as a component of the skeletal fibers of marine sponges. Part I. Verongidae (Demospongia : porifera). *J Exp Zool Part B* 2007;308B:347-356.

15. Marsh ME, editor. *Biomineralization in Coccolithophores* 2ed: Wiley-VCH Verlag GmbH & Co. KGaA, Weinheim, Germany, 2004.

16. Young JR, Henriksen K. Biomineralization within vesicles: The calcite of coccoliths. In: *Biomineralization*, Dove PM, DeYoreo JJ, Weiner S, editors.; 2003; 2003:189-215.

17. Young JR, Davis SA, Bown PR, Mann S. Coccolith ultrastructure and biomineralisation. *Journal of Structural Biology* 1999 Jun;126(3):195-215.

18. Ozaki N, Sakuda S, Nagasawa H. A novel highly acidic polysaccharide with inhibitory activity on calcification from the calcified scale "coccolith" of a coccolithophorid alga, Pleurochrysis haptonemofera. *Biochemical and Biophysical Research Communications* 2007, 357(4):1172-1176.

19. Marsh ME. Polyanion-mediated mineralization - assembly and reorganization of acidic polysaccharides in the golgi system of a coccolithophorid alga during mineral deposition. *Protoplasma* 1994, 177(3-4):108-122.

20. Marsh ME, Chang DK, King GC. Isolation and characterization of a novel acidic polysaccharide containing tartrate and glyoxylate residues from the mineralized scales of a unicellular coccolithophorid alga pleurochrysis-carterae. *Journal of Biological Chemistry* 1992, 267(28):20507-20512.

21. Benzerara K, Menguy N, Guyot F, Dominici C, Gillet P. Nanobacteria-like calcite single crystals at the surface of the Tataouine meteorite. *Proceedings of the National Academy of Sciences of the United States of America 2003*, 100(13):7438-7442.

22. Benzerara K, Yoon TH, Menguy N, Tyliszczak T, Brown GE. Nanoscale environments associated with bioweathering of a Mg-Fe-pyroxene. *Proceedings of the National Academy of Sciences of the United States of America* 2005;102(4):979-982.

23. Chan CS, De Stasio G, Welch SA, Girasole M, Frazer BH, Nesterova MV, et al. Microbial polysaccharides template assembly of nanocrystal fibers. *Science* 2004;303(5664):1656-1658.

24. Arias JL, Neira-Carrillo A, Arias JI, Escobar C, Bodero M, David M, et al. Sulfated polymers in biological mineralization: a plausible source for bio-inspired engineering. *Journal of Materials Chemistry* 2004;14(14):2154-2160.

25. Puverel S, Tambutte E, Pererra-Mouries L, Zoccola D, Allemand D, Tambutte S. Soluble organic matrix of two Scleractinian corals: Partial and comparative analysis. *Comparative Biochemistry and Physiology B-Biochemistry & Molecular Biology* 2005;141(4):480-487.

26. Carrino DA, Rodriguez JP, Caplan AI. Dermatan sulfate proteoglycans from the mineralized matrix of the avian eggshell. *Connective Tissue Research* 1997;36(3):175-193.

27. Albeck S, Weiner S, Addadi L. Polysaccharides of intracrystalline glycoproteins modulate calcite crystal growth in vitro. *Chemistry-a European Journal* 1996;2(3):278-284.

28. Cohen AL, McConnaughey TA. Geochemical perspectives on coral mineralization. *Biomineralization* 2003;54:151-187.

29. Aizenberg J, Lambert G, Addadi L, Weiner S. Stabilization of amorphous calcium carbonate by specialized macromolecules in biological and synthetic precipitates. *Advanced Materials* 1996;8(3):222-226.

30. Hidehiro Ozawa KH, Norio Amizuka. Current concepts of bone biomineralization. J*ournal of Oral Biosciences* 2008;50(1):1-14.

31. Boskey AL, Spevak L, Doty SB, Rosenberg L. Effects of bone CS-proteoglycans, DS-decorin, and DS-biglycan on hydroxyapatite formation in a gelatin gel. *Calcified Tissue International* 1997;61(4):298-305.

32. Boskey AL, Stiner D, Binderman I, Doty SB. Effects of proteoglycan modification on mineral formation in a differentiating chick limb-bud mesenchymal cell culture system. *Journal of Cellular Biochemistry* 1997;64(4):632-643.

33. Rees SG, Wassell DTH, Shellis RP, Embery G. Effect of serum albumin on glycosaminoglycan inhibition of hydroxyapatite formation. *Biomaterials* 2004;25(6):971-977.

34. Septier D, Hall RC, Lloyd D, Embery G, Goldberg M. Quantitative immunohistochemical evidence of a functional gradient of chondroitin 4-sulphate dermatan sulphate, developmentally regulated in the predentine of rat incisor. *Histochemical Journal* 1998;30(4):275-284.

35. Takagi M, Maeno M, Yamada T, Miyashita K, Otsuka K. Nature and distribution of chondroitin sulphate and dermatan sulphate proteoglycans in rabbit alveolar bone. *Histochemical Journal* 1996;28(5):341-351.

36. Wise ER, Maltsev S, Davies ME, Duer MJ, Jaeger C, Loveridge N, et al. The organic-mineral interface in bone is predominantly polysaccharide. *Chemistry of Materials* 2007;19(21):5055-5057.

37. Reid DG, Duer MJ, Murray RC, Wise ER. The organic-mineral interface in teeth is like that in bone and dominated by polysaccharides: Universal mediators of normal calcium phosphate biomineralization in vertebrates? *Chemistry of Materials* 2008;20(11):3549-3550.

38. Duer MJ, Friscic T, Proudfoot D, Reid DG, Schoppet M, Shanahan CM, et al. Mineral Surface in Calcified Plaque Is Like That of Bone Further Evidence for

Regulated Mineralization. *Arteriosclerosis Thrombosis and Vascular Biology* 2008;28(11):2030-U2208.

39. Duer MJ, Friscic T, Murray RC, Reid DG, Wise ER. The Mineral Phase of Calcified Cartilage: Its Molecular Structure and Interface with the Organic Matrix. *Biophysical Journal* 2009;96(8):3372-3378.

40. Beniash E, Aizenberg J, Addadi L, Weiner S. Amorphous calcium carbonate transforms into calcite during sea urchin larval spicule growth. *Proceedings of the Royal Society of London Series B-Biological Sciences* 1997;264(1380):461-465.

41. Politi Y, Arad T, Klein E, Weiner S, Addadi L. Sea urchin spine calcite forms via a transient amorphous calcium carbonate phase. *Science* 2004;306(5699):1161-1164.

42. Weiss IM, Tuross N, Addadi L, Weiner S. Mollusc larval shell formation: Amorphous calcium carbonate is a precursor phase for aragonite. *Journal of Experimental Zoology* 2002;293(5):478-491.

43. Ma Y, Weiner S, Addadi L. Mineral deposition and crystal growth in the continuously forming teeth of sea urchins. *Advanced Functional Materials* 2007;17:2693-2700.

44. Aizenberg J, Weiner S, Addadi L. Coexistence of amorphous and crystalline calcium carbonate in skeletal tissues. *Connective Tissue Research* 2003;44:20-25.

45. Termine JD, Posner AS. Infrared analysis of rat bone - age dependency of amorphous and crystalline mineral fractions. *Science* 1966;153(3743):1523-.

46. Weiner S. Transient precursor strategy in mineral formation of bone. *Bone* 2006;39(3):431-433.

47. Mahamid J, Sharir A, Addadi L, Weiner S. Amorphous calcium phosphate is a major component of the forming fin bones of zebrafish: Indications for an amorphous precursor phase. *Proceedings of the National Academy of Sciences of the United States of America* 2008;105(35):12748-12753.

48. Beniash E, Metzler RA, Lam RSK, Gilbert P. Transient amorphous calcium phosphate in forming enamel. *Journal of Structural Biology* 2009;166(2):133-143.

49. Aizenberg J. Patterned crystallisation on self-assembled monolayers with integrated regions of disorder. *Journal of the Chemical Society-Dalton Transactions* 2000(21):3963-3968.

50. Aizenberg J, Black AJ, Whitesides GM. Controlling local disorder in self-assembled monolayers by patterning the topography of their metallic supports. *Nature* 1998;394(6696):868-871.

51. Aizenberg J, Black AJ, Whitesides GM. Oriented Growth of Calcite Controlled by Self-Assembled Monolayers of Functionalized Alkanethiols Supported on Gold and Silver. *Journal of the American Chemical Society* 1999;121:4500-4509.

52. Aizenberg J, Muller DA, Grazul JL, Hamann DR. Direct fabrication of large micropatterned single crystals. *Science* 2003;299(5610):1205-1208.

53. Gower LA, Tirrell DA. Calcium Carbonate films and helices grown in solutions of poly(aspartate). *Journal of Crystal Growth* 1998;191:153-160.

54. Gower LB, Odom DJ. Deposition of calcium carbonate films by a polymer-induced liquid-precursor (PILP) process. *Journal of Crystal Growth* 2000;210:719-734.

55. Levi-Kalisman Y, Falini G, Addadi L, Weiner S. Structure of the nacreous organic matrix of a bivalve mollusk shell examined in the hydrated state using Cryo-TEM. *Journal of Structural Biology* 2001;135(1):8-17.

56. Estroff LA, Addadi L, Weiner S, Hamilton AD. An Organic Hydrogel as a Matrix for the Growth of Calcite Crystals. *Organic & Biomolecular Chemistry* 2004:137-141.

57. Li HY, Estroff LA. Hydrogels coupled with self-assembled monolayers: An in vitro matrix to study calcite biomineralization. *Journal of the American Chemical Society* 2007;129(17):5480-5483.

58. Li HY, Estroff LA. Porous calcite single crystals grown from a hydrogel medium. *Crystengcomm* 2007;9:1153-1155.

59. Li HY, Estroff LA. Calcite Growth in Hydrogels: Assessing the Mechanism of Polymer-Network Incorporation into Single Crystals. *Advanced Materials* 2009;21(4):470-473.

60. Colfen H. Double-hydrophilic block copolymers: Synthesis and application as novel surfactants and crystal growth modifiers. *Macromolecular Rapid Communications* 2001 Feb;22(4):219-252.

61. Colfen H, Antonietti M. Crystal design of calcium carbonate microparticles using double-hydrophilic block copolymers. *Langmuir* 1998;14(3):582-589.

62. Colfen H, Qi LM. A systematic examination of the morphogenesis of calcium carbonate in the presence of a double-hydrophilic block copolymer. *Chemistry-a European Journal* 2001;7(1):106-116.

63. Donners JJJM, Heywood BR, Meijer EW, Nolte RJM, Roman C, Schenning APHJ, et al. Amorphous Calcium Carbonate Stabilised by Poly(propylene imine) dendrimers. *Chemical Communications* 2000:1937-1938.

64. Pichon BP, Bomans PHH, Frederik PM, Sommerdijk N. A quasi-time-resolved CryoTEM study of the nucleation of CaCO3 under langmuir monolayers. *Journal of the American Chemical Society* 2008;130(12):4034-4040.

65. Donners JJJM, Nolte RJM, Sommerdijk NAJM. A Shape-Persistent Polymeric Crystallization Template for $CaCO_3$. *Journal of the American Chemical Society* 2002;124(33):9700-9701.

66. Gebauer D, Volkel A, Colfen H. Stable Prenucleation Calcium Carbonate Clusters. *Science* 2008;322(5909):1819-1822.

67. Pouget EM, Bomans PHH, Goos J, Frederik PM, de With G, Sommerdijk N. The Initial Stages of Template-Controlled CaCO3 Formation Revealed by Cryo-TEM. *Science* 2009;323(5920):1555-1458.

68. Hartgerink JD, Beniash E, Stupp SI. Self-assembly and mineralization of peptide-amphiphile nanofibers. *Science* 2001, 294(5547):1684-1688.

69. Spoerke ED, Anthony SG, Stupp SI. Enzyme Directed Templating of Artificial Bone Mineral. *Advanced Materials* 2009 Jan;21(4):425-430.

70. Glimcher MJ. Recent studies of the mineral phase in bone and its possible linkage to the organic matrix by protein-bound phosphate bonds. *Philosophical Transactions of the Royal Society of London Series B-Biological Sciences* 1984;304(1121):479-508.

71. Zhang RY, Ma PX. Porous poly(L-lactic acid)/apatite composites created by biomimetic process. *Journal of Biomedical Materials Research* 1999;45(4):285-293.

72. Verma D, Katti K, Katti D. Bioactivity in in situ hydroxyapatite-polycaprolactone composites. *Journal of Biomedical Materials Research Part A* 2006 ;78(4):772-780.

73. Chen HF, Clarkson BH, Sun K, Mansfield JF. Self-assembly of synthetic hydroxyapatite nanorods into an enamel prism-like structure. *Journal of Colloid Interface Science* 2005;288(1):97-103.

74. Song J, Saiz E, Bertozzi CR. A new approach to mineralization of biocompatible hydrogel scaffolds: An efficient process toward 3-dimensional bonelike composites. *Journal of the American Chemical Society* 2003;125(5):1236-1243.

75. Song J, Malathong V, Bertozzi CR. Mineralization of synthetic polymer scaffolds: A bottom-up approach for the development of artificial bone. *Journal of the American Chemical Society* 2005;127(10):3366-3372.

76. Palmer LC, Newcomb CJ, Kaltz SR, Spoerke ED, Stupp SI. Biomimetic Systems for Hydroxyapatite Mineralization Inspired By Bone and Enamel. *Chemical Reviews* 2008;108(11):4754-4783.

77. Dickerson MB, Sandhage KH, Naik RR. Protein- and Peptide-Directed Syntheses of Inorganic Materials. *Chemical Reviews* 2008;108(11):4935-4978.

CHAPTER 2

SYNTHESIS OF MALEIC CHITOSAN VIA NEW ORGANO-SOLUBLE CHITOSAN SALT INTERMEDIATES

*Chao Zhong† and C. Chang Chu†,‡,**

Fiber and Polymer Science Program, Department of Fiber science and Apparel design, Cornell University, Ithaca, New York 14853-4401

Biomedical Engineering Program, Cornell University, Ithaca, New York 14853-4401

Email: cz38@cornell.edu; cc62@cornell.edu*

* To whom correspondence should be addressed. Phone: (607) 255-1938, Fax: 607) 255-1093.

Email: cc62@cornell.edu

† Department of Fiber science

‡ Biomedical Engineering Program

Note: this chapter is to be submitted to *Biomacromolecules*.

2.1 Abstract

Organo-soluble chitosan intermediates were developed for efficient chemical modifications of chitosan. The intermediates, methanesulfonic (or tolunesulfonic) chitosan salts, were obtained from the ionic reaction of primary amine on chitosan backbone with methanesulfonic or tolunesulfonic acids in water at room temperature. The chitosan salts exhibit excellent solubility in some polar solvents, such as water, formamide and dimethyl sulfoxide (DMSO) and were characterized by ^{1}H NMR, ^{13}C NMR and FT-IR. The efficiency and usefulness of these intermediates for subsequent chemical modification of chitosan was demonstrated by the ring-opening reaction with maleic anhydride in either formamide or DMSO solvent. The resulting product, N, O-maleic chitosan, was then hydrolyzed in NaOH solution to prepare N-maleic chitosan. The chemical structures of N, O-maleic chitosan and N-maleic chitosan were elucidated by FT-IR, 1H NMR and ^{13}C NMR and 2D ^{1}H-^{1}H COSY. This paper reports a simple but highly efficient synthetic route to synthesize organo-soluble chitosan salt intermediates which were then used to synthesize chitosan derivatives like maleic chitosan.

Keywords Chitosan, Organo-soluble intermediates, Maleic chitosan and Methanesulfonic (or tolunesulfonic) chitosan salts

2.2 Introduction

Chitosan is a partially deacetylated product of chitin, the second most abundant polysaccharide in nature [1]. As a biocompatible [2] and biodegradable [3] polymer, chitosan has attracted considerable attention in fields ranging from pharmacy and biomedicine [4-6] to the food and textile industries [7, 8]. There have been many attempts to modify the molecular structure of chitosan in order to introduce tailored properties into it, including the incorporation of new sugar moieties, the grafting of long polymeric or polypeptide chains and enzymatic modifications [9-11]. However, the chemical reactions of chitosan are usually hampered by its poor solubility in common organic solvents including both polar (e.g. DMSO) and non-polar solvents (e.g. benzene). Typically, chitosan can only dissolve in some dilute acid solutions, such as acetic or hydrochloride acid.

Accordingly, it would be desirable to develop organo-soluble chitosan intermediates for its subsequent chemical modifications. Although some organo-soluble chitosan intermediates [12-18], for example, 6-O-triphenylmethyl-chitosan [19-21], have proved useful for performing modification reactions in a controlled manner, the synthesis of these intermediates usually had to be carried out via multi-step reactions and under harsh and heterogeneous conditions because chitosan itself is not soluble in the solvent used, i.e., DMF [22]. Furthermore, subsequent modification reactions based on these chitosan intermediates suffer from several limitations, such as expensive and complicated deprotection protocols and susceptibility to backbone degradation during the deprotection processes [23].

Simple, versatile and cost-effective organo-soluble chitosan intermediates would therefore be of great value in designing and developing novel and tailored chitosan derivatives and in realizing the commercial potential of chitosan derivatives in different applications.

We report here a new type of organo-soluble chitosan intermediates (methanesulfonic/tolunesulfonic chitosan salts) for the subsequent efficient and easy preparation of chitosan derivatives. We demonstrate their efficiency using the ring-opening reaction with maleic anhydride in either formamide or DMSO solvent. We also show that the synthetic route of maleic chitosan based on the novel chitosan intermediates in combination with the hydrolysis strategy produces regioselective modifications of chitosan at C-2 amino groups.

2.3 Experimental Section

2.3.1 Materials

Chitosan from Sigma had 75-85% degree of deacetylation, with Brookfield viscosity 20.0-200cps (1% acetic acid) and molecular weight approximately 50,000 daltons based on viscosity data. The dialysis membrane (Fisherbrand regenerated cellulose, Fisher Scientific) had a reported MW cutoff of 12 Kda. Maleic anhydride, p-tolunesulfonic acid monohydrate ($TosOH \cdot H_2O$), methanesulfonic acid and sodium bicarbonate were purchased from Sigma-Aldrich and used as received. Formamide from EMD Chemicals (stored in refrigerator) was first defrozened and used immediately. Other organic solvents including dimethyl sulfoxide (DMSO), acetone and isopropanol alcohol from VWR Scientific were used without further purification.

2.3.2 Synthesis of methanesulfonic or tolunesulfonic chitosan salts as organo-soluble intermediates

The general procedures for preparing methanesulfonic or tolunesulfonic chitosan salts are shown in Scheme 2.1. Typically, chitosan (1.0g) was dispersed in 100mL deionized water. Methanesulfonic acid or tolunesulfonic acid [molar ratio (acid: amine group) =1.2] was then added to the suspended solution and stirred for 2 hours at room temperature. After 2 hours, chitosan was completely dissolved and was precipitated by

addition of copious amounts of acetone or isopropanol. The precipitated product was washed with acetone for several times and dried in vacuum. The yields of the products ranged from 93~97%.

2.3.3. Solubility of methanesulfonic or tolunesulfonic chitosan salts

Solubility test of all chitosan salts (including the other salts described in Table 2.1) was carried out with 10mg salt samples dissolved in 1mL corresponding solvents at room temperature. The mixture was stirred for 1 day, and the solubility of the salts in the solvent was evaluated based on whether the remaining powders were still present or not in the solvent.

2.3.4 Synthesis of maleic chitosan from organo-soluble chitosan salts

Synthesis of N, O-maleic chitosan

The general synthetic route of N, O-maleic chitosan was presented in Scheme 2.1. Typically, 1.489 g methanesulfonic (or 1.875g tolunesulfonic) chitosan salts were dissolved in 100mL Formamide or DMSO solvent under stirring at room temperature. Solid maleic anhydride (3.52g) of 6-fold in molar ratio of sugar units was then added to the solution, and the reaction mixture was stirred under N_2 at 60 ^{o}C for 24 hrs. The resulting product in the solution was precipitated out by acetone, filtered, washed with copious amounts of acetone, and dried. Methanesulfonic (or tolunesulfonic) anions in the product were then removed from the chitosan salts by adding 0.1M $NaHCO_3$ solution. Finally the solution was dialyzed against deionized water to remove the remaining contaminants (e.g. small amount of $NaHCO_3$ and organic solvents) in the solution for more than 3 days (MW cut off 12,000) and lyophilized for 3 days using a Virtis Freeze Drier (Gardiner, NY) under vacuum at -42°C. The yields of the final products range from 69% to 89% (the exact yield depends on the reaction system employed, see Table 2.2).

Scheme 2.1. Synthetic Route for the Preparation of Organo-soluble Chitosan Salts (II), N, O-Maleic Chitosan (III) and N-maleic Chitosan (IV)

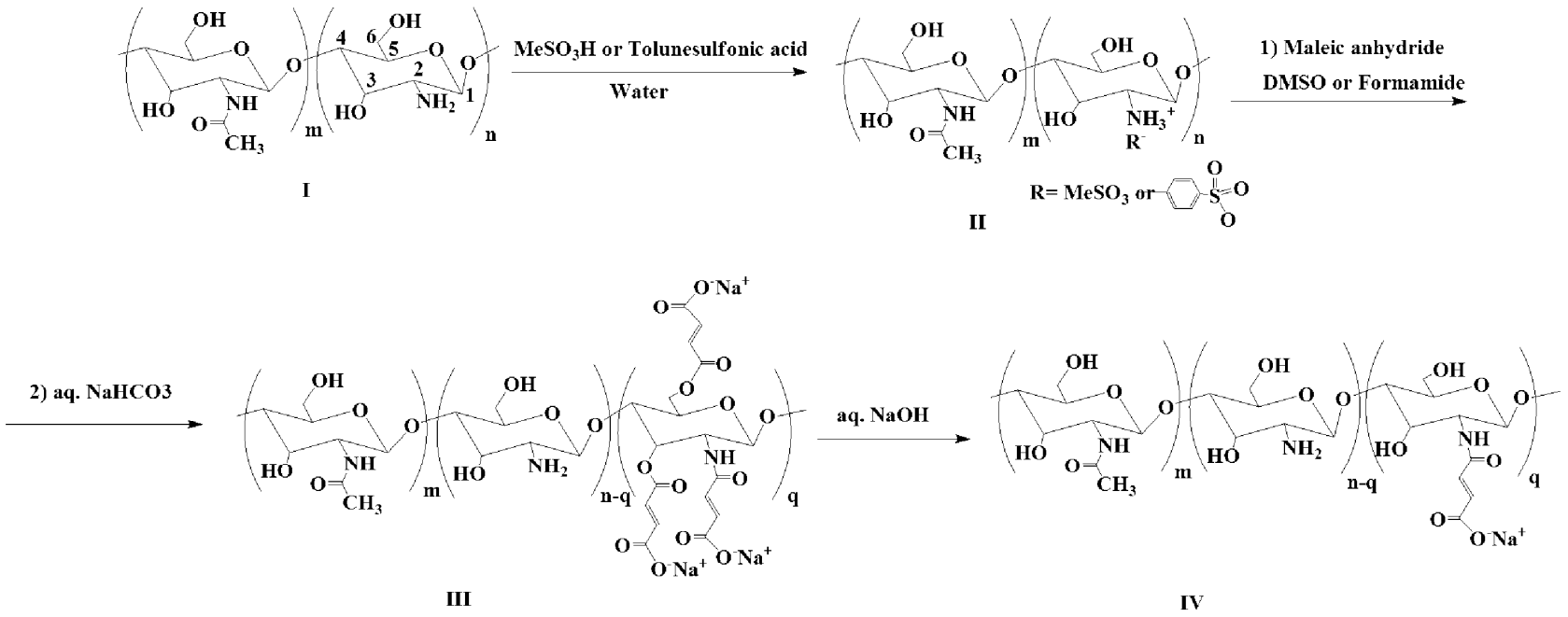

Synthesis of N-maleic chitosan

A complete hydrolysis of the ester groups on N, O-maleic chitosan led to N-maleic chitosan. 0.5g N, O-maleic chitosan was hydrolyzed in 20mL 0.1M aqueous sodium hydroxide at room temperature for 10h, and then dialyzed against deionized water for 3 days and lyophilized to give a product of 0.33g.

2.3.5 Characterization

FTIR spectra were obtained with a Perkin-Elmer (Madison, WI) Nicolet Magana 560 spectrometer from KBr pellets. X-ray diffraction(wide-angle) data were obtained from powdered samples with θ-θ diffractometer (Scintag, Inc., Cupertino, CA) with Cu Kα radiation (wavelength =1.5405 Å).

Molecular weight was determined based on the intrinsic viscosity approach using Mark-Houwink equation. Specifically, we adopted the empirical equation, $[\eta] = 3.04 \times 10^{-5} \times M_r^{1.26}$ to determine the molecular weight of Maleic chitosan [24].

Zeta-Potential of Maleic chitosan was measured using a Malvern Zetasizer Nano-ZS analyzer at room temperature. Maleic chitosan with varied degree of substitution (1.20, 1.37, and 1.55) were used for Zeta-Potential measurement. Briefly, maleic chitosan (MA-CS) solution (2 wt %) was prepared by dissolving maleic chitosan in 1×PBS buffer solution and the solution was filtered with ultra microfilter (0.2 μm pore size, whatman) before experiments. Zeta potentials were calculated by using the Smoluchowsky model for aqueous suspensions. Each sample was measured for triple times.

^{1}H and ^{13}C NMR spectra were recorded on a Varian (Palo Alto, CA) Unity INOVA 500-MHz spectrometer operating at 500 and 125.7 MHz, respectively. Samples of maleic chitosan (20 mg) were dissolved in 600μl of D_2O (Cambridge Isotope lab, Inc). Chemical shifts (δ) are reported in parts per million (ppm) using sodium 3-(trimethylsilyl) propionate-d4 (Aldrich) as an internal standard. To get good

NMR signals, all measurements were carried out at 353K. ^{1}H-^{1}H homonuclear single correlation (gradient-enhanced COSY) experiments were carried out on Varian (Palo Alto, CA) Unity INOVA 600-MHz spectrometer.

For NMR spectra of N, O-maleic chitosan, the detailed assignment of the double bond peaks at different substituent positions was done by comparing the ^{1}H, ^{13}C NMR of N, O-maleic chitosan with those of N-maleic chitosan, and assuming that C-6 hydroxyl group is more reactive than C-3 hydroxyl group due to the steric hindrance of the C-3 hydroxyl group[25]. Total degree of substitution (DS) of N, O-maleic chitosan was determined from ^{1}H NMR spectrum by comparing the integrals from the double bond signals (δ 5.8-5.95ppm) with the integrals of the hemiacetal proton signal (H-1, δ 4.5–4.8 ppm), or by comparing the integrals from the double bond signals with the integrals of the polysaccharide backbone proton signals (both methods give similar results).

DS of N substitution, C-6(O) substitution and C-3(O) substitution were determined by formula (1), (2) and (3), respectively.

DS(N)=[1 – Integrals of H-2 of GlcN residue (δ2.8ppm)]/[Integrals of the hemiacetal proton signal (H-1,δ4.5~4.8ppm)] – [1/3×integrals of CH_3(N-acetyl,δ2.05ppm) /Integrals of the hemiacetal proton signal] (1)

DS(C-6(O)) = [Integrals of H-9'(C-6(O) substitution, δ6.65ppm)]/[Integrals of the hemiacetal proton signal] (2)

DS(C-3(O)) = [Total DS – DS (N) – DS(C-6(O))], or DS(C-3(O)) = [Integrals of H-9"and H-9(both C-3(O) and N substitution, δ6.4ppm)]/ [Integrals of the hemiacetal proton signal – DS (N)] (3)

Methanesulfonic or tolunesulfonic chitosan salts:

FT-IR (Methanesulfonic chitosan salt): ν 3600-3200 (O-H stretch), ν1683(amide I, N-acetyl), ν1638(amide II , N-acetyl), ν1527(NH_3+ deformation vibration) ν 1192(asym SO_3 str), ν 1048(sym SO_3 str), ν784(S-C stretch), ν 522, 557(SO_2 def, two bands).

FT-IR (Tolunesulfonic chitosan salt): ν 3600-3200 (O-H stretch), ν1642 (amide I, N-acetyl), ν1536 (NH_3+ deformation vibration), ν 1164(asym SO_3 str), ν 1123, 1009(aromatic =C-H in-plane deformation), ν 817(aromatic =C-H out-of-plane deformation), ν690(S-C stretch), ν571 (SO_2 def).

^{1}H NMR (Methanesulfonic chitosan salt) at 353K (D_2O): δ2.06 (CH_3, N-acetyl), 2.79(CH_3SO_3-), 3.10(H-2, when amino groups react with methanesulfonic acids), 3.5-3.7(H-5), 3.70-3.85(H-4), 3.75-3.9(H-3), 3.80-4.0(H-6), 4.6-4.85(H-1) ppm.

^{13}CNMR (Methanesulfonic chitosan salt) at 353K (D_2O): δ25.02 (CH_3, N-acetyl), 41.37(CH_3SO_3-), 58.93(C-2), 63.13(C-6), 73.88(C-3), 77.63(C-5), 80.20(C-4), 101.70(C-1) ppm.

^{1}H NMR (Tolunesulfonic chitosan salt) at 353K (D_2O): δ2.04(CH_3, N-acetyl), 2.37(CH_3 of tolunesulfonic anion), 2.95(H-2 of GlcN unit, when amine groups binding with tolunesulfonic anions), 3.5-3.7(H-5), 3.65-3.85(H-4), 3.75-3.9(H-3), 3.8-4.0(H-6), 4.68(H-1), 7.35(H-3,5of tolunesulfonic), 7.68(H-2,6 of tolunesulfonic) ppm.

^{13}C NMR (Tolunesulfonic chitosan salt) at 353K (D_2O): δ23.18(CH_3 of tolunesulfonic anion),25.05((CH_3,N-acetyl),59.05(C-2),63.36(C-6),74.81(C-3), 77.90(C-5),80.66(C-4),102.93(C-1), 128.35,132.15,143.04, 144.93 (C from Phenyl groups)ppm.

N, O-maleic chitosan:

FT-IR (cm^{-1}): ν 3600-3200 (O-H), ν 1724, (C=O ester), 1666 (amide I, N-acetyl), 1573(C=C stretching, conjugated with C=O), 853, 812 (CH (-CH=CH-) out-of-plane def)

1H NMR at 353K(D2O): δ 2.05 (CH_3, N-acetyl), δ 2.8(H-2,Glcn residue), 3.4-4.0(H-6), 3.5-3.7(H-5), 3.55-3.8(H-4),3.6-3.85(H-3), 3.65-3.9(H-2), 4.5-4.8 ppm (H-1), 5.80-5.85(H-8'',C-3(O) substitution), 5.85-5.90(H-8', C-6(O) substitution), 5.90-5.95(H-8, C-2(N) substitution), 6.40(H-9'',C-3(O) substitution), 6.40(H-9, C-2(N)substitution), 6.65(H-9', C-6(O) substitution)ppm.

13C NMR at 353K(D2O): δ 24.92(CH_3, N-acetyl), 57.71(C-2), 62.88(C-6, unsubstituted), 65.30(C-6, substituted), 75.07(C-3), 77.41(C-5), 82.27(C-4), 104.01(C-1),120.70(C-8, C-6(O)substitution), 127.21(C-8, C-2(N)substitution), 136.14(C-9, C-3(O) substitution), 140.26(C-9, C-2(N) substitution) 144.77(C-9, C-6(O) substitution), 169.52(C-7, ester of C-6(O) substitution), 170.63(C-7, amide, C-2(N) substitution),174.64(C-7,ester, C-3(O) substitution),176.50(C-10, carboxyl, from both C-2(N), C-3,6(O) substitution),187.08(C=O, N-acetyl) ppm.

N-maleic chitosan:

FT-IR (cm^{-1}): ν 3600-3200 (O-H stretch), 1666 (amide I, N-acetyl), 1573(C=C stretching, conjugated with C=O), 853, 812 (CH (-CH=CH-) out-of-plane def)

^{1}HNMR at 353K(D_2O): δ 2.06(CH_3, N-acetyl), 2.70(H-2, when amino groups are not substituted),3.4-4.0(H-6),3.5-3.7(H-5),3.55-3.8(H-4),3.6-3.85(H-3),3.65-3.9(H-2), 4.5-4.8(H-1), 5.93(H-8), 6.44(H-9) ppm.

^{13}CNMR at 353K (D_2O): δ24.92(CH_3,N-acetyl),58.06(C-2),63.1(C-6), 75.19(C-3), 77.54(C-5), 82.07(C-4), 104.04(C-1), 126.99(C-8), 140.35(C-9), 170.72 (C-7, amide,N-substitution), 176.69(C-10, Carboxyl),188.59(C=O, N-acetyl)ppm.

2.4 Results and Discussion

2.4.1 Methanesulfonic & Tolunesulfonic chitosan salts

The proposed one-step reaction for achieving a high yield of organo-soluble chitosan salt intermediates provides many advantages over conventional means of preparing similar organo-soluble chitosan intermediates. Conventionally, organo-soluble chitosan intermediates like N-phthaloyl-chitosan and 6-O-triphenylmethyl-chitosan have been obtained by incorporating bulky hydrophobic substituents onto chitosan backbone [26]. One of the main features of this conventional approach is that it involves multi-step reactions (for example, 3 steps for 6-O-triphenylmethyl-chitosan) and the initial step reactions have to be carried out under very harsh heterogeneous reaction conditions (for example: over 100 ^{o}C and 72-hour reaction time [22]), as chitosan itself is not soluble in the solvents used (e.g., DMF [22]).

In contrast, our preparation of organo-soluble methanesulfonic or tolunesulfonic chitosan salts was accomplished under mild homogeneous conditions (using water as the solvent at room temperature within 2 hours). Moreover, our organo-soluble chitosan salt intermediates (methanesulfonic and tolunesulfonic chitosan salts) were easily elucidated by liquid-state ^{1}H NMR and ^{13}C NMR due to their good solubility in DMSO or water. (The conventional procedure for synthesizing organo-soluble chitosan intermediates cannot be characterized by liquid-state NMR, probably because they are insufficiently soluble [23].) Finally, the resulting methanesulfonic or tolunesulfonic chitosan salts obtained in our procedure are very stable with more than one year shelf life if stored in a dry environment.

One of the major reasons for the intractability of chitosan in chemical modifications lies in its rigid crystalline structure [18, 27, 28], and the primary amine groups on the backbone are responsible for the formation of peculiar conformational features through Intra- and/or intermolecular hydrogen bonding [18]. Removal of the

hydrogen atoms of amino groups by introduction of some hydrophobic groups through chemical modifications has proven to be an effective way to destroy the inherent crystalline structure of chitosan, thereby enhancing its solubility in common organic solvents [14, 29]. Accordingly, we deduced that the transformation of chitosan into a salt form by reacting primary amino groups with certain acids might also destroy the crystalline structure and enhance the solubility of chitosan in common organic solvents.

For our study, we chose several acids, ranging from hydrochloride acid to tolunesulfonic acid. Table 2.1 lists the general trend of solubility of chitosan salts in decreasing order of solvent polarity (empirical parameter of solvent polarity (EtN) value). Generally, the data show that both methansulfonic and tolunesulfonic chitosan salts dissolve more easily in high polar solvents than in low polar solvents, probably because of the inherent polarity of the chitosan backbone. Both chitosan salts dissolve in some solvents (water, formamide and DMSO), whereas hydrochloride acid and acetic acid chitosan salts only dissolve in water. The toluenesulfonic chitosan salts had an upper solubility of 40 mg/mL in DMSO.

The transformation of chitosan into chitosan salts effectively destroyed the inherent crystalline structure of chitosan. In contrast to chitosan (Figure 2.1a), both methanesulfonic and tolunesulfonic chitosan salts exist in an near-amorphous state (Figure. 2.1d and e), which explains their enhanced solubility in some organic solvents. However, their solubility in organic solvents also depends on the nature of counterion in salts. For example, the crystalline structure of the hydrochloride acid and acetic acid chitosan salts was completely destroyed (Figure 2.1b & c), these chitosan salts did not dissolve in any of the organic solvents tested other than water.

Table 2.1. Solubility of Chitosan Salts in Different Solvents

Solvent	Water	Formamide	DMSO	DMF	DMAC	Acetone	Pyridine	$CHCl_3$	THF	Benzene
E_t^N(solvent)	1.0	0.775	0.444	0.386	0.377	0.355	0.302	0.259	0.207	0.111
Chitosan	_	_	_	_	_	_	_	_	_	_
Chitosan(HCl)	+	_	_	_	_	_	_	_	_	_
Chitosan (CH_3COOH)	+	±	_	_	_	_	_	_	_	_
Chitosan ($MeSO_3H$)	+	+	+	_	_	_	_	_	_	_
Chitosan (p-tolunesulfonic acid)	+	+	+	±	_	_	_	_	_	_

Note: (+) Soluble, (±) Partially soluble or swelled, (-) Insoluble; E_t^N Value (Empirical parameter of solvent polarity) [30] ; All solubility tests were carried out with 10mg salt samples dissolved in 1mL corresponding solvents.

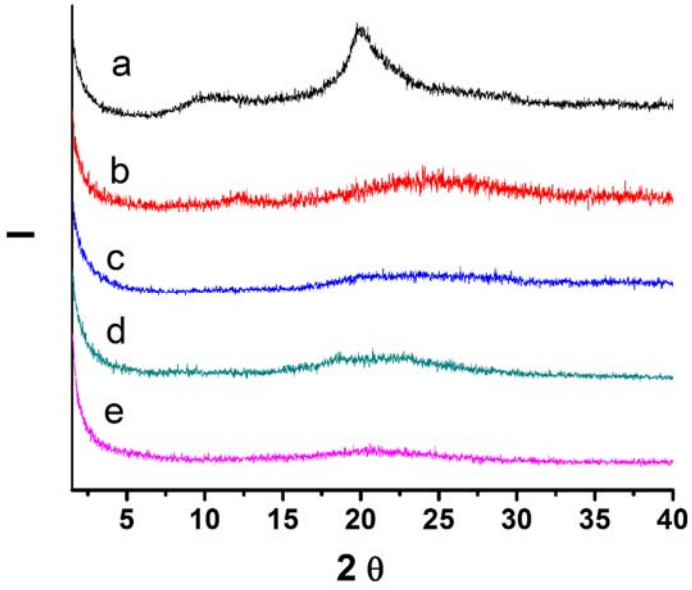

Figure 2.1. X-ray diffraction diagram of (a) Chitosan, (b) hydrochloride acid chitosan salt, c) acetic acid chitosan salt, (d) methanesulfonic chitosan salt and (e) tolunesulfonic chitosan salt.

2.4.2 N, O-Maleic chitosan prepared from methanesulfonic & tolunesulfonic chitosan salt intermediates

NMR and FTIR spectra were used to analyze the detailed structure of the chitosan derivataive (maleic chitosan) prepared from chitosan salts. Typical NMR data of maleic chitosan were shown in Figure 2.2. The incorporation of pendant double bonds onto chitosan backbone was confirmed by ^{1}H NMR, as indicated by the appearance of the peaks at δ 5.95, 6.42, and 6.68 ppm (Figure 2.2a). This was also confirmed by FTIR due to the appearance of an absorption band at 808.6 cm^{-1}, corresponding to the –CH (–CH=CH–) out-of-plane deformation (Figure 2.3a). Correspondingly, the presence of new peaks around δ 120~150 ppm in ^{13}C NMR spectrum (Figure 2.2b) was due to the C signals from the double bonds, while the peaks around δ 170~180ppm in ^{13}C NMR could be ascribed to C signals from the carbonyl groups because of the newly formed ester, amide bonds and carboxyl groups.

The total degree of substitution (DS) of maleic chitosan was determined from ^{1}H NMR spectrum by comparing the integrals from the double bond signals (δ 5.8-5.95ppm) with the integrals of the hemiacetal proton signal (H-1, δ 4.5–4.8 ppm) (Figure 2.2c). The accuracy of this approach to determine DS was confirmed by the measured zeta potential values of maleic chitosan with different degree of substitution. As shown in Figure 2.4, the zeta potentials of maleic chitosan are all negative in PBS solution due to the presence of pendent carboxyl groups, with the values becoming more negative (decreasing) as the DS of maleic chitosan increases.

The calculated degree of substitution (DS) based on ^{1}H NMR (DS=1.47, the value is 3 if fully substituted) and the multiple signals from the double bonds in both ^{1}H NMR and ^{13}C NMR imply that the substitution took place at both amino and hydroxyl groups of chitosan (Figure 2.2c, d). ^{1}H-^{1}H COSY NMR further confirmed that substitutions not only occurred at the C-6 hydroxyl groups and C-2 amino groups, but also the relatively less active C-3 hydroxyl groups, as 3 different signals off the diagonal appear in the region of double bond signals in ^{1}H-^{1}H COSY NMR (Figure 2.2e). The 3 different signals directly come from the couplings between neighboring protons of the double bond structure in 3 different molecular environments, or more specifically, different substituent positions. The complete assignment of the double bond peaks at different substituent positions could be done by comparing both ^{1}H NMR and ^{13}C NMR data with those of N-maleic chitosan. The specific assignments were listed in the characterization of the experimental section.

In summary, of the three substitution sites on the chitosan unit, the substitutions took place mainly at C-2 amine site, followed by C-6 hydroxyl group site, with the least substitution occurring at the C-3 hydroxyl group site. It is worth noting that, although the ionic linkage exits between ionized amine and methanesulfonic anions, the substitution still successfully took place at the C-2 amino groups.

Figure 2.2. (a) ^{1}H NMR spectra of N-maleic chitosan, (b) ^{13}C NMR spectra of N-maleic chitosan, (c) ^{1}H NMR spectra of N, O-maleic chitosan, (d) ^{1}H-^{1}H COSY of N, O-maleic chitosan(region of double bond signals), and (e) ^{13}C NMR spectra of N, O-maleic chitosan. N, O-Maleic chitosan was prepared under optimum conditions (60 ^{o}C for 24hs, molar ratio (tolunesulfonic Chitosan salt/maleic anhydride) = 1:6) in a system where tolunesulfonic chitosan salt and formamide were used as intermediate and solvent respectively. N-maleic chitosan was prepared by hydrolysis of N, O-maleic chitosan in 0.1M aqueous sodium hydroxide, RT, 10hs.

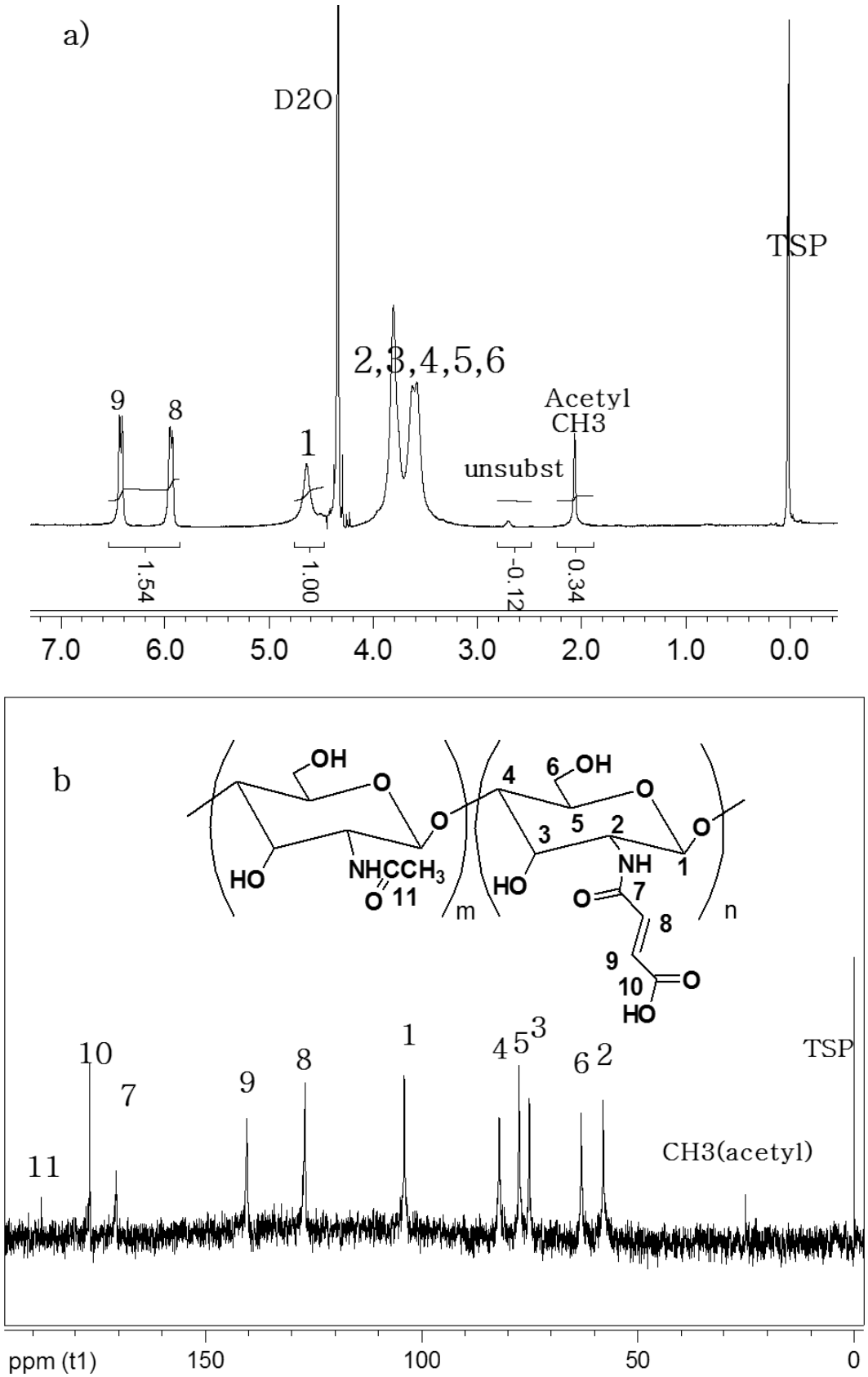
a)
D2O
TSP
2,3,4,5,6
9
8
1
Acetyl
CH3
unsubst
1.54
1.00
-0.12
0.34
7.0
6.0
5.0
4.0
3.0
2.0
1.0
0.0
b
OH
O
O
HO
NHCCH3
O 11
m
4
6 OH
O
3
5
2
O
HO
NH
1
O
7
8
n
9
10
O
HO
10
7
9
8
1
4 5 3
6 2
TSP
11
CH3(acetyl)
ppm (t1)
150
100
50
0

Figure 2.2 (Continued)

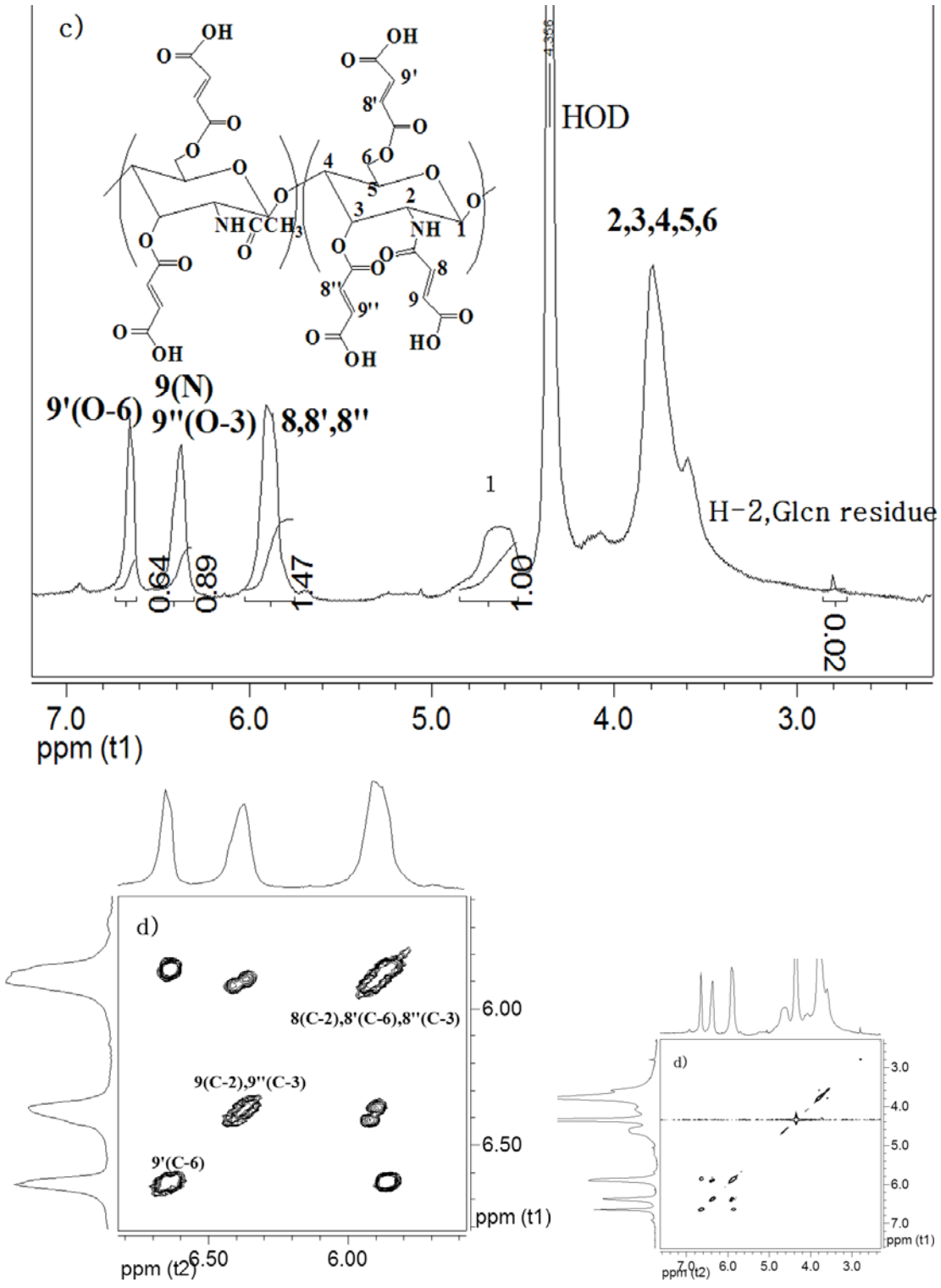

Figure 2.2 (Continued)

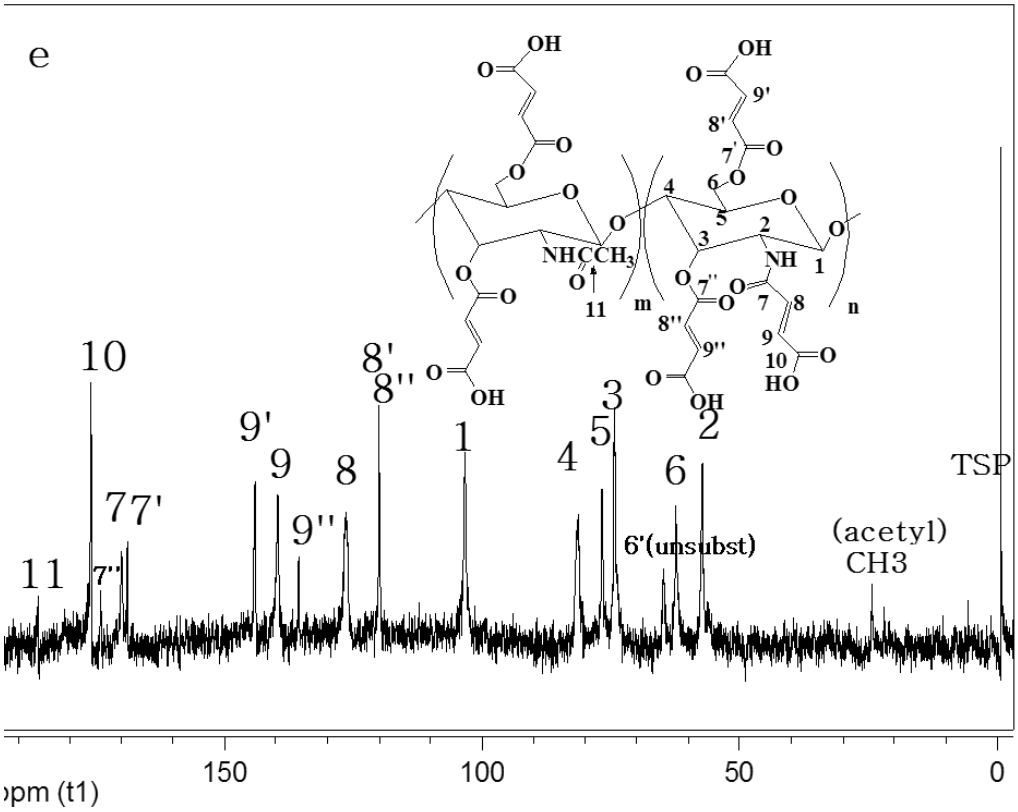

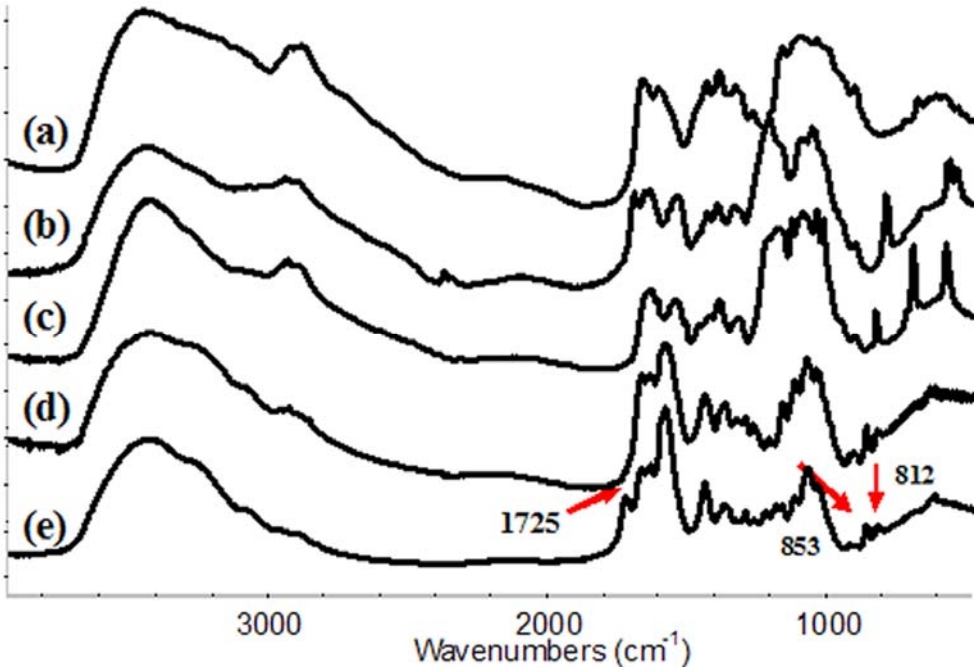

Figure 2.3. FTIR spectra of (a) chitosan, (b) methanesulfonic chitosan, (c) tolunesulfonic chitosan, (d) N-maleic chitosan, (e) N, O-maleic chitosan.

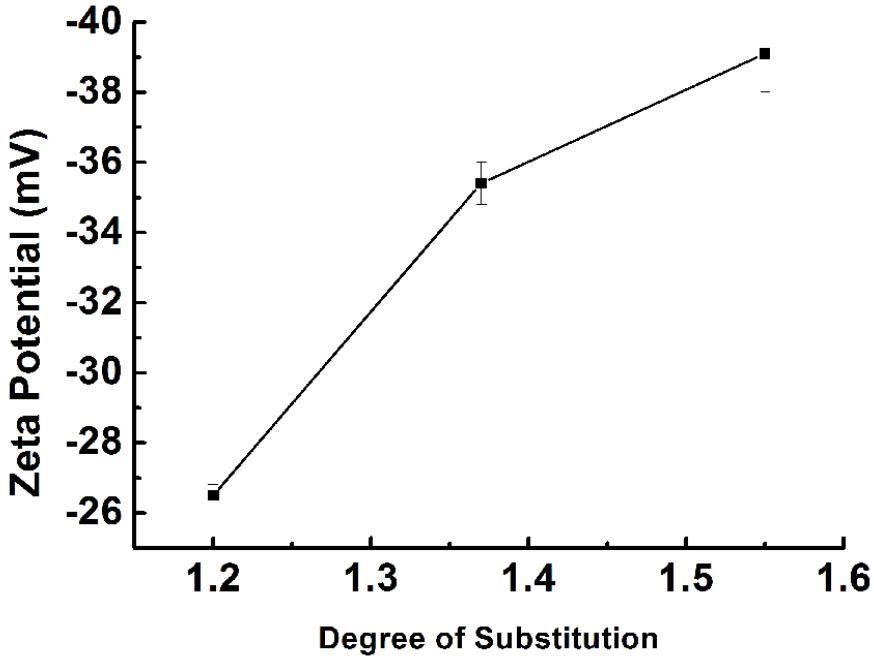

Figure 2.4. Zeta potentials of maleic chitosan with different degree of substitution (DS).

(Page 45, continued) This is probably due to the easy cleavage of relatively weak ionic links between methanesulfonic or tolunesulfonic anions and ionized amines.

Both methanesulfonic and toluenesulfonic chitosan salts have been utilized as intermediates for chemical synthesis of maleic chitosan either in formamide or DMSO in this study. The molecular weight, degree of substitution (DS) and yield of the final products ranged from 35,000 to 56,000; 0.58 to 1.53; and 69% to 89%, respectively, depending on the type of chitosan salt intermediates and solvents under optimum reaction conditions (shown in Table 2.2). Of the four systems examined, we concluded that formamide is a better solvent than DMSO, while toluenesulfonic chitosan salt is a better intermediate than methanesulfonic chitosan salt in terms of less degradation, and higher DS and yields of the final products.

The use of methanesulfonic or toluenesulfonic chitosan salts as intermediates enabled the chemical reaction of chitosan with maleic anhydride in a homogeneous reaction mixture in common organic solvents under a mild reaction condition. The average molecular weight (M_r) of chitosan (the starting material) is around 42,000; therefore, the general synthesis strategies reported here didn't cause significant backbone degradation, especially for the reaction systems in which formamide was used as solvent. The degree of substitution was also well controlled in our systems, and the maximum degree of substitution could reach as high as 1.53.

This level of degree of substitution in maleic chitosan is significantly higher than reported synthesis of cyclic anhydride chitosan derivatives including maleic chitosan [9,10,26,31,32]. For example: In gel-like mixed-solvents systems (lactic acid (acetic acid) /H_2O/MeOH= 1/20/80 (mL/mL/mL), Sashiwa et al. prepared maleic chitosan with a maximum degree of substitution 0.48 (no information for molecular weight) even using an excessive amount of maleic anhydride (12-fold in molar ratio of chitosan) [31]. The low degree of substitution in other reported studies could be due to

Table 2.2. Mw, Degree of Substitution and Yield of N, O-Maleic chitosan Prepared from Different Systems

System #	Intermediates	Solvent	Molecular Weight (M_r)	DS			Total DS	Yield (%)
				C-6 (O)	C-3 (O)	C-2 (N)		
1#	**$MeSO_3^-$ CN**	**DMSO**	**35,000**	**0.24**	**0.03**	**0.32**	**0.58**	**69**
2#	**TSO_3^- CN**	**DMSO**	**37,000**	**0.29**	**0.09**	**0.74**	**1.12**	**75**
3#	**$MeSO_3^-$ CN**	**Formamide**	**5,2000**	**0.32**	**0.07**	**0.75**	**1.15**	**86**
4#	**TSO_3^- CN**	**Formamide**	**5, 6000**	**0.64**	**0.10**	**0.80**	**1.53**	**89**

Note: DS= degree of substitution. All reactions were conducted under N_2 protection at 60 ^oC for 24hs, Molar ratio (Chitosan salt/maleic anhydride) =1:6.

inhomogeneous reaction conditions (gel-like system) and the presence of side reactions in the reaction systems, e.g., the reaction of cyclic anhydride with methanol and the hydrolysis of maleic anhydride in the presence of water.

One significant advantage of the proposed synthetic routes based on the chitosan salt intermediates is the easy removal of methanesulfonic or tolunesulfonic anions from the products in very mild conditions (in excess $NaHCO_3$ solutions, room temperature). The complete removal of the anions was confirmed both in FT-IR (Figure 2.3e) and NMR (Figure 2.2 c, e) spectra, as all the signals from the anions were gone in the spectra of the final products.

2.4.3 N-Maleic chitosan obtained via a hydrolysis strategy

Because ester bonds are more easily hydrolyzed than amide bonds under a basic condition, we employed the rule of regioselective modifications of chitosan at C-2 amino groups. A complete hydrolysis of the ester groups with little influence on the acetyl groups in a 0.1M sodium hydroxide solution resulted in N-maleic chitosan (see Scheme 2.1). ^{1}H and ^{13}C NMR spectra all indicate the complete removal of substituent groups at hydroxyl group sites, while the subsitituents at C-2 amino groups almost suffer no adverse effect under the same conditions (Figure 2.2a, b). The disappearance of the bands of ester groups at around 1730 cm^{-1} in the IR spectrum of N-maleic Chitosan further confirmed the complete removal of the substituent groups at the two C-6 and C-3 hydroxyl sites (Fig 2.3c). Hence, the hydrolysis strategy applied here made regioseletive modifications of chitosan at C-2 amino groups feasible.

2.5 Conclusion

Methanesulfonic (or tolunesulfonic) chitosan salt intermediates show excellent solubility in some polar solvents like water, formamide, and DMSO due to the destruction of the crystalline structure of chitosan and the presence of proper counter

anions. The organo-soluble chitosan salts are very promising as intermediates for various chemical modifications of chitosan, because the synthetic route for the salt intermediates is simple and efficient, the reaction conditions are very mild, and complete removal of salt anions can be easily achieved. The utility of these chitosan salts as intermediates for modifications of chitosan is demonstrated by the ring-opening reaction with maleic anhydride in a homogeneous organic solvent mixture. FT-IR, ^{1}H NMR, ^{13}C NMR and 2-D ^{1}H-^{1}H COSY confirm that the resulting product is N, O-maleic chitosan. More specifically, formamide is a better solvent than DMSO, whereas toluenesulfonic chitosan salt is a better intermediate than methanesulfonic chitosan salt in terms of higher molecular weight, DS, and yields of maleic chitosan.

The complete removal of ester groups on N, O-maleic chitosan by a hydrolysis strategy results in N-maleic chitosan. Hence, the simple synthetic route derived from the methanesulfonic (or tolunesulfonic) chitosan salt intermediates, coupled with a hydrolysis strategy in a basic solution, is expected to permit a wide range of regioselective N-acylation modifications of chitosan. Additional derivatives based on these chitosan salt intermediates are now being studied and will be reported in the future.

2.6 Acknowledgement

This research work was partially supported by the graduate student thesis funds from the College of Human Ecology at Cornell University and the Morgan Tissue Engineering Program. This work made use of the NMR facilities of the Cornell Chemistry department, and the XRD facility of the Cornell Center for Materials Research (CCMR) with support from the National Science Foundation Materials Research Science and Engineering Centers (MRSEC) program (DMR 0520404).

APPENDIX

^{1}H NMR and ^{13}C NMR of Methanesulfonic chitosan salts

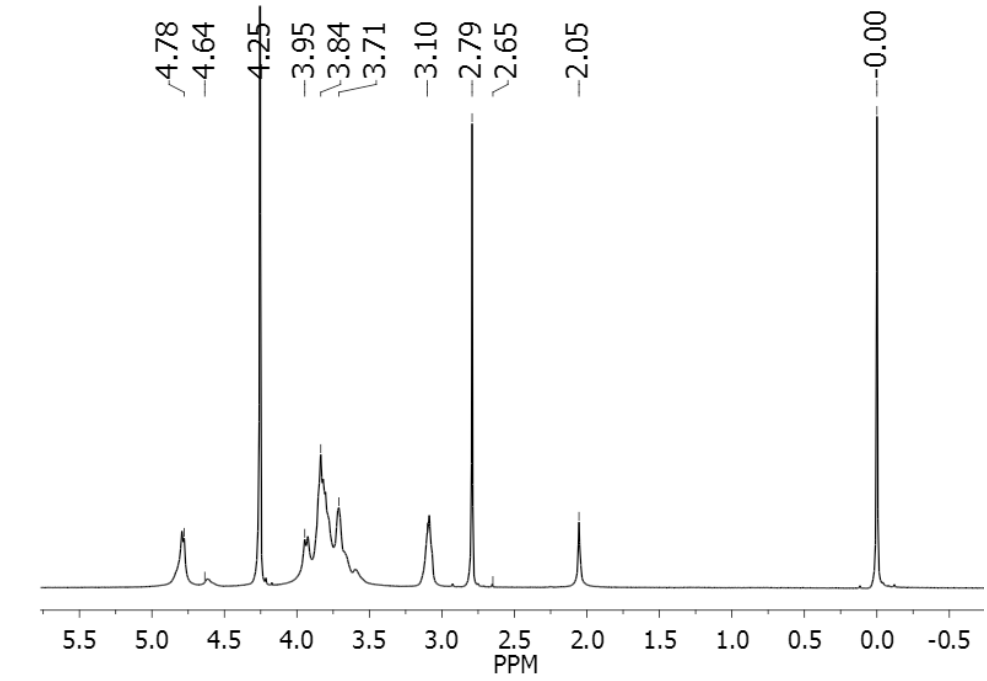

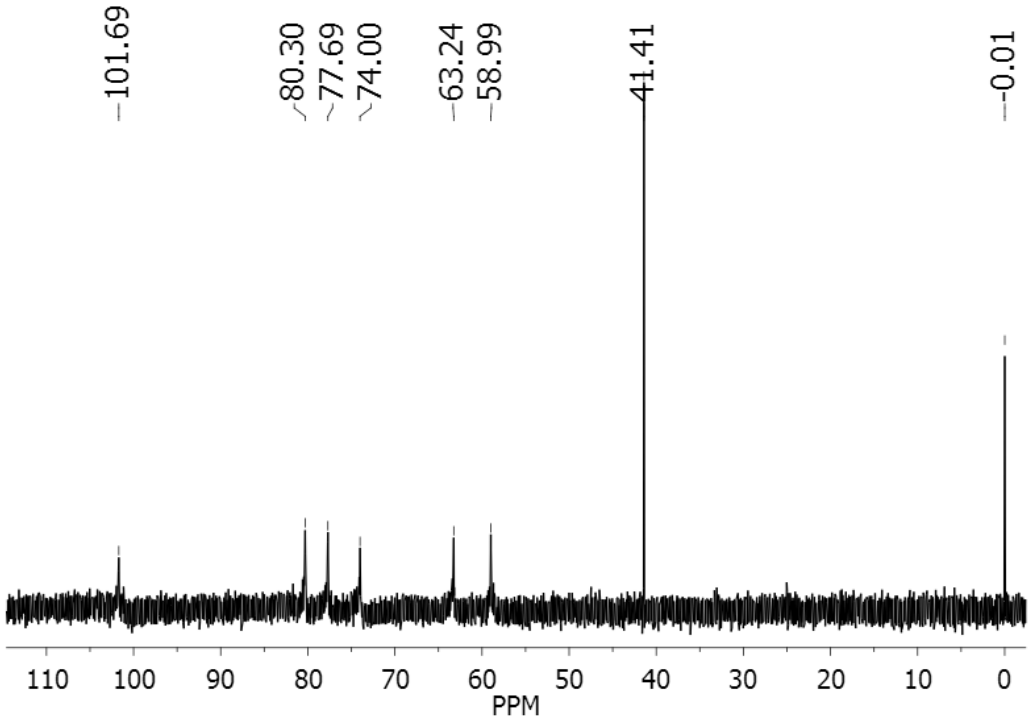

^{1}H NMR and ^{13}C NMR of Tolunesulfonic chitosan salts

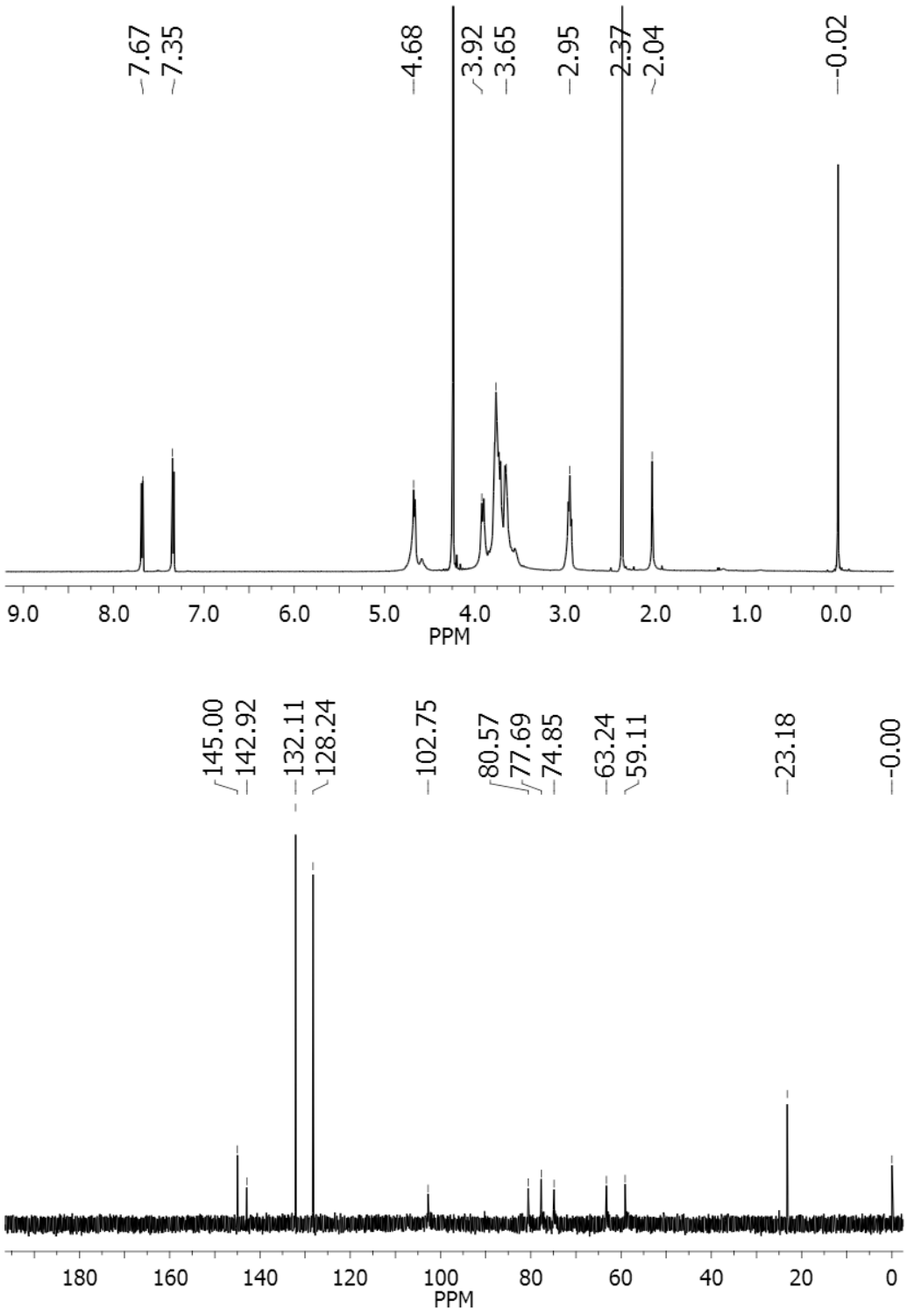

REFERENCES

1. Goosen, Mattheus F. A. Applications of Chitin and Chitosan. *Technomic, Lancaster, Pa* 1997: 3-5.

2. VandeVord PJ, Matthew HWT, DeSilva SP, Mayton L, Wu B, Wooley PH. Evaluation of the biocompatibility of a chitosan scaffold in mice. *Journal of Biomedical Materials Research* 2002;59(3):585-590.

3. Onishi H, Machida Y. Biodegradation and distribution of water-soluble chitosan in mice. *Biomaterials* 1999;20(2):175-182.

4. Felt O, Buri P, Gurny R. Chitosan: A unique polysaccharide for drug delivery. *Drug Development and Industrial Pharmacy* 1998;24(11):979-993.

5. Illum L. Chitosan and its use as a pharmaceutical excipient. *Pharmaceutical Research* 1998;15(9):1326-1331.

6. Paul W, Sharma CP. Chitosan, a drug carrier for the 21st century: a review. *Stp Pharma Sciences* 2000;10(1):5-22.

7. Devlieghere F, Vermeiren L, Debevere J. New preservation technologies: Possibilities and limitations. *International Dairy Journal* 2004;14(4):273-285.

8. Lim SH, Hudson SM. Review of chitosan and its derivatives as antimicrobial agents and their uses as textile chemicals. *Journal of Macromolecular Science-Polymer Reviews* 2003;C43(2):223-269.

9. Kumar M, Muzzarelli R A A, Muzzarelli C., Sashiwa H, Domb AJ. Chitosan chemistry and pharmaceutical perspectives. *Chemical Review* 2004, 104, 6017-6084.

10. Sashiwa H, Aiba SI. Chemically modified chitin and chitosan as biomaterials. *Progress in Polymer Science* 2004, 29(9):887-908.

11. Jayakumar R, Prabaharan M, Reis RL, Mano JF. Graft copolymerized chitosan - present status and applications. *Carbohydrate Polymers* 2005,62(2):142-158.

12. Kurita K, Yoshino H, Yokota K, Ando M, Inoue S, Ishii S, et al. Preparation of tosylchitins as precursors for facile chemical modifications of chitin. *Macromolecules* 1992;25(14):3786-3790.

13. Kurita K, Sannan T, Iwakura Y. Studies on chitin .3. preparation of pure chitin, poly(n-acetyl-d-glucosamine), from water-soluble chitin. *Makromolekulare Chemie-Macromolecular Chemistry and Physics* 1977;178(9):2595-2602.

14. Kurita K, Ichikawa H, Ishizeki S, Fujisaki H, Iwakura Y. Studies on chitin .8. modification reaction of chitin in highly swollen state with aromatic cyclic carboxylic-acid anhydrides. *Makromolekulare Chemie-Macromolecular Chemistry and Physics* 1982;183(5):1161-1169.

15. Kurita K, Yoshida A, Koyama Y. Studies on chitin. 13. new polysaccharide polypeptide hybrid materials based on chitin and poly(gamma-methyl l-glutamate). *Macromolecules* 1988;21(6):1579-1583.

16. Kurita K, Kamiya M, Nishimura SI. Solubilization of a rigid polysaccharide - controlled partial n-acetylation of chitosan to develop solubility. *Carbohydrate Polymers* 1991;16(1):83-92.

17. Kurita K, Yoshino H, Nishimura SI, Ishii S. Preparation and biodegradability of chitin derivatives having mercapto groups. *Carbohydrate polymers* 1993;20(4):239-245.

18. Nishimura SI, Kohgo O, Kurita K, Kuzuhara H. Chemospecific manipulations of a rigid polysaccharide - syntheses of novel chitosan derivatives with excellent solubility in common organic-solvents by regioselective chemical modifications. *Macromolecules* 1991;24(17):4745-4748.

19. Nishimura SI, Miura Y, Ren LD, Sato M, Yamagishi A, Nishi N, et al. an efficient method for the syntheses of novel amphiphilic polysaccharides by regioselective and thermoselective modifications of chitosan. *Chemistry Letters* 1993(9):1623-1626.

20. Kurita K, Shimada K, Nishiyama Y, Shimojoh M, Nishimura S. Nonnatural branched polysaccharides: Synthesis and properties of chitin and chitosan having alpha-mannoside branches. *Macromolecules* 1998;31(15):4764-4769.

21. Kurita K, Kojima T, Nishiyama Y, Shimojoh M. Synthesis and some properties of nonnatural amino polysaccharides: Branched chitin and chitosan. *Macromolecules* 2000;33(13):4711-4716.

22. Holappa J, Nevalainen T, Soininen P, Elomaa M, Safin R, Masson M, et al. N-chloroacyl-6-O-triphenylmethylchitosans: Useful intermediates for synthetic modifications of chitosan. *Biomacromolecules* 2005;6(2):858-863.

23. Holappa J, Nevalainen T, Savolainen J, Soininen P, Elomaa M, Safin R, et al. Synthesis and characterization of chitosan N-betainates having various degrees of substitution. *Macromolecules* 2004;37(8):2784-2789.

24. Roberts GAF, Domszy JG. Determination of the viscometric constants for chitosan. *International Journal of Biological Macromolecules* 1982;4(6):374-377.

25. Khor, E. *Chitin: fulfilling a biomaterials promise*，Elsevier, Amsterdam, Neth, 2001: 83-84.

26. Kurita K. Controlled functionalization of the polysaccharide chitin. *Progress in Polymer Science* 2001;26(9):1921-1971.

27. Saito H, Tabeta R, Hirano S. Conformation of chitin and n-acyl chitosans in solid-state as revealed by c-13 cross polarization magic angle spinning (cp-mas) nmr-spectroscopy. *Chemistry Letters* 1981(10):1479-1482.

28. Saito H, Tabeta R, Ogawa K. High-resolution solid-state c-13 nmr-study of chitosan and its salts with acids - conformational characterization of polymorphs and helical structures as viewed from the conformation-dependent c-13 chemical-shifts. *Macromolecules* 1987;20(10):2424-2430.

29. Kurita K, Ikeda H, Yoshida Y, Shimojoh M, Harata M. Chemoselective protection of the amino groups of chitosan by controlled phthaloylation: Facile preparation of a precursor useful for chemical modifications. *Biomacromolecules* 2002;3(1):1-4.

30. C. Reichardt, Solvatochromic dyes as solvent polarity indicators, *Chemical Review* 1994, 94, 2319-2358.

31. Sashiwa H, Shigemasa Y. Chemical modification of chitin and chitosan-2: preparation and water soluble property of N-acylated or N-alkylated partially deacetylated chitins. *Carbohydrate Polymers* 1999;39(2):127-138

32. Zhu AP, Pan YN, Liao TQ, Zhao F, Chen T. The synthesis and characterization of polymerizable and Biocompatible N-maleic acyl-chitosan. *Journal of Biomedical Materials Research Part B* 2008;85(2):489-495.

CHAPTER 3

ACID POLYSACCHARIDE-INDUCED AMORPHOUS CALCIUM CARBONATE (ACC) FILMS: COLLOIDAL NANOPARTICLE SELF-ORGANIZATION PROCESS

*Chao Zhong† and C. Chang Chu†, ‡,**

Fiber and Polymer Science Program, Department of Fiber science and Apparel design, Cornell University, Ithaca, New York 14853-4401

Biomedical Engineering Program, Cornell University, Ithaca, New York 14853-4401

Email: cc62@cornell.edu*

† Department of Fiber science

‡ Biomedical Engineering Program

* To whom correspondence should be addressed. Phone: (607) 255-1938, Fax: (607) 255-1093.

Langmuir 2009, 25, 3045-3049 (Published).

3.1 Abstract

Amorphous calcium carbonate (ACC) plays important roles in biomineralization, and its synthesis in vitro has been of keen interest in the field of biomimetic materials. In this report, we describe the synthesis of ACC films using a novel acid polysaccharide, maleic chitosan, as an additive. We prepared the films by directly depositing them onto TEM grids and examined them using Polarized Optical Microscopy (POM), Scanning Electron Microscopy (SEM) and Transmission Electron Microscopy (TEM) combined with Selected Area Electron Diffraction (SAED). This enabled us to examine their formation and mesostructure without introducing artifacts. We observed that in the presence of maleic chitosan, the ACC films are formed through particles buildup process, with aggregation and coalescence occurring simultaneously. Nanoparticles with size less than 10nm appear to be the basic units responsible for such self-organization. We suggest that the acid polysaccharide plays an important role in forming and stabilizing these nanoparticles, and we propose a colloidal nanoparticle self-organization model to explain the formation of the ACC films.

Keywords Amorphous Calcium Carbonate (ACC), Biomimetic Materials Synthesis, Biomineralization and Acid Polysaccharide

3.2 Introduction

Amorphous calcium carbonate (ACC) is one of the six known forms of calcium carbonate. Albeit unstable in its pure form under ambient conditions, ACC, like its crystalline polymorphs, can be produced, utilized, and stabilized by many biological organisms from different taxa [1, 2]. It is also known that ACC has important functions in biominerals and biomineralization process. For example, it can be used as temporary storage deposits [1, 3] and structural skeletal elements [1, 4, 5]. Recent evidence also shows that ACC acts as a transient precursor to its two major crystalline polymorphs, calcite and aragonite [6-10]. Biological occurrences of ACC usually involve organic macromolecules and, sometimes, magnesium and phosphate, factors that may contribute to the stabilization of ACC [2, 11].

Inspired by such findings, and trying to understand the biological mechanisms of ACC stabilization, several studies have synthesized ACC in the presence of additives and/or templates [12,13]. For example, ACC phase with stability over periods ranging from hours to months has been achieved by the addition of magnesium [14,15], self-assembled monolayer (SAMs) [12,16,17], biological macromolecules [4,5], synthetic polymers[18-23] and even small-molecules[24]. Stable continuous ACC or crystalline films transformed by ACC precursors are of particular interest because they provide an environmentally friendly process for fabricating ceramic films [19]. Examples include: the use of amphiphilic porphyrin templates coupled with poly (acrylic acid) to prepare thin continuous calcium carbonate films [25]; the preparation of a polypeptide-stabilized ACC film using an unconventional crystallization process called “polymer-induced liquid precursor” (PILP) [20]; and, the fabrication of a mm-sized single calcite film via the transformation of metastable ACC films on micropatterned self-assembled monolayers (SAMs) [16].

We are interested in understanding the stabilization of ACC in biological systems, and although there are reports using synthetic polymers to stabilize ACC phase, most of them do not use polymers that have direct biological relevance. Accordingly, we chose to use a synthetic acid polysaccharide, maleic chitosan (a derivative of chitin, Figure 3.1), as an organic additive to induce ACC film formation. Acid polysaccharides rich in either carboxyl or sulfated groups have been found to control the formation and morphology of corresponding biominerals in some organisms [26-30], and it has been suggested that sugar moieties in some biogenic macromolecules is a possible factor in stabilizing ACC both in vitro and vivo [4, 31]. And yet despite their importance in the field of biomineralization, polysaccharide macromolecules have received very little attention in vitro studies of calcium carbonate mineralization, and virtually no work has used polysaccharides to produce and stabilize ACC phase.

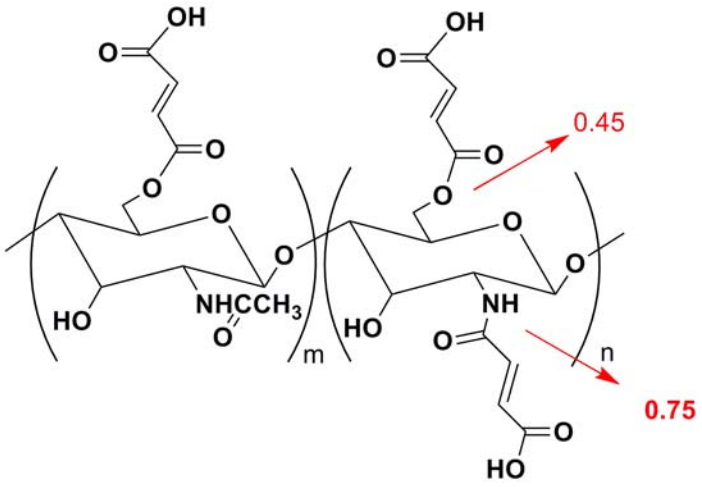

Figure 3.1. Chemical Structure of Maleic Chitosan

Despite the previous work on the synthesis of ACC films, the formation and mesostructure of ACC films are still not well understood. It has widely been accepted that ACC film formation occurs when preformed polymer-induced liquid precursor

(PILP) droplets (2~4μm) wet the substrate and spread into film form [20]. But in the absence of an adequate investigation of ACC film mesostructure, we believe it is premature to accept this statement about ACC film formation. Accordingly, we set out to examine the formation and the mesostructure of ACC films using a new approach. In particular, we used maleic chitosan as an organic additive to directly induce ACC films formation onto TEM grids followed by probing their mesostructure using TEM combined with Selected Area Electron Diffraction (SAED). Previous work has shown TEM to be a useful tool for studying ACC precursor structures [32] and the nucleation of $CaCO_3$ crystallization at an early stage [33].

Our studies may contribute to the understanding of biological mechanisms in ACC stabilization. We believe that our studies will provide insights into the general formation mechanism of ACC films in the presence of additive/template systems.

3.3 Experimental Section

3.3.1 ACC films precipitation

All chemicals are of analytical grade and used as received from Sigma. TEM grids (G300H-Cu, 300 Mesh Hex) were purchased from Electron Microscopy Sciences. All small pieces of glass cover slips were cleaned and sonicated in ethanol, rinsed with double distilled water, and dried with a constant flow of N_2. The formation of amorphous $CaCO_3$ was carried out in small petri dishes (5mL), which were put in a closed desiccator at room temperature (22°C). In a typical procedure, 75 μL 10 mg/mL maleic chitosan solution was injected into 3mL of 50mM $CaCl_2$ solution (filtered by a micro-filter with pore size of 40μm) in a 10mL clean centrifuge tube. After being mixed homogeneously in the tube for 1 minute, the solution was transferred into the 5mL petri dish. Next, a glass slide (18mm) or TEM grid was carefully put into the petri dish for collecting amorphous phase (floating on the surface

of the solution). After that, the bottles were covered with parafilm, which was punched with three needle holes, and placed in a larger desiccator. Three small glass bottles (15 mL) of crushed ammonium carbonate were also covered with parafilm punched with one-needle hole in the center and placed at the bottom of the desiccator. The formation of ACC usually took place within 1 hour; samples were thus collected at 30mins and 40mins. (When stored in a vacuum, ACC films can be stabilized for at least 3 months.) At 50mM $CaCl_2$, ACC films can be formed within polymer concentration range of 30-500μg/mL, but the amount of ACC films collected varies. We thus choose an intermediate concentration (243.9μg/mL) within this range to study the self-organization process. In control experiments without maleic chitosan, rhombohedral calcite crystals were collected after 40 mins.

3.3.2 Characterization

FTIR: Infrared Spectroscopy (IR) was performed in a Microscopy–continuum mode. Samples were analyzed using a Perkin Elmer Spectrum One FT-IR spectrometer.

SEM: The morphology of the obtained samples was examined by scanning electron microscopy (KECK FE-SEM, LEO 1550 (Schottky Field Emitter)) after being sputter-coated with Au/Pd. The experiments were performed at a low accelerating voltage (3 KeV), especially suitable for imaging the surface detail of low-density materials.

POM (Polarized Optical Microscope): Fresh samples formed on glass slides or TEM grids were directly observed using a polarized optical microscope (Zeiss) equipped with cross-polarizers in the transmission mode. Some of these optical micrographs were taken with the insert of the first-order red λ-plate so that both birefringent and isotropic matter can be viewd in cross-polarized light.

TEM: Samples were directly formed on TEM carbon grids, and then loaded using a single tilt holder. TEM was performed on a FEI Technai T12 at 120 kV, and selected area electron diffraction (SAED) was recorded using the same equipment.

3.4 Results & Discussion

The calcium carbonate precipitation was achieved using an ammonium carbonate diffusion method. Typical SEM morphology of ACCs formed at 30mins on a glass slide is shown in Figure 3.2a. It is a continuous film with thickness less than 1μm. The corresponding optical micrograph is shown in Figure 3.2b. The amorphous feature of the whole film was confirmed by polarized optical microscopy (Figure 3.2c, and d). Figure 3d reveals that the films were seen as the same color as the background when the first-order red λ-plate with cross-polars was used, revealing isotropic feature [19]. The ACC characteristics of the structure is further confirmed by the FT-IR spectrum, which reveals the presence of carbonate out-of-plane bending adsorption at 866 cm^{-1} (ν_2), the symmetric stretch in noncentrosymmetric structure expressed by the presence of a broad peak at 1080cm^{-1} (ν_1), and the splitting at 1420 and 1474cm^{-1} of the peak due to the asymmetric stretch of the carbonate ion (Figure 3.3) [1].

It is difficult to prepare very thin samples of ACC film for TEM characterization due to the rapid transformation of ACC into its crystalline phase during the microtome process. Accordingly, we decided to form ACC films directly onto TEM grids by floating the grids onto a crystallization solution. This approach also precludes artifacts produced during sample preparation via microtomy. ACC films can even be formed in the solution without the assistance of any substrate. Although the surface properties of glass slides and TEM grids are different, these differences did not affect the deposition of ACC films onto them.

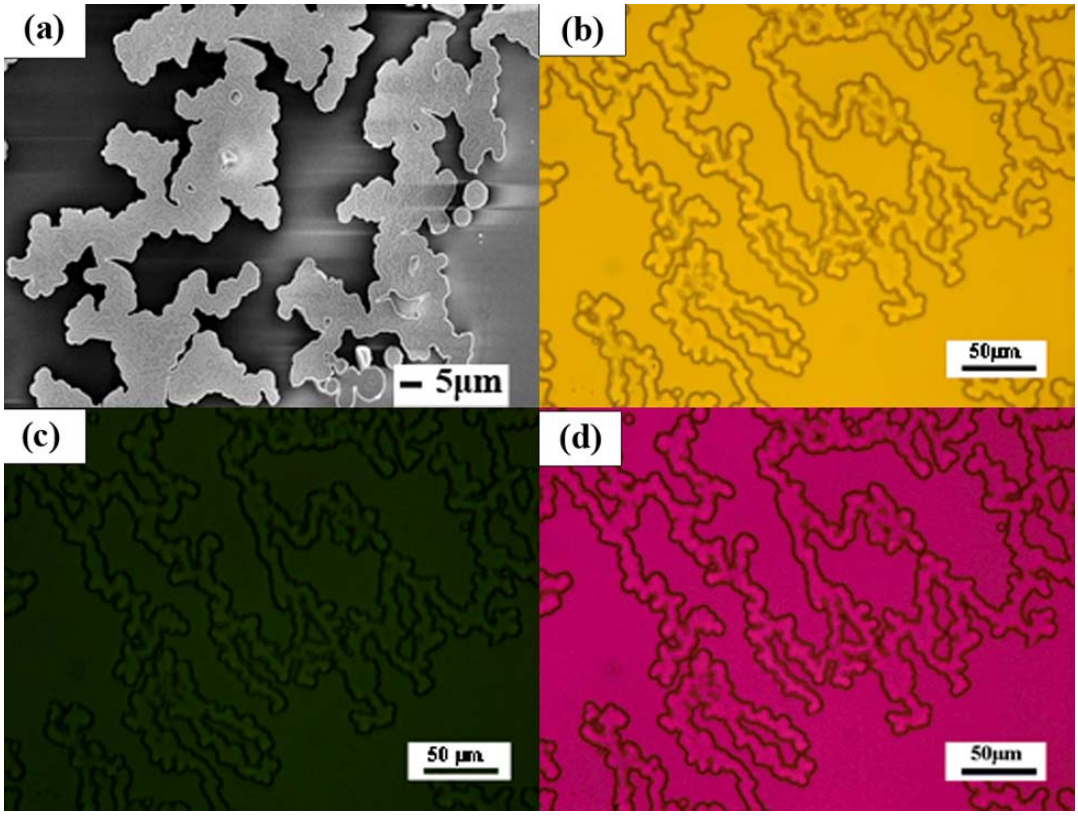

Figure 3.2. SEM and optical micrograph of ACC films collected on glass slide. (a) SEM image, (b) optical microscopy (c) cross-polarized optical microscopy (d) cross-polarized optical microscopy with the first-order red λ-plate inserted. The films, seen as same color as the background when using the first-order red λ-plate with cross-polars, indicates an isotropic features.

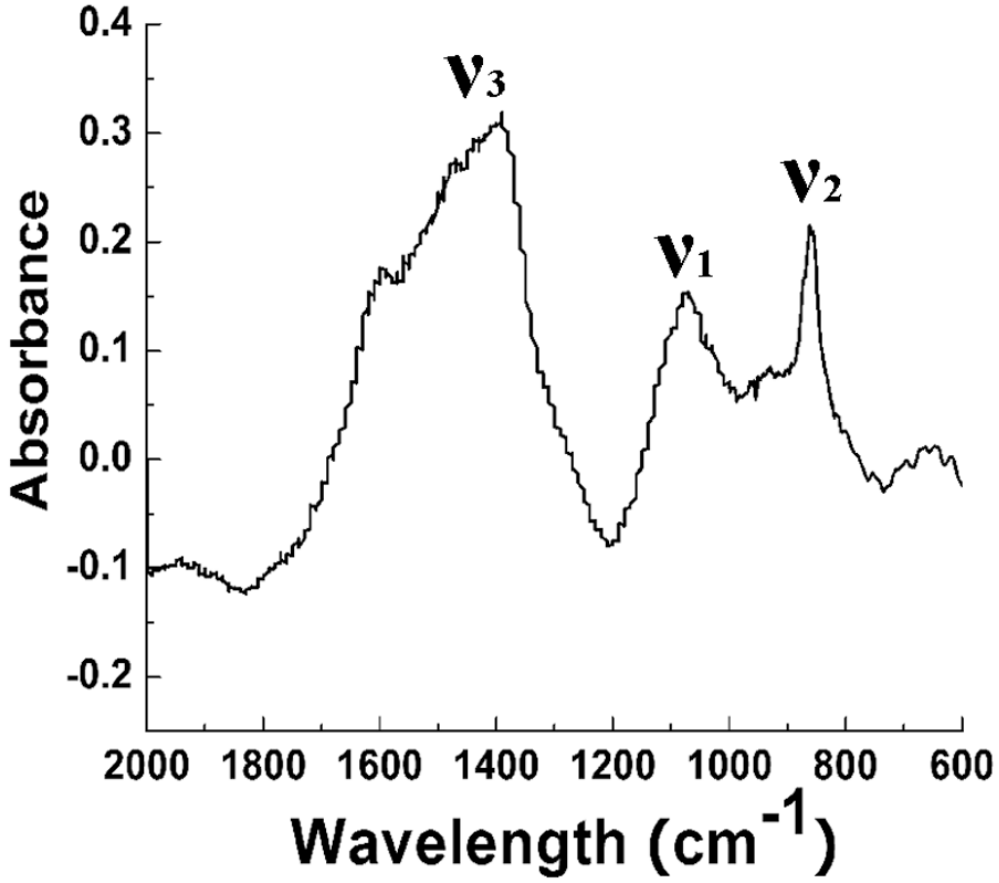

Figure 3.3. FTIR spectra of amorphous calcium carbonate film collected from the glass slide.

Figure 3.4. SEM and Crossed-polarized microscopy micrographs of amorphous calcium carbonate (ACC) films directly deposited on TEM grids at different time intervals. (a-f) 40min sample; e is the magnified picture of selected area in d (white arrow point to), the grain boundaries between particles are clearly seen (the white arrows in e). (g-i) 30min sample, examined from the deposition site. The ACC grows toward the open area even without the presence of a substrate (the white arrow in h).

a
1μm
30μm
b
30μm
c
30μm
d
40μm
e
5μm
f
1μm
g
30um
h
20μm
i
1μm

Figure 3.4 displays the morphology typical of the films deposited on TEM grids after 30 and 40mins. Moreover, they exhibit morphology similar to the films we obtained on glass slides (based on light microscopy and SEM images, as shown in Figure 3.2 and 3.2d). The amorphous feature of both films is confirmed by cross-polarized optical microscopy (Figure 3.4c, and Figure 3.5). After a deposition time of 40mins, continuous amorphous films with thickness about 1~2μm typically covered the whole TEM grid (Figure 3.4a and 3.4a insert). In some cases, the films have not yet been fully integrated, as indicated by the presence of boundaries between neighboring spherical particles with size around 2μm (Figure 3.4e). It is thus conceivable that the continuous integrated films formed through a gradual buildup of many small particles around 2μm. The 30min sample, examined from the deposition side, provides further insight into how the continuous films were formed. The whole film has a patterned morphology (Figure 3.4g). The formation of such pattern apparently originates from the grid pattern due to initial deposition of ACC phase along the rim, followed by gradual growth of more ACC phase towards the open area (Figure 3.4h). In addition, the ACC phase directly deposited on the rim exhibited a smooth surface due to full coalescence of the particles, whereas those close to the open areas had a rough surface, indicated by similar traces of boundaries as 40min sample, as a result of incomplete coalescence (Figure 3.4h). Accordingly, we believe that the films are formed through a gradual buildup of smaller particles (1-2μm), with aggregation and coalescence occurring synchronously. This observation does not imply, however, that the 2μm particles are necessarily the basic units for such aggregation and coalescence. Indeed, SEM images of higher magnification, shown in Figures 3.4f and 3.4i, reveal that these spherical particles are actually constructed from many smaller subunits around 100~200nm.

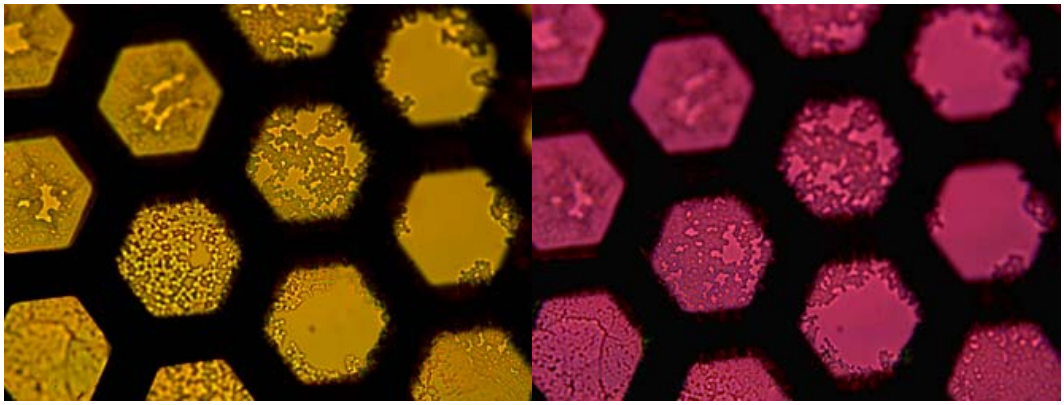

Figure 3.5. Optical and cross-polarized optical microscopy images of 40min ACC sample. (a) Optical microscopy image, (b) cross-polarized optical microscopy with the first-order red λ-plate inserted.

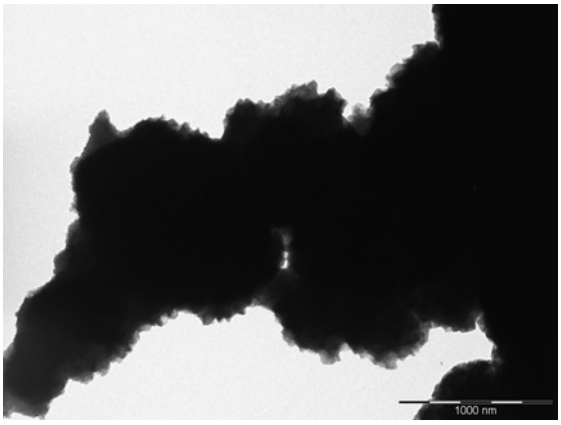

Figure 3.6. TEM micrograph of 40 min samples showing that the 40min sample obtained is always very thick for TEM observation.

Our next step was to investigate the mesostructure of the ACC films using TEM. For the 40min sample, the detailed structure was hard to detect due to the thickness of the films (Figure 3.6). However, we did find some thin area in the 30min sample, composed of many particle clusters (Figure3.7a). The size of each particle is around 100~200nm, similar to the size of those particles we observed from SEM

image (Figure 3.4f, i). The amorphous feature of these nanoparticles was confirmed by the appearance of diffuse rings in the SAED pattern (Figure 3.7a insert). In some thinner areas, particularly those close to the film edges, even smaller particles were observed across sites (Figure 3.7b). Indeed, TEM of higher magnification (Figure 3.7c), reveals that these nanoparticles are less than 10nm and tend to form a continuous but "disordered" nano-film structure. It may be that the polysaccharide on their surfaces assists this aggregation. Similar observations can be extended to the film edges of different locations (Figure 3.7d, e). It is thus conceivable that these smallest particles are the basic units to construct the whole films. Interestingly, in some cases, individual mesopores with diameter ranging from 10 to 50nm were sometimes observed to be embedded inside these nanoparticles (Figure 3.7f). It is not clear how such pores are formed, although the SAED pattern around the pore area also indicates its amorphous feature (Figure 3.7f insert). We suspect that the presence of these pores might be associated with colloidal nanoparticles self-assembly processes.

There are reports in the literature that describe the formation of amorphous calcium carbonate films or crystalline films transforming via ACC film in the presence of acid polymer (poly-aspartic acid) [19, 20]. The capture of pure amorphous calcium carbonate films before the phase transformation was not achieved in the reports. It was however suggested that preformed polymer-induced liquid precursor (PILP) droplets (2~4μm) settle and subsequently wet the substrate and spread into a film form [20]. This suggestion was based on optical microscopy and SEM results. More recently, Rieger et al. have studied precursor structures in the precipitation processes of $CaCO_3$ by mixing 0.01M solutions of $CaCl_2$ and Na_2CO_3 in the presence of polycarboxylic acid [32]. They have found that, from an emulsion-like or phase-separated structure formed at the very beginning (obtained within 100ms, and information about the chemical components is not known), ACC nanoparticles formed and then built into

Figure 3.7. TEM pictures of 30min amorphous calcium carbonate (ACC) film sample directly deposited on TEM grids (a) typical structure image of 30-min sample. (a insert) SAED pattern of 30min sample, the selected area is indicated in white dotted line as shown in (a). (b) typical structure image of 30min sample examined at thin edges showing multi-scale sizes of nanoparticles. (c) detailed mesostructure around the thin edges showing nanoparticles less than 10nm. These nanoparicles aggregate to form nano-film structure. (d-f) more TEM images examined at different sites of thin edges of the 30min sample. Similar mesoporous structures constructed from nanoparticles less than 10nm are found. (f inserted) Corresponding SAED pattern of films shown in f. The selective area is indicated as white dotted line in f.

a
1μm
b
200nm
c
30nm
d
100nm
e
100nm
f
200nm

floc structure, probably interconnected by the polymer coatings. In contrast, we also observed film-like structures in our studies even though we did not detect any emulsion-like structure even in the samples we collected at earlier stage (for example 5-10min samples). Moreover, our results seem to support the hypothesis that the films are formed through a gradual dynamic buildup of particles with different sizes (ranging from nanometers to microns), an inference based on the combined results from SEM, optical microscopy and TEM. These films can even be formed around the open area of TEM grid, which does not have a substrate to support its deposition (Figure 3.4 a, d).

Accordingly, we propose a colloidal nanoparticle self-organization model to explain the formation of continuous ACC films. This is illustrated in Scheme 3.1. At the initial stage, the acid polysaccharide molecules sequester and concentrate the ionic species and inhibit crystallization. It is likely that phase separation takes place at this stage. The resulting phase-separated structures might be highly hydrated and not easily collected under normal conditions. ACC nanoparticles less than 10nm then appeared and were stabilized by acid polysaccharide molecules as local supersaturation increases. These ACC nanoparticles tend to aggregate to form nanoclusters, and then self-organize into larger particles (100-200nm), and these bigger particles, in turn, first aggregate to form bigger particle clusters and then self-organize into 2-3μm particles. Further self-organization process between particles and/or particle clusters (including small/small particles or clusters, small/big particles or clusters, and big/big particules or clusters) finally leads to the formation of a continuous ACC film. It is interesting to note that the phenomenon of nanoparticles and nanoclusters formation via aggregation has previously been observed in surfactant-stabilized ACC-containing reverse microemulsions [34], and in several other solution systems including silica [35], aluminum ions [36] and other large cations [37]. There is increasing evidence that

Scheme 3.1. Proposed Colloidal Nanoparticles Self-Organization Model to Explain the Formation of Amorphous Films in the Presence Of Acid Polysaccharide

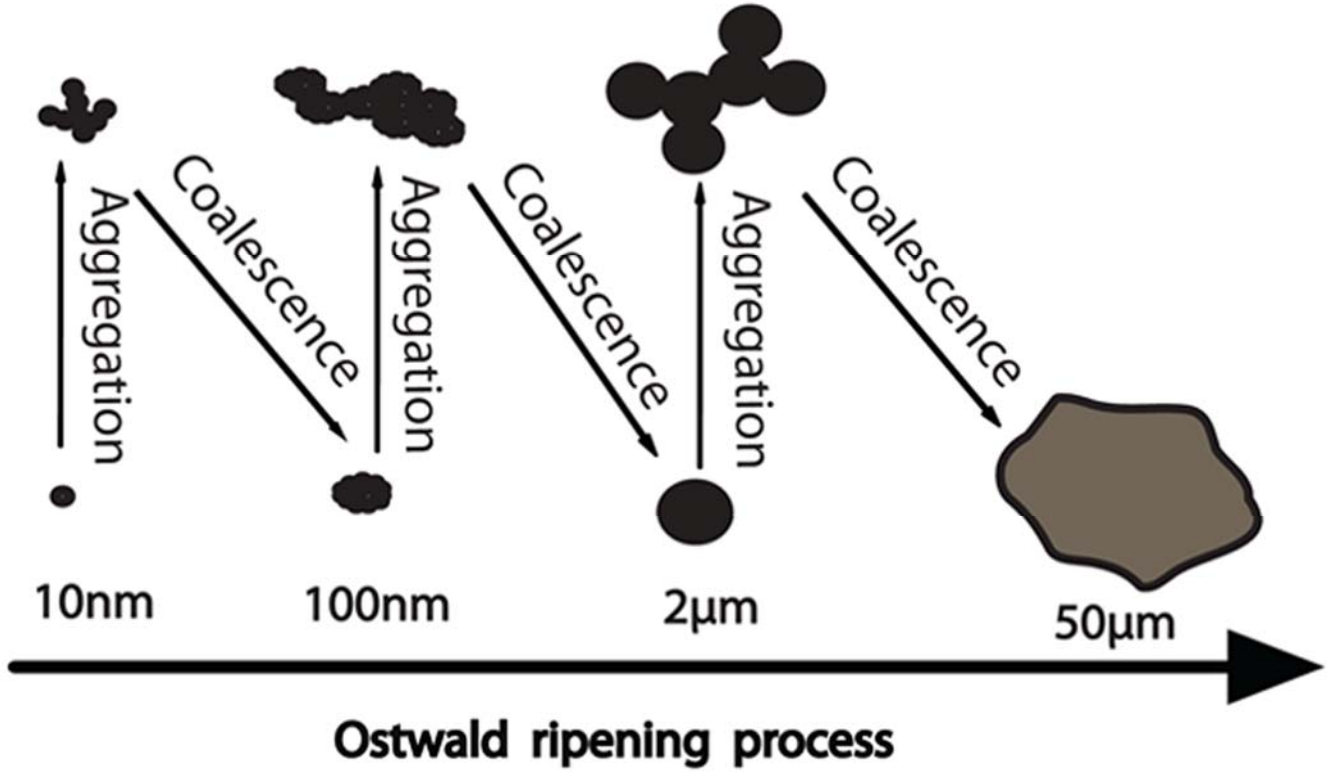

nanocluster precursors in the aqueous phase may play an important role in crystallization and biomineralization [38].

The process of self-organization associated with the general trend toward a minimal interfacial area (thus a minimal interfacial energy) between the dispersed phase of small particles or particle clusters and the dispersion medium. This is primarily achieved by coagulation followed by coalescence. It is also possible that the functionalized surface of nanoparticles/nanoclusters assists in the self-organization, although very little is known about the surface at this point. Finally, the self-organization process obeys the Ostwald ripening process in which larger ACC colloidal particles grow at the expense of smaller ones due to particle diffusion through the continuous phase.

3.5 Conclusions

We have demonstrated that ACC films can be formed in the presence of a novel synthetic acid polysaccharide template. We believe that this is the first report using an acid polysaccharide as an additive to prepare ACC films. By direct deposition of the ACC films onto TEM grids, we have successfully used TEM in combination with SAED to characterize the mesostructure of the formed ACC films. We propose a colloidal nanoparticle self-organization model to explain the formation of the continuous ACC films. Our studies indicate that polysaccharide macromolecules, particularly acid polysaccharides, are potential resources for producing stable ACC films. More generally, we believe these several findings and our self-organization model provide insight into the formation of ACC films in the presence of additive/template systems.

3.6 Acknowledgment

The authors thank Professor Lara Estroff from Cornell's Department of Materials Science for help with the crystallization set-up and for providing insightful suggestions. This project was partially supported by graduate student thesis funds from the School of Human Ecology at Cornell University. This work made use of the electron microscopy (SEM and TEM) facilities of the Cornell Center for Materials Research (CCMR) with support from the National Science Foundation Materials Research Science and Engineering Centers (MRSEC) program (DMR 0520404).

APPENDIX

Synthesis and Chemical structure of maleic chitosan

Synthesis of Maleic Chitosan:

The synthesis of maleic chitosan was carried out using a novel approach developed in our own group (Provisional U.S. patent filed). The starting material, chitosan (Sigma product) has 75% degree of deacetylation, with Brookfield viscosity 20.0-200cps (1% acetic acid). Briefly, 1.0 g methanesulfonic chitosan salts were dissolved in 100mL DMSO solvent under stirring at room temperature. Solid maleic anhydride of 6-fold in molar ratio was then added to the solution, and the reaction mixture was stirred under N_2 at 60 °C for 24 hrs. The resulting product in the solution was precipitated out by acetone, filtered, washed with copious amounts of acetone, and dried. Methanesulfonic (or tolunesulfonic) anions in the product were then removed from the chitosan salts by adding 0.1M $NaHCO_3$ solution. Finally the solution was dialyzed against deionized water (MW cut off 12,000) and lyophilized to yield 69% of the products. Degree of Substitution of Maleic chitosan=1.2, with N-2 and O-6 substitution 0.75 and 0.45, respectively. Molecular weight (M_n) =56,000.

REFERENCES

1. Addadi L, Raz S, Weiner S. Taking advantage of disorder: Amorphous calcium carbonate and its roles in biomineralization. *Advanced Materials* 2003;15(12):959-970.

2. Weiner S, Levi-Kalisman Y, Raz S, Addadi L. Biologically formed amorphous calcium carbonate. *Connective Tissue Research* 2003;44:214-218.

3. Raz S, Testeniere O, Hecker A, Weiner S, Luquet G. Stable amorphous calcium carbonate is the main component of the calcium storage structures of the crustacean Orchestia cavimana. *Biological Bulletin* 2002;203(3):269-274.

4. Aizenberg J, Lambert G, Addadi L, Weiner S. Stabilization of amorphous calcium carbonate by specialized macromolecules in biological and synthetic precipitates. *Advanced Materials* 1996;8(3):222-225.

5. Aizenberg J, Weiner S, Addadi L. Coexistence of amorphous and crystalline calcium carbonate in skeletal tissues. *Connective Tissue Research* 2003;44:20-25.

6. Beniash E, Aizenberg J, Addadi L, Weiner S. Amorphous calcium carbonate transforms into calcite during sea urchin larval spicule growth. *Proceedings of the Royal Society of London Series B-Biological Sciences* 1997;264(1380):461-465.

7. Raz S, Hamilton PC, Wilt FH, Weiner S, Addadi L. The transient phase of amorphous calcium carbonate in sea urchin larval spicules: The involvement of proteins and magnesium ions in its formation and stabilization. *Advanced Functional Materials* 2003;13(6):480-486.

8. Politi Y, Arad T, Klein E, Weiner S, Addadi L. Sea urchin spine calcite forms via a transient amorphous calcium carbonate phase. *Science* 2004;306 (5699):1161-

1164.

9. Ma Y, Weiner S, Addadi L. Mineral deposition and crystal growth in the continuously forming teeth of sea urchins. *Advanced Functional Materials* 2007;17:2693-2700.

10. Weiss IM, Tuross N, Addadi L, Weiner S. Mollusc larval shell formation: Amorphous calcium carbonate is a precursor phase for aragonite. *Journal of Experimental Zoology* 2002;293(5):478-491.

11. Lam RSK, Charnock JM, Lennie A, Meldrum FC. Synthesis-dependant structural variations in amorphous calcium carbonate. *Crystengcomm* 2007;9:1226-1236.

12. Han YJ, Aizenberg J. Calcium carbonate storage in amorphous form and its template-induced crystallization. *Chemistry of Materials* 2008;20:1064-1068.

13. Faatz M, Grohn F, Wegner G. Amorphous calcium carbonate: Synthesis and potential intermediate in biomineralization. *Advanced Materials* 2004;16(12):996-1000.

14. Loste E, Wilson RM, Seshadri R, Meldrum FC. The role of magnesium in stabilising amorphous calcium carbonate and controlling calcite morphologies. *Journal of Crystal Growth* 2003;254(1-2):206-218.

15. Ajikumar PK, Wong LG, Subramanyam G, Lakshminarayanan R, Valiyaveettil S. Synthesis and characterization of monodispersed spheres of amorphous calcium carbonate and calcite spherules. *Crystal Growth & Design* 2005;5(3):1129-1134.

16. Aizenberg J, Muller DA, Grazul JL, Hamann DR. Direct fabrication of large micropatterned single crystals. *Science* 2003;299(5610):1205-1208.

17. Lee JRI, Han TY-J, Willey TM, Wang D, Meulenberg RW, Nilsson J, et al. Structural Development of Mercaptophenol Self-Assembled Monolayers and the Overlying Mineral Phase during Templated CaCO3 Crystallization from a Transient Amorphous Film. *Journal of the American Chemical Society* 2007;129(34):10370-10381.

18. Xu XR, Han JT, Cho K. Formation of amorphous calcium carbonate thin films and their role in biomineralization. Chemistry of Materials 2004;16(9):1740-1746.

19. Gower LA, Tirrell DA. Calcium Carbonate films and helices grown in solutions of poly(aspartate). *Journal of Crystal Growth* 1998;191:153-160.

20. Gower LB, Odom DJ. Deposition of calcium carbonate films by a polymer-induced liquid-precursor (PILP) process. *Journal of Crystal Growth* 2000;210:719-734.

21. Donners JJJM, Heywood BR, Meijer EW, Nolte RJM, Roman C, Schenning APHJ, et al. Amorphous Calcium Carbonate Stabilised by Poly(propylene imine) dendrimers. *Chemical Communications* 2000:1937-1938.

22. Bolze J, Peng B, Dingenouts N, Panine P, Narayanan T, Ballauff M. Formation and growth of amorphous colloidal CaCO3 precursor particles as detected by time-resolved SAXS. *Langmuir* 2002;18(22):8364-8369.

23. Bolze J, Pontoni D, Ballauff M, Narayanan T, Colfen H. Time-resolved SAXS study of the effect of a double hydrophilic block-copolymer on the formation of CaCO3 from a supersaturated salt solution. *Journal Of Colloid And Interface Science* 2004;277(1):84-94.

24. Xu AW, Yu Q, Dong WF, Antonietti M, Colfen H. Stable amorphous CaCO3

microparticles with hollow spherical superstructures stabilized by phytic acid. *Advanced Materials* 2005;17(18):2217-2221.

25. Xu GF, Yao N, Aksay IA, Groves JT. Biomimetic synthesis of macroscopic-scale calcium carbonate thin films. Evidence for a multistep assembly process. *Journal of the American Chemical Society* 1998;120(46):11977-11985.

26. Ozaki N, Sakuda S, Nagasawa H. A novel highly acidic polysaccharide with inhibitory activity on calcification from the calcified scale "coccolith" of a coccolithophorid alga, Pleurochrysis haptonemofera. *Biochemical and Biophysical Research Communications* 2007;357(4):1172-1176.

27. Albeck S, Weiner S, Addadi L. Polysaccharides of intracrystalline glycoproteins modulate calcite crystal growth in vitro. *Chemistry-a European Journal* 1996;2(3):278-284.

28. Andrade LR, Salgado LT, Farina M, Pereira MS, Mourao PAS, Filho GMA. Ultrastructure of acidic polysaccharides from the cell walls of brown algae. *Journal of Structural Biology* 2004;145(3):216-225.

29. Arias JL, Neira-Carrillo A, Arias JI, Escobar C, Bodero M, David M, et al. Sulfated polymers in biological mineralization: a plausible source for bio-inspired engineering. *Journal of Materials Chemistry* 2004;14(14):2154-2160.

30. Goldberg WM. Acid polysaccharides in the skeletal matrix and calicoblastic epithelium of the stony coral Mycetophyllia reesi. *Tissue & Cell* 2001;33(4):376-387.

31. Aizenberg J, Lambert G, Weiner S, Addadi L. Factors involved in the formation of amorphous and crystalline calcium carbonate: A study of an ascidian skeleton. *Journal of the American Chemical Society* 2002;124(1):32-39.

32. Rieger, J.; Frechen, T.; Cox, G.; Heckmann, W.; Schmidt, C.; Thieme, J., Precursor structures in the crystallization/precipitation processes of CaCO3 and control of particle formation by polyelectrolytes. *Farad*ay *Discuss.* 2007**,** 136, 265-277.

33. Pichon, B. P.; Bomans, P. H. H.; Frederik, P. M.; Sommerdijk, N. A quasi-time-resolved CryoTEM study of the nucleation of CaCO3 under langmuir monolayers. *Journal of the American Chemical Society* 2008**,** 130, 4034-4040.

34. Li M, Mann S. Emergent nanostructures: Water-induced mesoscale transformation of surfactant-stabilized amorphous calcium carbonate nanoparticles in reverse microemulsions. *Advanced Functional Materials* 2002;12(11-12):773-779.

35. Brinker CJS, G. W. , editor. Sol-Gel Science: The Physics and Chemistry of Sol-Gel Processing (Academic, London). 1990.

36. Phillips BL, Casey WH, Karlsson M. Bonding and reactivity at oxide mineral surfaces from model aqueous complexes. *Nature* 2000 Mar;404(6776):379-382.

37. Casey WH, Swaddle TW. Why small? The use of small inorganic clusters to understand mineral surface and dissolution reactions in geochemistry. *Reviews of Geophysics* 2003; 41(2):1-20

38. Navrotsky A. Energetic clues to pathways to biomineralization: Precursors, clusters, and nanoparticles. *Proceedings of the National Academy of Sciences of the United States of America* 2004;101(33):12096-12101.

CHAPTER 4

ON THE ORIGIN OF AMORPHOUS CORES IN ACID POLYSACCHARIDE-MEDIATED BIOMIMETIC CALCIUM CARBONATE SPHERULITES: NEW INSIGHTS INTO SPHERULITIC CRYSTALLIZATION

*Chao Zhong,[†] and C. Chang Chu[†, ‡, *]*

Fiber and Polymer Science Program, Department of Fiber science and Apparel design, Cornell University, Ithaca, New York 14853-4401

Department of Materials Science and Engineering, Cornell University, Ithaca, New York 14853

Email: cc62@cornell.edu*

* To whom correspondence should be addressed. Phone: (607) 255-1938, Fax: (607) 255-1093.

† Department of Fiber science

§ Department of Materials Science

4.1 Abstract

Spherulitic crystals are found in many materials, including biominerals, but the overall process that creates them itself is not well understood. Using maleic chitosan as an organic template to control $CaCO_3$ crystallization, we have discovered a two-step process that leads to the formation of biomimetic $CaCO_3$ spherulites. In the first step, films of amorphous calcium carbonate (ACC) are formed, and amorphous nanoparticles are precipitated, deposited, and stabilized by maleic chitosan to form an ACC core. In the second step, this core acts as a nucleus to initiate radial growth of needle-like calcite subunits. The resulting crystals comprise an outer layer of needle-like crystalline $CaCO_3$ (calcite) and a core of ACC, thereby combining features of two kinds of $CaCO_3$ biominerals: the coexistence of calcite and ACC found in composite skeletal elements, and the radially-ordered structure of spherulitic biominerals. These findings suggest that amorphous cores might be more common in spherulites than has been generally recognized and, in conjunction with previous studies of spherulites in plants and animals, may provide new insights into the formation of spherulitic biominerals found in Nature. The findings may also have important implications for the understanding and eventual treatment of diseases in which amorphous cores have been already been observed, such as Alzheimer's disease and kidney stones.

Keywords Spherulitic crystallization, Spherulite, Amorphous Calcium Carbonate, Biomimetic Materials Synthesis and Biomineralization

4.2 Introduction

Spherulitic crystals are found in many materials including synthetic polymer melts [1], natural polymers [2], inorganics [3] and even metals [4]. They are also found in association with several human diseases including Alzheimer's disease [5] and kidney stones [6]. The crystals (displaying "Maltese-cross" extinction pattern under cross-polarized optical microscopy, called "spherulites") are polycrystalline aggregates that form from rapidly crystallizing solutions or from viscous gels or melts. The experimental study of nucleation is very challenging [7], and the rapid, spontaneous (due to high-force driven) crystallization of spherulites makes their nucleation particularly difficult to study. Despite more than a century of research and the existence of theories that describe the gross features of spherulitic growth [8, 9],very little is known about its early stages.

In the field of biomineralization, spherulitic crystals are often referred to as "spherulitic biominerals" [10], a unique type of radial growing polycrystalline minerals that arises from matrix-mediated processes of site-directed nucleation [11, 12]. Examples include scleractinian (stony) corals, avian eggshells, and fish otoliths [13-20]. Here too, the formation of the spherulitic biominerals is not well understood and remains a topic of debate. For example, geologists and biologists disagree about the growth of coral fibers: Is it a pure physico−chemical process, as suggested by the resemblance between crystals in coral and crystals in inorganics, or is it a biologically driven process, as suggested by the incorporation of organic macromolecules inside coral skeletons [16, 15]?

In the study reported here, we used $CaCO_3$ crystallization as a model system for studying the formation of spherulites. The significance of $CaCO_3$ crystallization is well known in both biomineralization and geosciences [21], and it has also been employed as a model for understanding nucleation and crystallization in both classical

[22] and non-classical crystallization [23]. In particular, we investigated the structural evolution of acid polysaccharide-mediated biomimetic $CaCO_3$ spherulites, paying particular attention to the early stages of crystallization. As described in detail below, our findings reveal a two-step process involved in spherulitic crystallization.

Our research strategy has also been motivated by the keen interest in synthesizing biomimetic materials. Biomimetic synthesis of $CaCO_3$ minerals in the presence of organic macromolecules is one of the promising bio-inspired pathways toward this goal [24], and we chose the synthetic acid polysaccharide maleic chitosan (Scheme 4.1), as an organic template for producing biomimetic $CaCO_3$ minerals. Despite increasing evidence of their widespread occurrence in biominerals, polysaccharides have received very little attention in either biomineralization or in the synthesis of biomimetic materials. The decision to use maleic chitosan in particular was based on two observations: polysaccharide chitin is found in nature as a major component of the organic fraction of several biocomposites [25] and acid polysaccharides rich in either carboxyl groups or sulfate groups are employed by organisms to regulate the growth and morphology of the corresponding biominerals [26-30].

Scheme 4.1. Chemical Structure of Maleic Chitosan

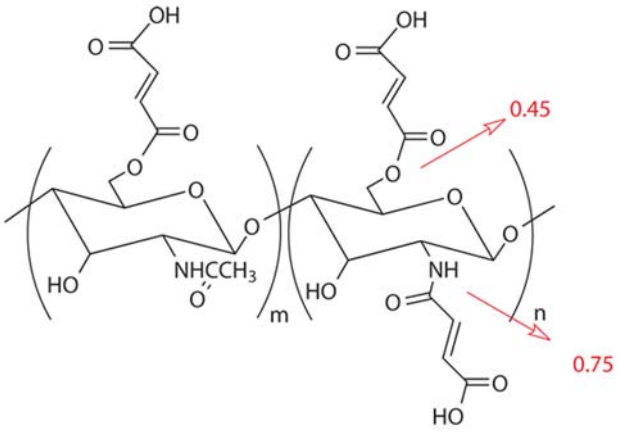

4.3 Experimental Section

4.3.1 Synthesis of maleic chitosan

The synthesis of maleic chitosan was carried out using a novel approach developed in our group. The starting material, chitosan (Sigma product) has 75% degree of deacetylation, with Brookfield viscosity 20.0-200cps (1% acetic acid). Briefly, 1.0 g methanesulfonic chitosan salts were dissolved in 100mL DMSO solvent under stirring at room temperature. Solid maleic anhydride of 6-fold in molar ratio was then added to the solution, and the reaction mixture was stirred under N_2 at 60 ^oC for 24 hrs. The resulting product in the solution was precipitated out by acetone, filtered, washed with copious amounts of acetone, and dried. Methanesulfonic (or tolunesulfonic) anions in the product were then removed from the chitosan salts by adding 0.1M $NaHCO_3$ solution. Finally the solution was dialyzed against deionized water (MW cut off 12,000) and lyophilized to yield 69% of the products. Degree of Substitution of Maleic chitosan=1.2, with N-2 and O-6 substitution 0.75 and 0.45, respectively. Molecular weight (M_n) =56,000.

4.3.2 Crystallization experiments

All chemicals are of analytical grade and used as received from sigma. All small pieces of glass cover slips was cleaned and sonicated in ethanol, rinsed with double distilled water, and finally dried with a constant flow of N_2. The mineralization of $CaCO_3$ was carried out in small Petri dish (5 mL), which were put in a closed desiccator at room temperature (22°C). In a typical procedure, 75 μL 10 mg/mL maleic chitosan solution was injected into 3 mL of 50mM $CaCl_2$ solution and the homogeneously mixed solution was then transferred into a Petri dish. Then, one piece of glass slide was carefully put into the Petri dish for collecting the crystals. After that, the bottles were covered with Parafilm, which was punched with three needle holes, and placed in a larger desiccator. Three small glass bottles (15mL) of crushed

ammonium carbonate were also covered with Parafilm punched with one needle holes in the center and placed at the bottom of the desiccator. Samples were collected from the dishes at different time intervals within 24 hours. The samples were washed with distilled water and dried in air for further characterization. Control crystallizations (with only 50mM $CaCl_2$) were also carried out in the desiccator containing ammonium carbonate. Typical rhombohedral calcite crystals were always obtained in the absence of maleic chitosan.

4.3.3 Etching experiments

The crystals collected at 24 hours were used for etching experiments. To facilitate the differentiation of crystalline phase from amorphous phase that possibly exists inside the spherulites, we prepared our samples with the spherulites' basal plane (or nucleation plane) completely disclosed using a special method. Specifically, the crystals were carefully peeled off the glass slide using regular tape. Some crystals were successfully transferred from the glass slides and became embedded in the tape surface. Samples thus prepared were then either etched in deionized (DI) water, or 1 M KOH for 12 and 6 hours, respectively. After etching treatments, they were briefly washed with DI water and dried, and the etch figures on the cross sections were then observed by SEM.

4.3.4 Special experiments for studying nucleation events

The evolution of amorphous film into a spherulite structure is quite rapid, taking only about 15 minutes (45min and 1 hour sample in Figure 4.7). This makes it difficult to examine any intermediate processes under normal crystallization conditions. Accordingly, we adopted the alternative of removing the crystallization dish from the desiccators after 45mins, but collecting samples from the dish for observation at ten minutes intervals. In this way, we expect that the consequent crystallization events would be slowed down so that we can investigate the

relationship between 45min and 1 hour sample.

The major procedures for the specially-designed experiment are shown in Scheme 4.2: After 45 mins crystallization, petri dishes were removed from the closed desiccator. The samples growing on glass slide are collected at 10mins intervals, with aging time in solution ranging from 0 min to 20mins. During the aging periods, the petri dishes were still sealed and the samples inside the petri dishes were visualized to float on the crystallization solution.

Scheme 4.2. Procedures of the specially-designed experiments for study of nucleation events

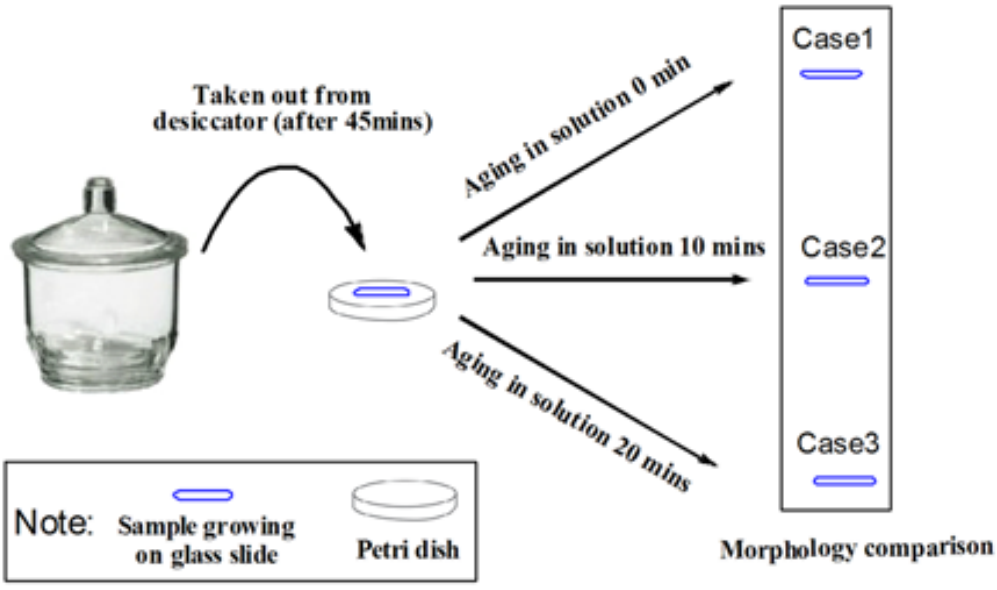

4.3.5 Characterization

FTIR:

Sample collected at certain time was carefully scraped off from the glass slides, and then the ground sample was dispersed in KBr pellets. FTIR spectra were then obtained with a Perkin-Elmer (Madison, WI) Nicolet Magana 560 spectrometer from KBr pellets.

Powder X-ray diffraction (pXRD):

Crystals grown on glass slides in solution were studied Using a diffractometer (Scintag, Inc., Cupertino, CA) with Cu Kα radiation (wavelength =1.5405 Å).

SEM:

The morphology of the obtained samples was examined by scanning electron microscopy **(**KECK FE-SEM, LEO 1550 (Schottky Field Emitter) after being sputter-coated with Au/Pd. The experiments were performed at low accelerating voltages (3 KeV), especially suitable for imaging the surface detail of low-density materials.

POM (Polarized Optical Microscope):

Fresh Samples formed on glass slides were directly observed using a polarized optical microscope (Zeiss) equipped with cross-polarizers in the transmission mode. Many of these optical micrographs are taken using the first-order red λ-plate so that both birefringent and isotropic material can be viewed in cross-polarized light.

TEM:

45min Samples were directly formed on TEM carbon grids, and then loaded using a single tilt holder into TEM facility for structure characterization. TEM was performed on a FEI Technai T12 at 120 kV, and electron diffraction was correspondingly recorded using the same equipment.

TGA:

Air-dried 4-hour samples were used for TGA test by using a thermogravimetric analyzer (TGA), model 2050, (TA Instruments, New Castle, DE). Air-dried samples were directly scraped off from the glass slides and used immediately for the TGA test. All specimens were scanned from 25 °C to 500 °C at a ramp rate of 20 °C/min. All TGA tests were carried out in nitrogen environment. Typical TGA curve was shown below.

4.4 Results and Discussions

Using the ammonium carbonate diffusion method, $CaCO_3$ crystallization was carried out in the presence of maleic chitosan and observed at different time intervals ranging from 30 minutes to 24 hours. The analysis of the 4-hour sample by scanning electron microscopy (SEM) revealed a uniform spherulite shape composed of needle-like subunits with many (104) faces exposed, a typical characteristic of calcite morphology (Figure 4.1a and 4.1c). The spherulitic feature is further confirmed by cross-polarized optical microscopy, under which all aggregates exhibit a "Maltese-cross" extinction pattern typical of spherulites (Figure 4.1b). Powder XRD (Figure 4.2) and FTIR spectrum (Figure 4.3) all appear to support that the spherulites are composed only of calcite.

To investigate the interior structure of the crystals, we etched the crystals in deionized (DI) water. After etching for 4 days, the spherulites show a very interesting dissolution pattern, with the remaining needle-like subunits stretching radially outwards from an open 3-5 μm diameter center area (Figure 4.1d). Similar dissolution was observed for the 1-hour samples after etching in DI water for 20 hours (Figure 4.4). Because no crystalline phases other than calcite were detected in the X-ray diffraction pattern, the preferential dissolution in the center region could be attributed to amorphous phase, which doesn't diffract X-ray and has a much higher solubility than calcite phase. At this point, however, we cannot rule out the possibility that relatively a higher concentration of macromolecules together with calcite phase is present in the center.

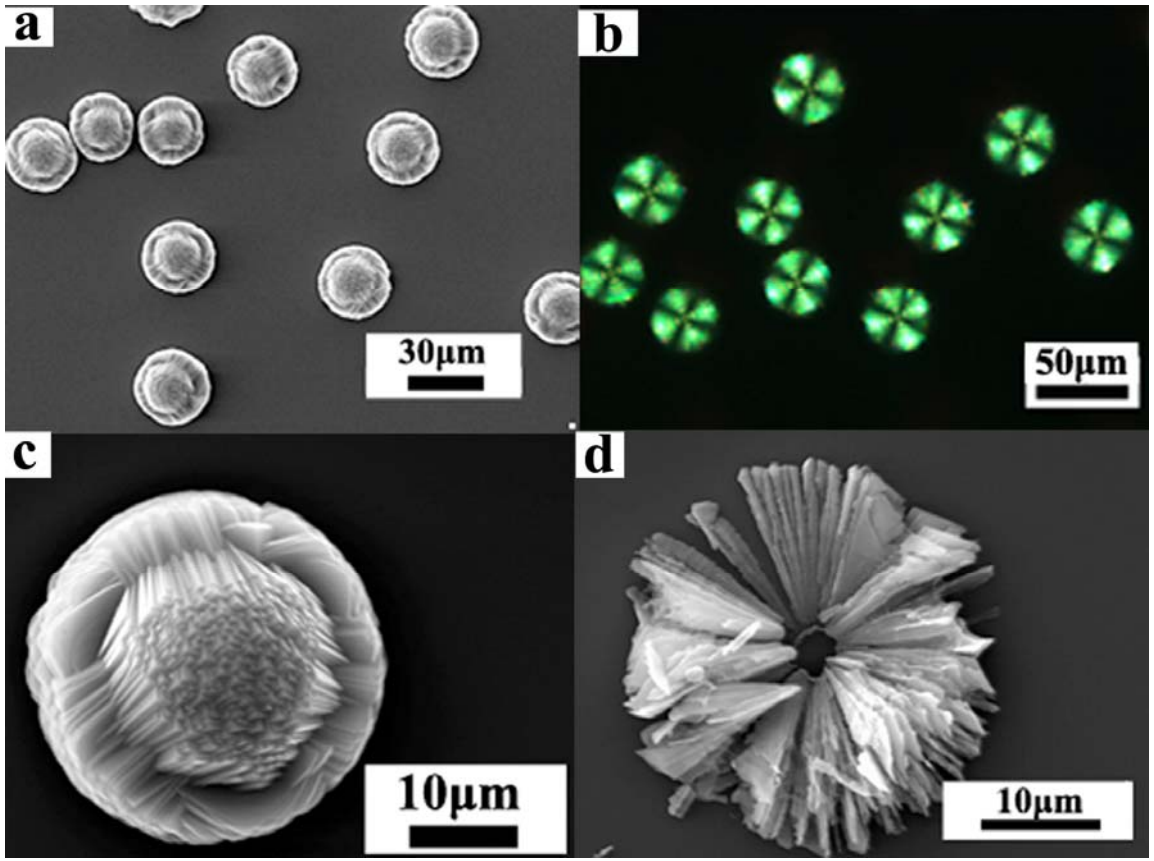

Figure 4.1.(a, c) SEM images of as-prepared spherulites after 4-hour crystallization; (b) Crossed-polarized Optical Microscopy Image of as-prepared spherulites after 4-hour crystallization; (d) SEM image of 4-hour sample after etching in DI water for 4 days.

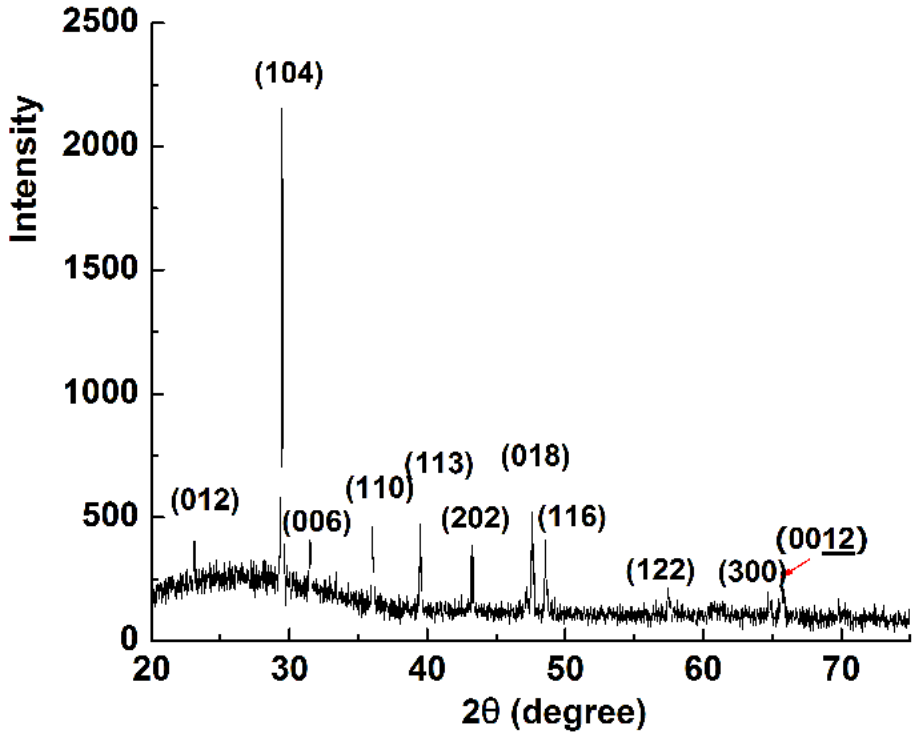

Figure 4.2. WAXS (wide angle X-ray scattering) plots from calcium carbonate crystals after 4 hours. The XRD pattern of the sample displays the following diffraction peaks (2θ): 23.10, 29.47, 31.51, 36.01, 39.40, 43.21, 47.59, 48.50, 57.51, 61.30, 64.71, 65.66, which can be correlated to the (hkl) indices (012), (104), (006), (110), (113), (202), (018), (116), (122),(119), (300), (0012), respectively, of pure calcite . These results are in agreement with the SEM observations.

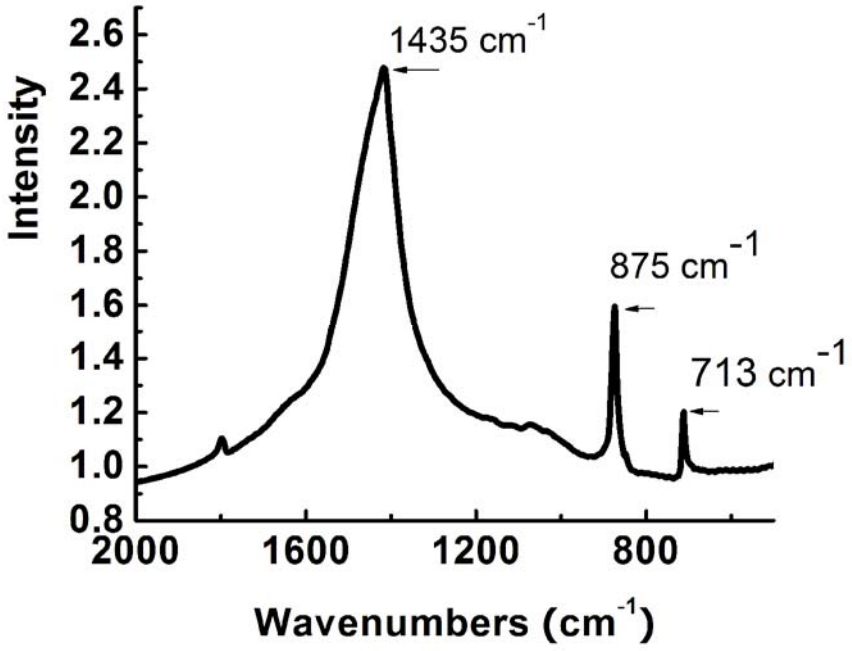

Figure 4.3. FTIR spectrum of 4-hour sample shows only the characteristic calcite reflections. The FTIR spectrum displays only the characteristic v_4, v_2, and v_3 absorption bands of calcite at 713, 875, and around 1435 cm^{-1}, respectively.

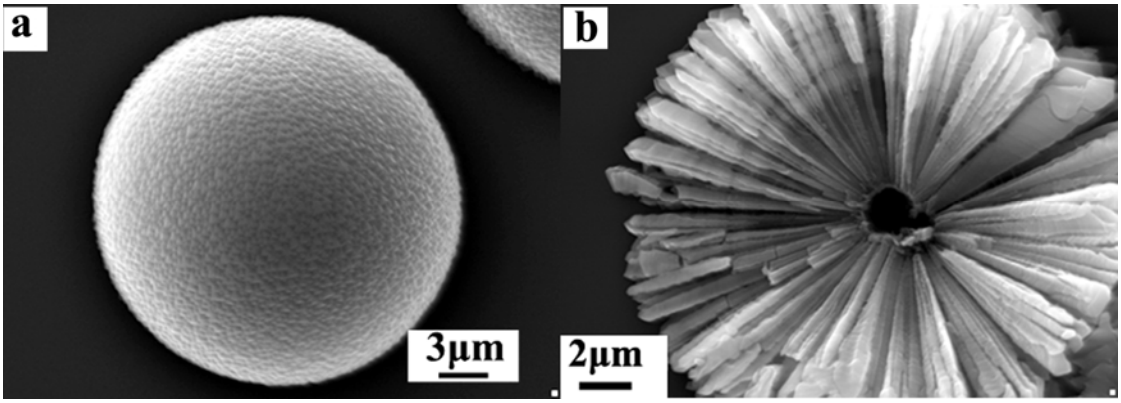

Figure 4.4. SEM Micrographs of 1 hour Spherulites (obtained in the presence of Maleic Chitosan after 1 hour crystallization.) (a) as-prepared sample; (b) sample etched in DI water for 20 hours.

To further clarify the phase in the center of the spherulites, we selected 24-hour samples and investigated their basal surfaces(or nucleation surfaces) by carefully peeling them off the glass slide using regular tape and then etching them in both DI water and KOH solution (Figure 4.5a). Etching experiments have proven useful in the past for differentiating an ACC phase from a crystalline phase due to their different solubility [32]. In particular, treatments with KOH solution have been reported to selectively dissolve the ACC phase without affecting the pure calcite phase [33].

As is shown in Figure 4.5b and 4.5c, the bottom surface of unetched spherulites always displays radial subunits covered by a very thin film in the center area. After being etched in double distilled water for 12 hours, the thin film covering the needles is gone, a 'hole' surrounded by radial growing needle-like subunits is clearly visible instead (Figure 4.5d, e and g). Clearly the center part of the basal surface is more easily—and thus more heavily—corroded than the outer part. The higher resolution image reveals the presence of 50~200nm nanoparticles in the hole, a typical morphology of the ACC phase (Figure 4.5f).

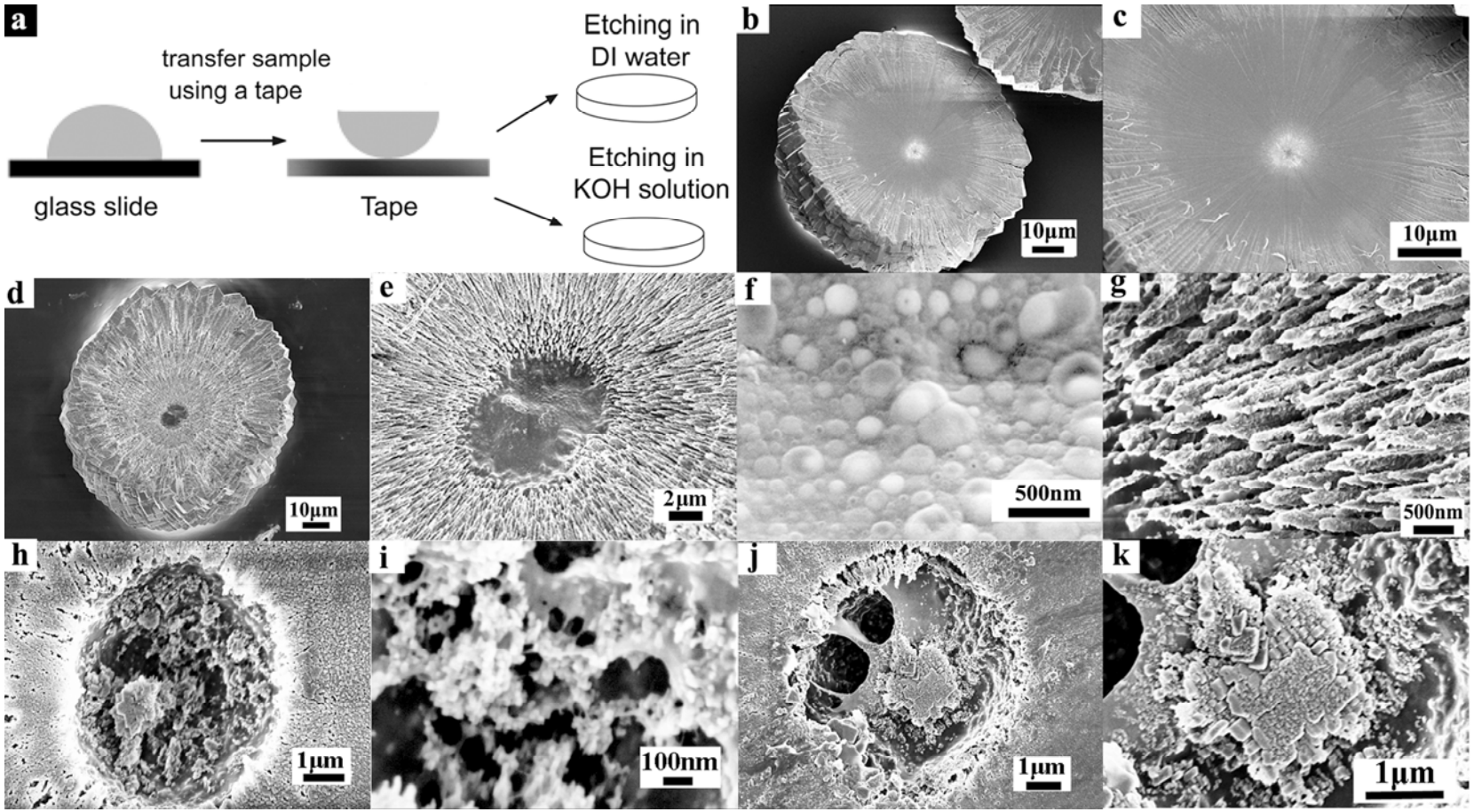

Figure 4.5. Scheme showing etching experiments (a) and SEM micrographs of 24-hour spherulites before (b-c) and after etching experiments (d-k): (d-g) after etching in DI water for 12 hours; (h-i) after etching in 1M KOH solution for 6 hours; (j-k) after etching in 1M KOH solution for 6 hours, followed by heating in one drop of water.

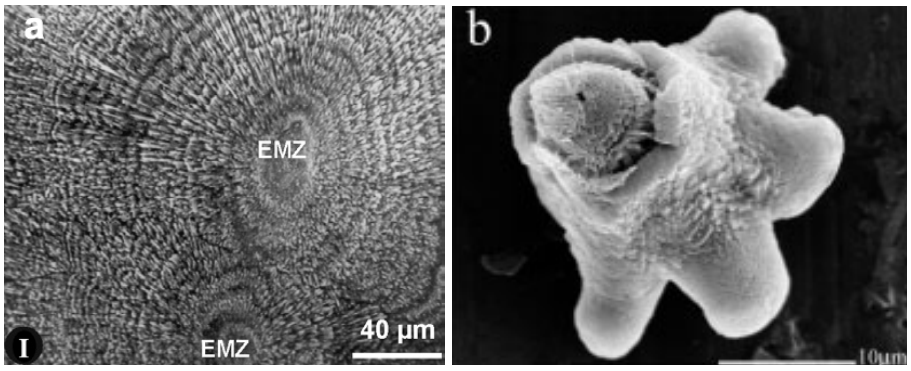

Figure 4.6. SEM images of a) stony coral showing spherulitic arrays of aragonite radiating out from the nucleation center; b) etched tunic dogbone spicule, showing an external calcite layer separated by a membrane from an internal ACC core (a,b, reproduced from reference 31, 32, respectively).

Figure 4.5h shows the results of etching in 1M KOH for 6 hours. A structural boundary around the center area is clearly visible. The affected area is approximately 5µm in diameter, similar to the size of center open area in the 4 hour spherulite superstructures after etching in distilled water for 4 days (Figure 4.1d). The enlarged image of the affected area indicates that both ACC nanoparticles and organic materials are present (Figure 4.5i). When the etched sample was heated in a small drop of water (0.1 mL), the nanoparticles aggregated and recrystallized into calcite phase with typical rhombohedral morphology (Figure 4.5j and k). On the basis of the above observations, we conclude that each spherulite contains two phases, an inner core of polysaccharide-stabilized ACC phase with diameter around 5µm, and an outer layer of calcite phase. Interestingly, the spherulites with such unusual architectures possess combined features from two independent types of $CaCO_3$ biominerals: radially-ordered structure of spherulitic biominerals (e.g., stony corals (Figure 4.6a) and the coexistence of crystalline $CaCO_3$ (Calcite) and stable amorphous calcium carbonate (ACC) of the composite skeletal elements (e.g., Dogbone spicule from tunic (Figure 4.6b) [31-34].

Time-dependent study indicates the spherulites start to appear after 1 hour crystallization (Figure 4.7). Their average size increases from 17μm at 1 hour to 54μm at 24 hours (Figure 4.8a), implying that the ACC weight percentage, defined as (W_{ACC}/ $W_{(ACC + Calcite)}$), should decrease as a result of more calcite phase forming at the outer layers as the crystallization process progresses, as illustrated in Figure 4.8b. This is confirmed by the infrared spectra of the crystals collected at different times (Figure 4.8c). It has been previously reported that the ratio of the maximum intensity of the v_2 mode at 875 cm^{-1} and the v_4 mode at 713 cm^{-1} ($I_{max}v_2$/ $I_{max}v_4$) is proportional to the ACC percentage in Paracentrotus lividus [35] and S. purpuratus sea urchin larval spicules [36], both of which are considered mixtures of ACC and calcite phase. As seen in Figure 4.8c, our results show a decreasing trend from 4.68 to 3.11 in this same intensity ratio in our own samples as crystallization progresses. Noticeably, the broad v_1 absorption band of ACC around 1070 cm^{-1} is clearly present in the spectrum of the 1-hour sample as a result of relatively higher ACC proportion, and this broad FTIR band became gradually smaller with time and disappeared almost completely at 24 hrs sample.

To probe the origin of amorphous cores in these spherulites, we collected early-stage products (30-45 minute samples), points at which they always display film-like morphology. Figure 4.9a, b and 4.7 show the typical morphology of 45 min films; and, as TEM image (Figure 4.9c) shows, they are constructed from many smaller nanoparticles and their formation can be explained using a colloidal nanoparticle self-organization mechanism as described in our previous publication [37]. We have shown above, in Figures 4.5b and c, that the basal surface of each unetched spherulite always has a thin film in the center covering the radial subunits. It thus seemed possible that the formation of spherulites begin with those thin amorphous films.

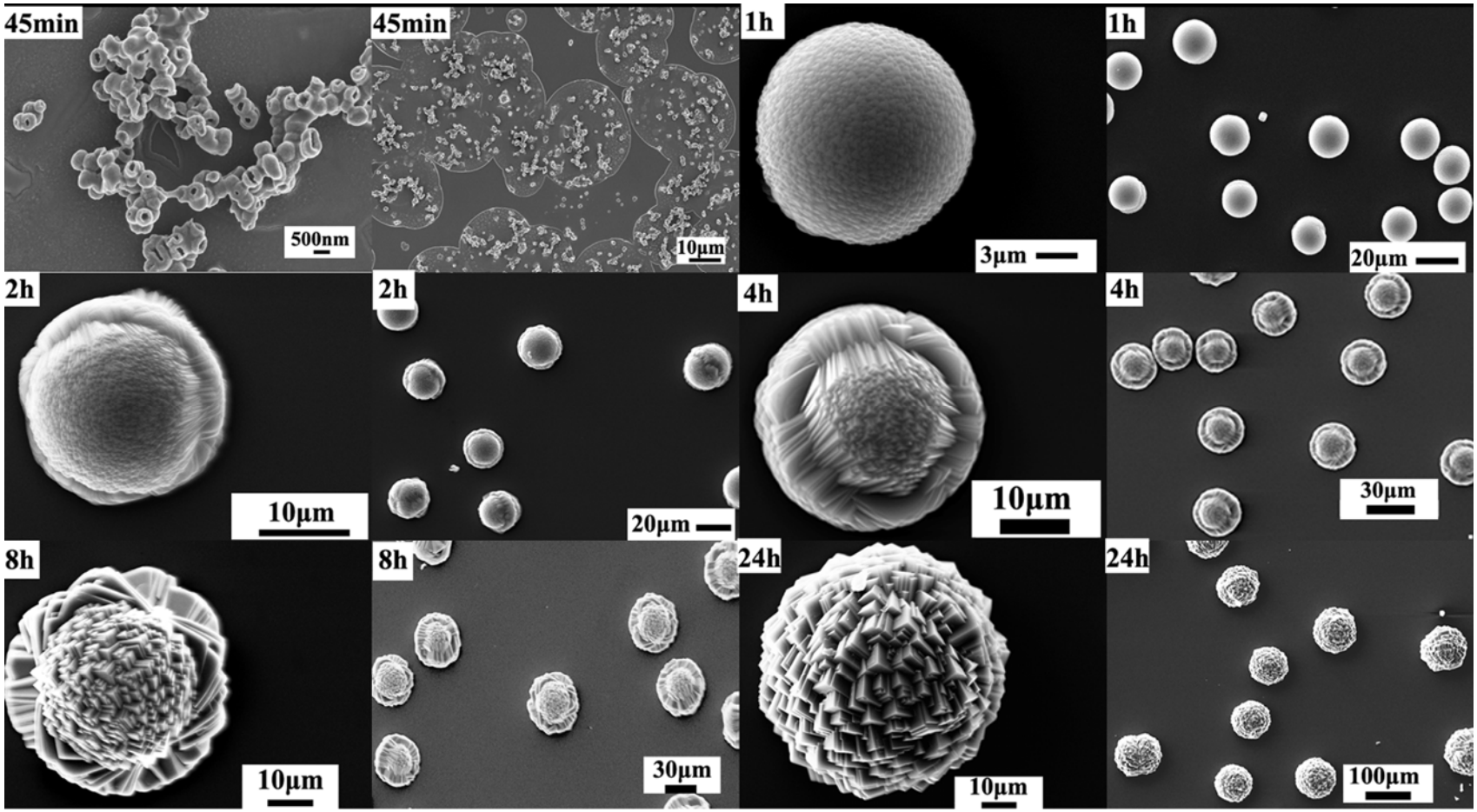

Figure 4.7. SEM images of samples collected at different time intervals ranging from 45mins to 24 hours.

Figure 4.8. (a) Effect of crystallization time on the size of spherulites collected at different time intervals within 24 hours; (b) scheme showing that ACC is located in the core, while more calcite phase forming at the outer layers as crystallization process progresses; ACC weight percentage (defined in a) thus decreases as a function of time. (c) The corresponding FTIR spectra for samples collected at different time intervals within 24 hours.

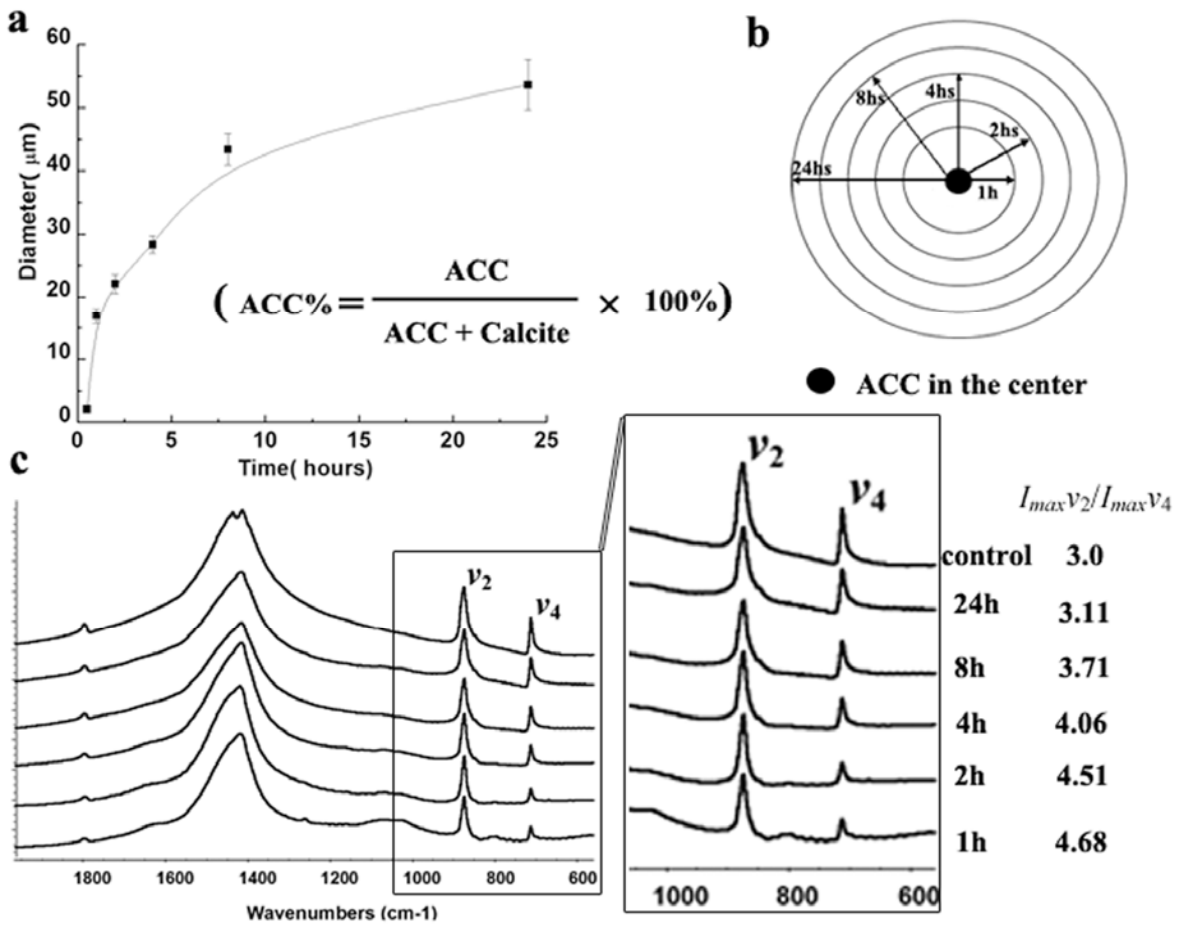
a
Diameter(μm)
Time(hours)
$\left(\text{ACC\%} = \frac{\text{ACC}}{\text{ACC + Calcite}} \times 100\% \right)$
b
8hs
4hs
2hs
24hs
1h
ACC in the center
c
v_2
v_4
Wavenumbers (cm-1)
$I_{max}v_2/I_{max}v_4$
control 3.0
24h 3.11
8h 3.71
4h 4.06
2h 4.51
1h 4.68

To explore this possibility further, we investigated the relationship between the amorphous film and the spherulites as a function of time. The evolution of amorphous film into a spherulite structure is quite rapid, taking only about 15 minutes (45min and 1 hour sample in Figure 4.7). This makes it difficult to examine any intermediate processes under normal crystallization conditions. Accordingly, we adopted the alternative of removing the crystallization dish from the desiccators after 45mins, but collecting samples from the dish for observation at ten minutes intervals. (Scheme 4.2, experimental section).

The results are shown in Figure 4.9. The films show amorphous features at all time intervals, as indicated by corresponding SAED (Figure 4.9c insert) and cross-polarized optical micrograph (Figure 4.9f and 4.9I insert), but the detailed surface morphology of the film changes over time. Initially, many donut-like nanoparticles around 200~300nm are randomly distributed on ACC films (Figure 4.9a, b). After 10 mins in crystallization solution, each film shows two well-defined regions: a smooth denser outer domain and a rough loose center domain, with a micron-sized particle located at the center (Figure 4.9d, e). Such unusual morphology may suggest the existence of multiple forms of ACC with different degrees of hydration and short range order. The occurrence of ACC nanoparticles in the center implies the onset of building up of a nucleus for subsequent crystallization. After another 10mins in solution, the film shows flower-like morphology probably due to a further dehydration effect of ACC phase, while more nanoparticles are glued by fibrous-like organic material, maleic chitosan, in the core (Figure 4.9h insert). Interestingly, the location and morphology of these aggregated donut-like particles are very similar to those of the remaining nanoparticules we observed inside the center hole of the etching samples (Figure 4.5f). Our observations thus confirm that spherulite formation is intimately associated with the initial formation of an amorphous film.

Figure 4.9. (a-b, d-e and g-h) SEM images of 45-min samples collected after aging in solution for different times: (a-b) 0 min, collected immediately; (d-e) 10 minutes; (g-h) 20 minutes; (c) Bright-field TEM image of 45-min samples collected immediately. The inserted image is the SAED pattern of the samples shown in c; (f-i) polarized optical micrographs of 45-min samples collected after aging in solution for different time: (f) 10 minutes, i) 20 minutes. *Note: the inserted Cross-polarized optical images in f, i were observed with the first-order red λ-plate inserted. In both cases, the films were seen as same color as the background when using the first-order red λ-plate with cross-polarizer, indicating isotropic features.*

a
10μm
b
1μm
10μm
c
100nm
d
10μm
e
5μm
f
20μm
g
10μm
h
5μm
i
20μm

Accordingly, we propose that a two-step crystallization process explains the formation of spherulites. As illustrated in Figure 4.10, a two-dimensional transformation is followed by a three-dimensional transformation. In the first step, maleic chitosan-induced ACC nanoparticles aggregate and self-organize into amorphous films at an early stage. The rough films then evolve into films with two well-defined domains, an outer and a center domain. Such films then serve as a substrate for a subsequent three-dimensional (3D) transformation. In this step, ACC nanoparticles are continuously deposited onto the center of the film to form an ACC core with diameter of 3-5μm. This ACC core then acts as nucleus for building up the radial growing needle-like subunits.

The calcite subunits can be considered to grow at the expense of the metastable ACC phase that initially formed from the parent solution phase, even though at this stage we do not know the specific mechanism regarding the growth of subunits (for example: via a dissolution-recrystallization pathway or an ACC precursors pathway). We further assume that calcite subunits nucleate and grow (in a 3D mode) at rates $J_{calcite}$ and $G_{calcite}$ in a metastable ACC phase whose rates of nucleation and growth (in a 2D mode) in the old solution phase are J_{acc} and G_{acc}. In addition, ideally, the overall crystallization process follows the classical Kolmogorov-Johnson, Mehl-Avrami (KJMA) kinetics involving stationary nucleation and power-law growth of particles. Under these conditions, the kinetics of the overall crystallization process can be theoretically described using the following formulas originally proposed by Kashchiev and Sato [38].

$$\alpha_{acc}(t) = V_{acc}(t)/V_0 = 1 - \exp\left[-(t/\theta_{acc})^m\right] \quad (1)$$

$$\alpha_{calcite}(t) = V_{calcite}(t)/V_0 = \alpha_{acc}(t) - \int \exp\left\{-\left[(t - t')/\theta_{calcite}\right]^s\right\}\left[d\alpha_{acc}(t')/dt'\right] dt' \quad (2)$$

Figure 4.10. A proposed two-step crystallization mechanism for the formation of acid polysaccharide-mediated $CaCO_3$ spherulites. **Step 1 2D transformation mode:** 1) Maleic chitosan macromolecules sequester and concentrate the Ca^{2+} ions (red dots), phase separation might take place. 2) Metastable colloidal ACC nanoparticles precipitate as a result of increasing local supersaturation. 3) ACC films form via a colloidal nanoparticle self-organization mechanism, 4) the randomly-aggregated ACC films evolve into well-organized ACC films composed of two well-defined regions (core and outer) possibly due to a dehydration effect. **Step 2 3D transformation mode:** 5) ACC nanoparticles are deposited onto the core area, 6) more nanoparticles are deposited and stabilized in the center by maleic chitosan, 7) needle-like calcite subunits grow from the ACC core in a radial growing mode.

Two-step Crystallization Mechanism

Step1 2D transformation mode (Top view)

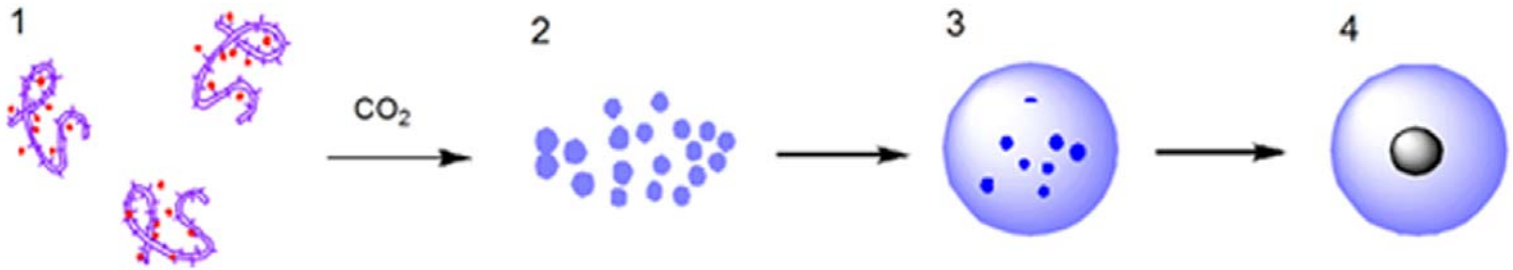

Step2 3D transformation mode (Side view)

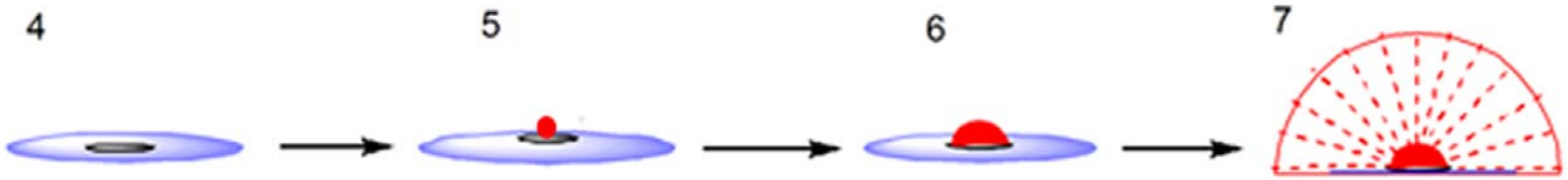

Where, α_{acc} and $\alpha_{calcite,}$ are defined respectively as volume fractions of the metastable ACC and calcite at time t, θ_{acc} and $\theta_{calcite}$ are time constant of the formation of ACC and Calcite, and m, s are the kinetic exponent characterizing the ACC and calcite.

As $\theta_{acc}= (m/C_{acc} J_{acc} G_{acc}^{m-1})^{1/m}$, and ACC films grow in a 2-dimensional growth mode (m=3, $C_{acc}= \pi H_0$, (H_0 , constant film thickness)), accordingly, $\theta_{acc}= (3/\pi H_0 J_{acc} G_{acc}^{2})^{1/3}$.

Similarly, as $\theta_{calcite} = (s/C_{calcite} J_{calcite} G_{calcite}^{s-1})^{1/s}$, and calcite subunits grow in a 3-dimensional growth mode (spheres) (s=4, $C_{calcite}=4\pi/3$), accordingly, $\theta_{calcite} = (3/\pi J_{calcite} G_{calcite}^{3})^{1/4}$.

For $t/\theta_{acc} \geq b$ ($t/\theta_{acc} < b$, $\alpha_{calcite}(t)=0$), approximately, equation (b) becomes:

$$\alpha_{calcite}(t) = \alpha_{acc}(t) (1- \exp\{-(\theta_{acc}/\theta_{calcite})^{s} [(t/\theta_{acc})-b]^{s}\}), \quad b= (m-1/m)^{1/m} \qquad (3)$$

The equation (2) tells us that $\alpha_{calcite}$ depends not only on the kinetics of appearance of the stable phase itself, but also on the rate of formation of the metastable phase. Further, equation (3) indicates that the ratio $\theta_{acc}/\theta_{calcite}$ is the main parameter to control the appearance of the stable crystalline phase.

The general condition for formation of a long-living metastable ACC phase because of a delayed appearance of the calcite phase in it is:

$$(\ln 2)^{(1/s-1/m)} \theta_{calcite}/\theta_{acc} > 1,$$

With the concrete values listed above, this inequality becomes:

$$(\ln 2)^{-1/12} (3/\pi J_{calcite} G_{calcite}^{3})^{1/4}/(3/\pi H_0 J_{acc} G_{acc}^{2})^{1/3} > 1 \qquad (4)$$

This expression shows explicitly that the faster kinetics of nucleation and growth of the ACC phase (for example, J_{acc} and/or G_{acc} sufficiently larger than $J_{calcite}$ and/or $G_{calcite}$, respectively) is the reason for delayed two-step crystallization of or in the parent phase.

Our proposed crystallization mechanism is very similar to a so-called

"stepwise crystallization" or "two-step nucleation," a mechanism that has been proposed for protein crystallization through numerical simulations [39] and directly observed in colloidal model crystallization system [40]. According to the stepwise crystallization, crystal nucleation begins with the formation of metastable phase. Metastable phase is usually not stable, the thermodynamic accomplishment of the overall crystallization process thus required further transformation of the metastable phase into the stable crystalline phase.

Both the stepwise crystallization and our proposed two-step crystallization are consistent with the predication of Ostwald's rule of stages. However, the crystallization process in our system is more complicated, containing unique crystallization features. For example, multiple forms of metastable ACC (films versus cores) with different degree of hydration and short range order might exist in our system. In addition, amorphous cores initially appear at the center of amorphous films as nucleus, and remain as amorphous phase even after the formation of spherulites.

Previous studies suggest that macromolecules might be one of the factors that can stabilize biogenic ACCs in certain biominerals [41]. We believe that maleic chitosan also contributes to the stabilization of ACC phase. Indeed, organic phase associated with ACC nanoparticles was clearly visualized in the center of spherulites after etching (Figure 4.5i), and the incorporation of maleic chitosan into the spherulites was confirmed by TGA data (Figure 4.11).

Recent biomineralization research has revealed several important functions of ACC phase in biominerals and biomineralization process [41]. These include transient precursors for the two major crystalline polymorphs (calcite and aragonite), temporary storage deposits and structural elements for certain biominerals [41]. In particular, coexistence of stable ACC and crystalline phase in a microstructure has been previously observed in biogenic skeletal elements (e.g., sponge and ascidian spicules),

and investigators have speculated that ACC in the composite structures is constructed for structural purposes and may confer advantageous mechanical properties [34]. The coexistence of stable ACC and crystalline phase was also identified in our acid polysaccharide-mediated spherulitic structures. However, the primary function of the ACC core in our biomimetic spherulites appears to be to serve as the nucleus for the crystallization of the needle-like subunits, thereby initiating spherulitic crystallization. We therefore believe this role goes beyond the known functions of ACC in either the biogenic or synthetic forms. It may be that this new role also takes advantage of ACC's isotropic property which permits the needle-like subunits to grow outwards in all directions.

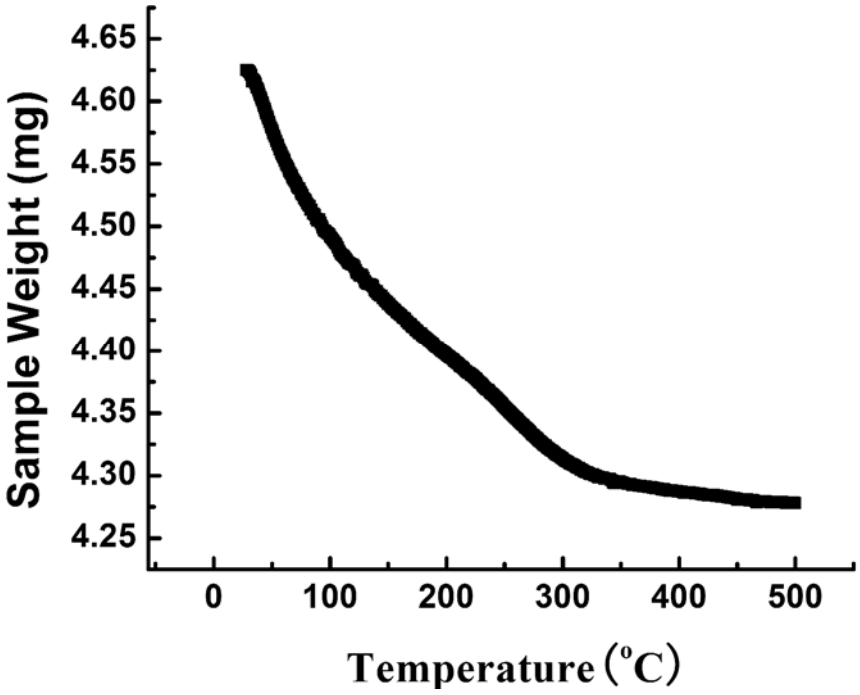

Figure 4.11. Thermogravimetric analysis (TGA) curves of 4-hour air-dried sample. The weight loss when heated to 500°C equals to 7.51%, indicative of the incorporation of small amount of Maleic chitosan inside the crystals.

Our findings may provide insights into the formation of spherulitic arrays in some $CaCO_3$ biominerals. $CaCO_3$ spherulite biominerals are produced in several natural mineralizing systems, including stony corals, avian eggshells, and fish otoliths. The mechanisms of these spherulitic biominerals formation are not fully understood. Previous observations have led to the belief that polycrystalline bundles grow from predisposed nucleation centers that are rich in either crystalline phase and/or organic materials [12]. This feature also appears in our in-vitro biomimetic spherulites in which radial growing needle-like calcite subunits grow off pre-formed nucleation centers. In our spherulites, the centers are rich in polysaccharide-stabilized ACC phase. Nevertheless, the components of nucleation centers in biogenic spherulites have not been confirmed in all cases. For example, some researchers have already cast doubt on the precise mineral phase at the trabecular centers of the corals and have suggested the possibility of an ACC precursor of the granular calcite seed nuclei [18, 42]. It would be informative to reexamine the possibility that ACC phase, either in transient or stable form, might be present at some point at the nucleation centers of spherulite $CaCO_3$ biominerals. It is relevant that the formation of avian egg shells and scleractinian coral skeletons are among the most rapid mineralization processes known [10]. ACC is likely to be precipitated as early stage products in such conditions, and ACC phase is either extremely difficult to detect in its transient form or easily overlooked when it coexists with crystalline phase [34, 43].

Similar observations can be applied not only to other types of biominerals, but to domains beyond the field of biomineralization. For example, central noncrystalline "cores" from which individual crystals radiate to form spherulites have been observed in druses of calcium oxalate crystals in plants [44] (crystalline mineral aggregates in plants, botanically termed "druses") and in human calcium oxalate monohydrate urinary (kidney) stones [6]. The simultaneous occurrence of regularly ordered and

disordered materials has also been observed in spherical amyloid deposits in Alzheimer's disease plaques [44] and in bovine insulin spherulites known as "amyloid-containing spherulite-like structures" [46-48]. The amorphous (nonbirefringent) core located at the heart of the insulin spherulites is thought to form through random aggregation and is likely to form the nucleus for spherulitic crystallization [46].

The simultaneous co-existence of amorphous and crystalline phases in these several cases makes it highly likely that many other types of spherulites may form similar structures using a similar two-step crystallization mechanism. After all, metastable amorphous phase is very likely to form in crystallization systems with high driving force, and the driving force for spherulitic crystallization (either from a solution or viscous gel or melts) is usually quite high. The formation of amorphous cores inside spherulites would also be favored by their being isotropic with no preferential orientation, and hence energetically more likely to induce the crystalline subunits to grow outwards in all directions. Because it is very easy to overlook small amounts of amorphous phase when it coexists with crystalline phase, we urge investigators to look carefully for this combination when studying spherulite structures.

4.5 Conclusions

Using a synthesis strategy inspired by biominerals, we have produced unusual $CaCO_3$ superstructures from a biomimetic mineralizing system in which maleic chitosan was used as an organic template to control calcium carbonate formation in an aqueous solution. The resulting calcite crystals possess features of two independent types of biominerals: the radially ordered structure of spherulitic biominerals and the coexistence of crystalline calcite and stable amorphous calcium carbonate (ACC) of the composite skeletal elements.

We have demonstrated that the crystallization begins with the formation of amorphous thin films, probably in transient ACC form. Amorphous nanoparticles are then deposited and stabilized by acid polysaccharide onto a pre-defined center area of the film to form a stable ACC core. This ACC core then acts as nucleus to initiate radial growth of needle-like calcite subunits, a role that goes beyond the known functions of ACC in both biogenic and synthetic forms. After approximately an hour, the spherulitic superstructures appear in which the ACC and calcite phase form at the core and outer layer, respectively. In short, we suggest that a 2-D transformation is followed by a 3-D transformation to produce the superstructures.

Finally, we believe that our findings may not only provide insights into the formation of spherulitic biominerals in nature, but they may also have important implications for the understanding and eventual treatment of diseases in which amorphous cores have already been observed, such as Alzheimer's disease and kidney stones.

4.6 Acknowledgement

This project was partially supported by graduate student thesis funds from the School of Human Ecology at Cornell University. This work made use of the electron microscopy (SEM and TEM) facilities of the Cornell Center for Materials Research (CCMR) with support from the National Science Foundation Materials Research Science and Engineering Centers (MRSEC) program (DMR 0520404).

REFERENCES

1. Magill, J. H., Review spherulites: A personal perspective. *Journal of Materials Science* 2001, 36, (13), 3143-3164.

2. Kobayashi, S.; Hobson, L. J.; Sakamoto, J.; Kimura, S.; Sugiyama, J.; Imai, T.; Itoh, T., Formation and structure of artificial cellulose spherulites via enzymatic polymerization. *Biomacromolecules* 2000, 1, (2), 168-173.

3. Browne, G. H.; Kingston, D. M., Early Diagenetic Spherulitic Siderites from Pennsylvanian Paleosols in the Boss Point Formation, Maritime Canada. *Sedimentology* 1993, 40, (3), 467-474.

4. Miao, B.; Wood, D. O. N.; Bian, W. M.; Fang, K. M.; Fan, M. H., Structure and Growth of Platelets in Graphite Spherulites in Cast-Iron. *Journal of Materials Science* 1994, 29, (1), 255-261.

5. Snow, A. D.; Sekiguchi, R.; Nochlin, D.; Fraser, P.; Kimata, K.; Mizutani, A.; Arai, M.; Schreier, W. A.; Morgan, D. G., An Important Role of Heparan-Sulfate Proteoglycan (Perlecan) in a Model System for the Deposition and Persistence of Fibrillar a-Alpha-Amyloid in Rat-Brain. *Neuron* 1994, 12, (1), 219-234.

6. Khan, S. R., Calcium phosphate calcium oxalate crystal association in urinary stones: Implications for heterogeneous nucleation of calcium oxalate. *Journal of Urology* 1997, 157, (1), 376-383.

7. Sear, R. P., Nucleation: theory and applications to protein solutions and colloidal suspensions. *Journal of Physics-Condensed Matter* 2007, 19, (3):33101-33129

8. Keith, H. D.; Padden, F. J., A Phenomenological Theory of Spherulitic Crystallization. *Journal of Applied Physics* 1963, 34, (8), 2409-2421.

9. Goldenfeld, N., Theory of Spherulitic Crystallization. *Journal of Crystal Growth* 1987, 84, (4), 601-608.

10. Addadi, L.; Weiner, S., Control and Design Principles in Biological Mineralization. *Angewandte Chemie-International Edition in English* 1992, 31, (2), 153-169.

11. Mann, S.; Webb, J.; Williams, R. J. P., *Biomineralization: Chemical and Biochemical Perspectives*. VCH Publishers: New York, 1989; p 541.

12. Weiner, S.; Addadi, L., Design strategies in mineralized biological materials. *Journal of Materials Chemistry* 1997, 7, (5), 689-702.

13. Nys, Y.; Gautron, J.; Garcia-Ruiz, J. M.; Hincke, M. T., Avian eggshell mineralization: biochemical and functional characterization of matrix proteins. *Comptes Rendus Palevol* 2004, 3, (6-7), 549-562.

14. Nys, Y.; Hincke, M. T.; Arias, J. L.; Garcia-Ruiz, J. M.; Solomon, S. E., Avian eggshell mineralization. *Poultry and Avian Biology Reviews* 1999, 10, (3), 143-166.

15. Cuif, J. P.; Dauphin, Y.; Doucet, J.; Salome, M.; Susini, J., XANES mapping of organic sulfate in three scleractinian coral skeletons. *Geochimica Et Cosmochimica Acta* 2003, 67, (1), 75-83.

16. Gautret, P.; Cuif, J. P.; Stolarski, J., Organic components of the skeleton of scleractinian corals - evidence from in situ acridine orange staining. *Acta Palaeontologica Polonica* 2000, 45, (2), 107-118.

17. Cuif, J. P.; Dauphin, Y., Proteoglycan diversity and aragonite crystallization patterns in coral skeletons: a reinterpretation of isotopic "biological mismatches". *Geochimica Et Cosmochimica Acta* 2002, 66, (15A), A159-A159.

18. Cohen, A. L.; McConnaughey, T. A., Geochemical perspectives on coral mineralization. *Biomineralization* 2003, 54, 151-187.

19. Parmentier, E.; Cloots, R.; Warin, R.; Henrist, C., Otolith crystals (in Carapidae): Growth and habit. *Journal of Structural Biology* 2007, 159, 462-473.

20. Falini, G.; Fermani, S.; Vanzo, S.; Miletic, M.; Zaffino, G., Influence on the formation of aragonite or vaterite by otolith macromolecules. *European Journal of Inorganic Chemistry* 2005, (1), 162-167.

21. Gebauer, D.; Volkel, A.; Colfen, H., Stable Prenucleation Calcium Carbonate Clusters. *Science* 2008, 322, (5909), 1819-1822.

22. De Yoreo, J. J.; Vekilov, P. G. In *Principles of crystal nucleation and growth*, 2003; Dove, P. M.; DeYoreo, J. J.; Weiner, S., Eds. Mineralogical Soc America: 2003: 57-93.

23. Niederberger, M.; Colfen, H., Oriented attachment and mesocrystals: Non-classical crystallization mechanisms based on nanoparticle assembly. *Physical Chemistry Chemical Physics* 2006, 8, (28), 3271-3287.

24. Xu, A. W.; Ma, Y. R.; Colfen, H., Biomimetic mineralization. *Journal of Materials Chemistry* 2007, 17, (5), 415-449.

25. Falini, G.; Fermani, S., Chitin mineralization. *Tissue Engineering* 2004, 10, (1-2):1-6.

26. Albeck, S.; Weiner, S.; Addadi, L., Polysaccharides of intracrystalline glycoproteins modulate calcite crystal growth in vitro. *Chemistry-a European Journal* 1996, 2, (3), 278-284.

27. Andrade, L. R.; Salgado, L. T.; Farina, M.; Pereira, M. S.; Mourao, P. A. S.; Filho, G. M. A., Ultrastructure of acidic polysaccharides from the cell walls of brown algae. *Journal of Structural Biology* 2004, 145, (3), 216-225.

28. Young, J. R.; Henriksen, K., Biomineralization within vesicles: The calcite of coccoliths. *Biomineralization* 2003, 54, 189-215.

29. Goldberg, W. M., Acid polysaccharides in the skeletal matrix and calicoblastic epithelium of the stony coral Mycetophyllia reesi. *Tissue & Cell* 2001, 33, (4), 376-387.

30. Arias, J. L.; Neira-Carrillo, A.; Arias, J. I.; Escobar, C.; Bodero, M.; David, M.; Fernandez, M. S., Sulfated polymers in biological mineralization: a plausible source for bio-inspired engineering. *Journal of Materials Chemistry* 2004, 14, (14), 2154-2160.

31. Cuif, J. P.; Dauphin, Y., The two-step mode of growth in the scleractinian coral skeletons from the micrometre to the overall scale. *J. Struct. Biol.* 2005, 150, 319-331.

32. Aizenberg, J.; Lambert, G.; Weiner, S.; Addadi, L., Factors involved in the formation of amorphous and crystalline calcium carbonate: A study of an ascidian skeleton. *Journal of the American Chemical Society* 2002, 124, (1), 32-39.

33. Aizenberg, J.; Lambert, G.; Addadi, L.; Weiner, S., Stabilization of amorphous calcium carbonate by specialized macromolecules in biological and

synthetic precipitates. *Advanced Materials* 1996, 8, (3), 222-225.

34. Aizenberg, J.; Weiner, S.; Addadi, L., Coexistence of amorphous and crystalline calcium carbonate in skeletal tissues. *Connective Tissue Research* 2003, 44, 20-25.

35. Beniash, E.; Aizenberg, J.; Addadi, L.; Weiner, S., Amorphous calcium carbonate transforms into calcite during sea urchin larval spicule growth. *Proceedings of the Royal Society of London Series B-Biological Sciences* 1997, 264, (1380), 461-465.

36. Raz, S.; Hamilton, P. C.; Wilt, F. H.; Weiner, S.; Addadi, L., The Transient Phase of Amorphous Calcium Carbonate in Sea Urchin Larval Spicules: The involvement of Proteins and Magnesium Ions in its Formation and Stabilization. *Advanced Functional Materials* 2003, 13, (6), 480-486.

37. Zhong, C.; Chu, C. C., Acid Polysaccharide-Induced Amorphous Calcium Carbonate (ACC) Films: Colloidal Nanoparticle Self-Organization Process. Langumuir 2009, 25, 3045-3049.

38. Kashchiev, D.; Sato, K., Kinetics of crystallization preceded by metastable-phase formation. *Journal of Chemical Physics* 1998, 109, (19), 8530-8540.

39. Lomakin, A.; Asherie, N.; Benedek, G. B., Liquid-solid transition in nuclei of protein crystals. *Proceedings of the National Academy of Sciences of the United States of America* 2003, 100, (18), 10254-10257.

40. Zhang, T. H.; Liu, X. Y., Nucleation: What Happens at the Initial Stage? *Angewandte Chemie-International Edition* 2009, 48, (7), 1308-1312.

41. Addadi, L.; Raz, S.; Weiner, S., Taking Advantage of Disorder: Amorphous

Calcium Carbonate and its Roles in Biomineralization. *Advanced Materials* 2003, 15, (12), 959-970.

42. Weiner, S.; Dove, P. M., An overview of biomineralization processes and the problem of the vital effect. *Biomineralization* 2003, 54, 1-29.

43. Weiner, S.; Levi-Kalisman, Y.; Raz, S.; Addadi, L., Biologically formed amorphous calcium carbonate. *Connective Tissue Research* 2003, 44, 214-218.

44. Webb, M. A.; Arnott, H. J., Inside Plant-Crystals - a Study of the Noncrystalline Core in Druses of Vitis-Vinifera Endosperm. *Scanning Electron Microscopy* 1983, 1759-1770.

45. Jin, L. W.; Claborn, K. A.; Kurimoto, M.; Geday, M. A.; Maezawa, I.; Sohraby, F.; Estrada, M.; Kaminsky, W.; Kahr, B., Imaging linear birefringence and dichroism in cerebral amyloid pathologies. *Proceedings of the National Academy of Sciences of the United States of America* 2003, 100, (26), 15294-15298.

46. Krebs, M. R. H.; Bromley, E. H. C.; Rogers, S. S.; Donald, A. M., The mechanism of amyloid spherulite formation by bovine insulin. *Biophysical Journal* 2005, 88, (3), 2013-2021.

47. Krebs, M. R. H.; MacPhee, C. E.; Miller, A. F.; Dunlop, L. E.; Dobson, C. M.; Donald, A. M., The formation of spherulites by amyloid fibrils of bovine insulin. *Proceedings of the National Academy of Sciences of the United States of America* 2004, 101, (40), 14420-14424.

48. Rogers, S. S.; Krebs, M. R. H.; Bromley, E. H. C.; van der Linden, E.; Donald, A. M., Optical microscopy of growing insulin amyloid spherulites on surfaces in vitro. *Biophysical Journal* 2006, 90, (3), 1043-1054.

CHAPTER 5

SYNTHESIS AND CHARACTERIZATION OF BIODEGRADABLE MALEIC CHITOSAN-PEGDA HYBRID HYDROGELS VIA PHOTOPOLYMERIZATION

Chao Zhong[†], *Jun Wu*[‡] *and C. Chang Chu*[†, ‡, *]

Fiber and Polymer Science Program, Department of Fiber science and Apparel design, Cornell University, Ithaca, New York 14853-4401

Biomedical Engineering Program, Cornell University, Ithaca, New York 14853-4401

Email: cc62@cornell.edu*

* To whom correspondence should be addressed. Phone: (607) 255-1938, Fax: (607) 255-1093.

† Department of Fiber science

‡ Biomedical Engineering Program

5.1 Abstract

A new family of pH-sensitive biodegradable maleic chitosan/polyethylene glycol diacrylate (PEGDA) hybrid hydrogels was synthesized in an aqueous solution via UV- photopolymerization. The precursor, maleic chitosan, was prepared via a simple one-step chemical modification of chitosan salts and characterized by FTIR, ^{1}H NMR and ^{13}C NMR. Maleic chitosan and PEGDA precursors of varied weight feed ratios were then mixed in an aqueous solution and directly photopolymerized for 10 minutes under a long wavelength (365 nm) UV-light using 4-(2-hydroxyethoxy) phenyl-(2-hydroxy-2-propyl) ketone (Irgacure 2959) as a photoinitiator. The swelling ratios, compressive moduli and interior morphologies of the hybrid hydrogels of varied weight feed ratio and molecular weight of PEGDA were investigated. Briefly, as the weight feed ratio of PEG-GA to maleic chitosan precursors increased, the swelling ratio decreased and compressive modulus increased as a result of the increasing densities of hydrogel networks, as indicated by the decreasing pore sizes of the hydrogel samples. The molecular weight of PEGDA had also a significant influence on the swelling ratios and compressive moduli of the hybrid hydrogels, with a decrease in swelling ratio and an increase in modulus as PEGDA molecular weight increased. Finally, the cell cytotoxity of both maleic chitosan and maleic chitosan /PEGDA hydrogels (using Bovine Endothelial Aorta Cell (BEAC) line) was evaluated based on MTT assay and live-dead assay, respectively. The results from MTT and live-dead assay indicated that maleic chitosan and maleic chitosan/PEGDA hydrogels are nontoxic to the BEAC cells. We expect to use the new biocompatible and biodegradable hydrogels as biomaterials for various biomedical applications.

Keywords: Maleic chitosan, Hydrogel and Photopolymerization

5.2 Introduction

Hydrogels are of keen interest in the field of tissue engineering and controlled drug delivery due to their biocompatibility, high water content, permeability for oxygen and nutrients, and tissue-like elastic properties [1-3]. Hydrogels can also be integrated with microdevices for different applications including biosensors [4] and diagnostic imaging [5] using photolithographic, molding, or other approaches [3]. Although natural physical hydrogels have been widely utilized for many biomedical applications, synthetic hydrogels provide better control over their final physical, structural, and mechanical properties[2, 6]. Several chemical approaches (for example: photo and thermal-initiated polymerization) have been used to prepare synthetic covalent hydrogels. Among all the approaches, photopolymerization has several inherent advantages. For example, it allows for better spatial and temporal control over polymerization and more rapid entrapment of cells with minimal cell death due to fast curing rates (less than a second to a few minutes). In addition, the gelation can be performed at physiological temperature and pH and even in situ in a minimally invasive manner [7]. Accordingly, photopolymerization is the preferred approach for preparation of covalent hydrogels, particularly for biomedical applications [8].

Chitosan is a partially deacetylated product of chitin, the second most abundant polysaccharide in nature. Chitosan is also a linear polycationic polysaccharide comprising glucosamine and N-acetylglucosamine residues. Due to its biocompatibility, biodegradability, non-toxicity and antimicrobial property [9-11], chitosan has been widely utilized for biomedical applications, such as controlled drug and protein delivery [12, 13], non-viral gene delivery [14], and tissue engineering [15-17]. It is also a potential biomaterial choice for preparation of photopolymerizable hydrogels for biomedical applications. For many tissue engineering applications, it is often desirable to encapsulate cells directly inside

hydrogels; this is extremely challenging with chitosan-only gels due to chitosan's insolubility in a neutral pH aqueous medium. Therefore, several types of water soluble photopolymerizable chitosan derivatives had been prepared to achieve this goal. These include azidobenzoic acid modified lactose chitosan (Az-CH-LA) [18, 19], methacrylated glycol chitosan [20] and methacrylated O-carboxymethyl chitosan [21]. The synthesis of these derivatives involves two separate reactions: the preparation of a water-soluble chitosan derivative, followed by the incorporation of photopolymerizable moieties into the water-soluble chitosan derivative. The relative low yield of the final products due to two-step reactions and the resulting derivatives with functional groups randomly distributed along the backbone make these newly-developed chitosan derivatives less attractive than those photopolymerizable counterparts developed from other polysaccharide, for example, dextran and hyaluronic acid.

In this paper, we report a new photopolymerizable water-soluble chitosan precursor, maleic chitosan, based on a simple one-step modification of chitosan salts. We integrate maleic chitosan and PEG derivative (polyethylene glycol diacrylate, PEGDA) in an aqueous medium via photopolymerization to form hybrid biodegradable hydrogels having pH sensitivity. The specific use of PEGDA as crosslinkers was based on reported studies that PEG hydrogels are nontoxic, non-immunogenic, and approved by the US Food and Drug Administration for various clinical uses [3]. PEG-based hydrogels are also one of the widely used materials for biomedical applications [22]. By varying the weight feed ratio of PEGDA to maleic chitosan and the molecular weight of PEGDA, we were able to tune the swelling ratio, mechanical property and pore sizes of the resulting hybrid hydrogels.

5.3 Experimental section

5.3.1 Materials

The starting material, chitosan (Sigma product) has 75% degree of deacetylation, with Brookfield viscosity 20.0-200cps (1% acetic acid) and molecular weight approximately 50,000 Daltons based on viscosity data. p-tolunesulfonic acid monohydrate (Alfa Aesar, Ward Hill, MA), sodium bicarbonate (Sigma), maleic anhydride (Fluka), poly(ethylene glycol) (weight-average molecular weight (Mw) 2000, 4000, 8000 g/mol, Aldrich Chemical Co.) and acryloyl chloride (Aldrich Chemical Co. (Milwaukee, WI) were all used without further purification. Triethylamine from Fisher Scientific (Fairlawn, NJ) was dried via refluxing with calcium hydride and then distilled before use. Formamide from EMD Chemicals (stored in refrigerator) was first unfrozen and used immediately. Other solvents including benzene, hexane and acetone were purchased from VWR Scientific (West Chester, PA) and used as received. PEGDA (M_w=700) from Sigma was used as received. 2-Hydroxy-l-[4-(hydroxyethoxy) phenyl]-2-methyl-l-propanone (Irgacure 2959) was donated by Ciba Specialty Chemicals Corporation.

3-(4, 5-Dimethylthiazol-2-yl)-2, 5-diphenyl tetrazolium bromide (MTT) purchased from Sigma (St. Louis, MO) was used to evaluate the cell toxicity of maleic chitosan and maleic chitosan/PEGDA hydrogel. Other chemicals and reagents if not otherwise specified were purchased from Sigma (St. Louis, MO).

5.3.2 Synthesis of N, O- Maleic Chitosan and PEGDA macromer precursors

Synthesis of N, O- Maleic Chitosan:

Chitosan powder (1.0 g) was added into 100 mL formamide solvent. p-Tolunesulfonic acid monohydrate (1.1 g) was then directly added into the dispersed chitosan solution. The mixed solution became transparent after stirring for 1 hour at room temperature, maleic anhydride solid (3.52 g, 6-fold in molar ratio of sugar units)

was then added into the solution under the protection of N_2 gas. Reaction then took place under stirring and N_2 at a constant temperature of 60 °C for 24 hrs. The resulting maleic chitosan in the solution was precipitated out by acetone, filtered, washed with copious amounts of acetone, and dried. Methanesulfonic (or tolunesulfonic) anions in the maleic chitosan were then removed by adding 0.1M $NaHCO_3$ solution. Finally, the solution was dialyzed against deionized water (MW cut off 12,000) and lyophilized for 3 days using a Virtis Freeze Drier (Gardiner, NY) under vacuum at -42°C to yield 89% of the maleic chitosan. The degree of substitution (DS) on the maleic chitosan is 1.17 based on the ^{1}H NMR.

Synthesis of PEGDA macromer

PEGDA was synthesized according to a modified procedure based on a previously reported method [23, 24]. Briefly, 1.5 mmol of PEG was dissolved in 150 mL of benzene and heated to 45 °C with stirring until a complete dissolution. After the solution was cooled to room temperature, 1.67 mL (12.0 mmol) of triethylamine, at a fourfold molar excess concentration (based on PEG diol end groups), was added to the PEG solution. Then, 0.97 mL (12.0 mmol) of acryloyl chloride, also at a fourfold molar excess concentration, was added dropwise to the PEG solution through a syringe. The mixture was stirred and heated to 80 °C for 3 h under nitrogen gas. The reaction was then stopped, and the insoluble triethylamine was removed by filtration. The PEGDA product was then precipitated from the solution by the addition of 700 mL of cold hexane. The PEGDA precipitate was collected using a funnel, redissolved in 20 mL of benzene, and reprecipitated by adding 700 mL of chilled hexane twice. The PEGDA polymer was finally dried for 24 h in a vacuum oven at 35 °C and the dry product was stored in the refrigerator (approximately 4 °C) for future use.

5.3.3 Preparation of Maleic Chitosan/PEGDA Hydrogels

The degree of substitution on maleic chitosan has an important influence on the formation and final property of the hybrid hydrogels. With a low degree of substitution (less than 0.6), the solubility of maleic chitosan in an aqueous solution is significantly decreased. When using a high degree of substitution of maleic chitosan (more than 1.6) for hydrogel formation, the resultant hydrogels are easily broken or even dissociate in water upon swelling because of their very high hydrophilicity. We found out maleic chitosan with a medium degree of substitution (0.8~1.4) is appropriate in terms of the ability of gel formation, gel stability and sufficient solubility in water. The parameters of maleic chitosan used for preparation of maleic chitosan hydrogels were thus chosen as follows: degree of substitution (DS) 1.17 and molecular weight (M_n) =52,000.

Maleic chitosan solution with a concentration of 3.5 % (w/v) was prepared by dissolving 0.350 gram maleic chitosan in 10 mL distilled water in a glass bottle. PEGDA (M_n=700 ~ 8000) with a pre-determined weight feed ratio to maleic chitosan (See Table 5.1) was then added to the prepared maleic chitosan solution. The photoinitiator, 4-(2-hydroxyethoxy) phenyl-(2-hydroxy-2-propyl) ketone (Irgacure 2959) was added to the precursor solution at a concentration of 0.1 %(m/v). The mixed solution was then stirred for 10 minutes at 50°C to ensure a complete dissolution of the photoinitiator. The homogenous, transparent solution (5mL in total) was first transferred to a custom-made 20 well Teflon mold (with 250μm volume per well) using a micropipette, and then irradiated by a long-wavelength UV lamp (365nm and 8W) at room temperature for 10mins. The reaction scheme is shown in Scheme 5.1. The resultant hydrogels were actually formed by photocrosslinking the unsaturated functional groups in maleic chitosan and PEGDA precursors (scheme 5.1). After photopolymerization, the hydrogel samples were immersed in distilled water at

room temperature for at least 3 days to leach out the unreacted chemicals. During this period, distilled water was replaced every 12 hours.

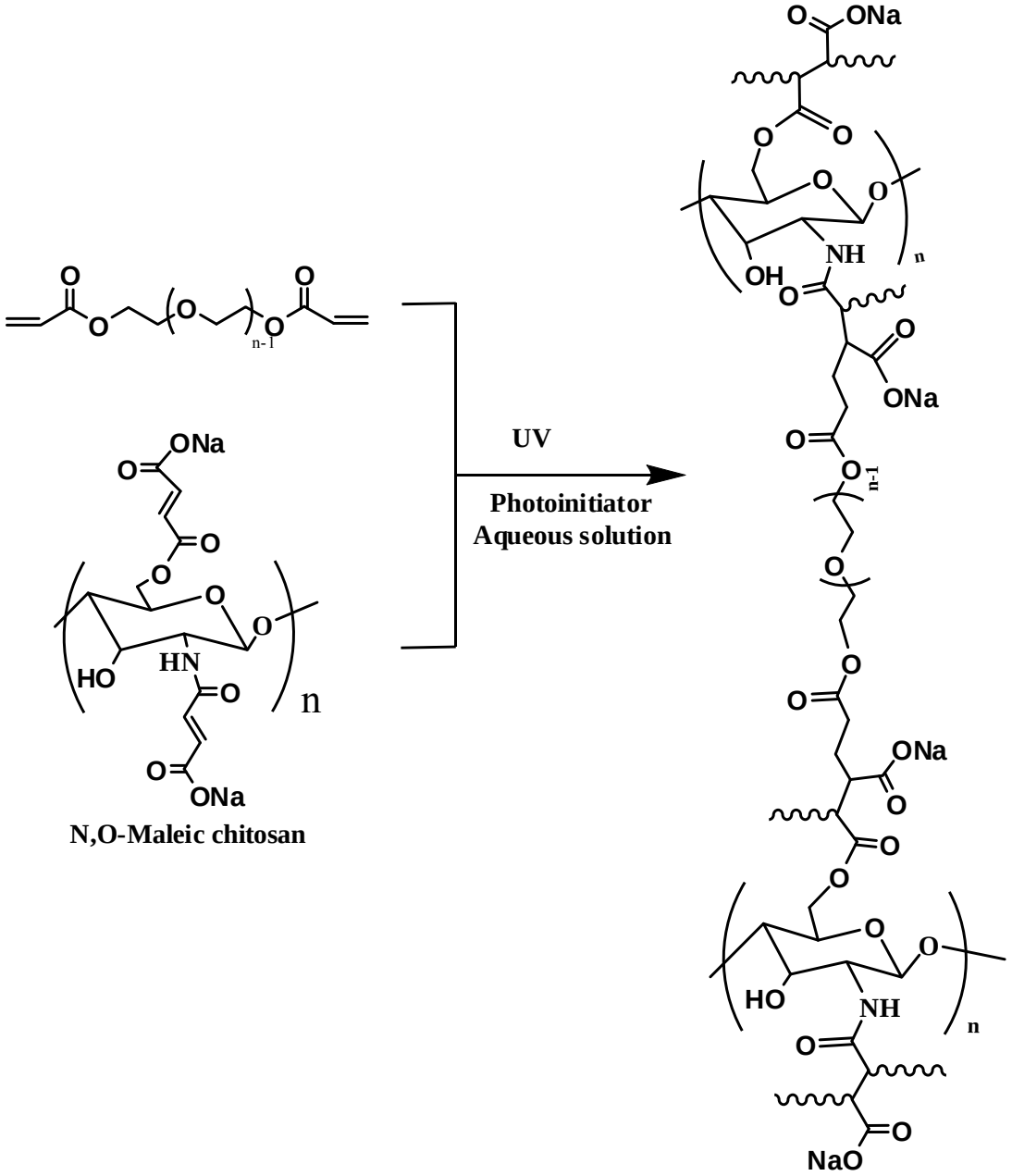

Scheme 5.1. One of the possible photocrosslinked structures via photopolymerization between N,O-maleic chitosan and PEGDA

5.4 Characterization

5.4.1 Characterization of Precursorss

Nucleation Magnetic Resonance (NMR)

Both ^{1}H and ^{13}C NMR spectra of maleic chitosan were recorded on a Varian (Palo Alto, CA) Unity INOVA 500-MHz spectrometer operating at 500 and 125.7 MHz, respectively. Samples of maleic chitosan (20 mg) were dissolved in 600μl of D_2O. Chemical shifts (δ) are reported in parts per million (ppm) using sodium 3-(trimethylsilyl) propionate-d4 as an internal standard. To get good signal, ^{13}C NMR tests were carried out at 343K for 12 hours. For PEGDA samples, only ^{1}H NMR spectrum was done to confirm that the purified product is free of any contaminants.

Total degree of substitution (DS) of maleic chitosan was determined from ^{1}H-NMR spectrum by comparing the signal integrals from the double bond signals (2 protons, 5.95~6.68 ppm) with the integrals of the polysaccharide backbone proton signals (5 protons, 3.5~4.0ppm). The assignment of the double bond peaks at different substituent positions was done by comparing the ^{1}H, ^{13}C NMR of N, O-maleic chitosan with those of N-maleic chitosan, and assuming that C-6 hydroxyl group is more reactive than C-3 hydroxyl group due to the steric hindrance of the C-3 hydroxyl group.

Molecular weight

Molecular weight was determined from the intrinsic viscosity data using Mark-Houwink equation. Specifically, we adopted the empirical equation, $[\eta] = 3.04\times10^{-5}\times M_r^{1.26}$ to determine the molecular weight of maleic chitosan [25].

5.4.2 Characterization of Maleic chitosan/PEGDA hybrid hydrogels

FT-IR:

For FTIR characterization, dried maleic chitosan-PEGDA hydrogels were ground into powder, mixed with KBr (sample/KBr 1:20 w/w), and compressed into

KBr pellets. FTIR spectra were then obtained with a PerkinElmer (Madison, WI) Nicolet Magana 560 FTIR spectrometer with Omnic software for data acquisition and analysis. For comparison, both precursors (maleic chitosan and PEGDA) were also grounded into powers and compressed into pellets for FTIR analysis.

SEM for freeze-dried Maleic-PEGDA hydrogels:

Interior morphology of maleic chitosan/PEGDA hydrogels were probed by SEM. The swollen hydrogel samples, after reaching their maximum swelling ratio in distilled water at room temperature after 24 hours, were quickly frozen in liquid nitrogen and then freeze-dried in a Virtis Freeze Drier (Gardiner, NY) under vacuum at -42°C for 3 days until all water was sublimed.

The freeze-dried hydrogel specimens were cut and fixed on aluminum stubs and then coated with gold for 30 seconds for interior morphology observation with a scanning electron microscope instrument (KECK FE-SEM, LEO 1550**)**.

Swelling ratio & swelling kinetics measurement in PBS and deionized water

The equilibrated swelling ratio (Q) was calculated as follows [26, 27]:

$$Q = \frac{W_s - W_d}{W_d} \times 100\%$$

Where W_s is the weight of swollen hydrogel at time t and W_d is the weight of the dry hydrogel at t = 0.

The swelling kinetics of the maleic chitosan-PEGD hydrogels were measured over a period of 5 days at room temperature. Dry Maleic chitosan-PEGDA gel samples were weighed and immersed in 20 mL of a phosphate-buffered saline buffer (PBS) solution (pH=7.4)or 20mL deionized water at room temperature for predetermined periods. The samples were removed from the PBS solution or deionized water, and blotted with filter papers to remove surface water. The samples were then weighed.

All swelling ratio results were obtained from triplicate samples and data were expressed as the means ± standard deviation.

Compressive modulus by Dynamic Mechanical Analyzer (DMA)

The mechanical property of the maleic chitosan/PEDGA hydrogels was measured by a DMA 2980 Dynamic Mechanical Analyzer (TA Instruments Inc., New Castle, DE) in a ‘‘controlled force’’ (CF-mode) mode. The swollen hydrogel samples in circular disc shape were submerged in distilled water and mounted between the movable compression clamp (diameter 30 mm) and the fluid cup with a 0.1 N preloading force. A force ramp from 0.1 to 1.5N, 2.0N or 2.5N (depending on the gel strength) at a rate of 0.3 or 0.5 N/min was applied. All measurements were carried out at room temperature. The compression elastic modulus (E) of the swollen hydrogel was extracted by plotting the compressive stress versus strain. All compression elastic modulus data in this study were obtained from triplicate samples and data were expressed as the means ± standard deviation.

5.4.3 Cytotoxicity of maleic chitosan and maleic chitosan/PEGDA hydrogel

Cell Culture

Bovine Endothelial Aorta Cells (BAEC, primary cells) were purchased from VEC Technologies, kindly offered by Professor Cynthia Reinhart-King at Department of Biomedical Engineering of Cornell University. BAECs were maintained at 37°C in 5% CO_2 in Medium 199 (Invitrogen, Carlsbad, CA) supplemented with 10% Fetal Clone III (HyClone, Logan, UT), and 1% each of penicillin–streptomycin, MEM amino acids (Invitrogen, Carlsbad, CA), and MEM vitamins (Mediatech, Manassas, VA). BAECs were used from passages 8–12. Media was changed every 2 days. Cells were grown to 70% confluence before splitting or harvesting. Cell culture plates were treated with 2 wt% gelatin aqueous solution before use.

Cytotoxicity of maleic chitosan

The evaluation of the cytotoxicity of maleic chitosan was performed by MTT assay. Maleic chitosan aqueous solution (5 wt%) was obtained by dissolving maleic chitosan in PBS buffer solution . Cultured Bovine Endothelial Aorta Cells were seeded at an appropriate cell density concentration (5, 000 cells/well) in 96-well plates and incubated overnight. After 12h, the cells were treated with the freshly prepared aqueous maleic chitosan solution with various volumes. Cells without maleic chitosan were used as control. After 48 h treatment and incubation, 20 μl of MTT solution (5 mg/ml) was added to each well, followed by a 4 h incubation at 37°C, 5% CO_2. Then the cell culture medium including polymer solution was carefully removed and 200 μl of acidic isopropyl alcohol (with 0.1 M HCl) was added to dissolve the formed formazan crystal. The plate was slightly shaken for 20 mins to make sure that the purple crystal dissolved completely. Absorbance (OD) was measured immediately at 570 nm (subtract background reading at 690 nm) using a microplate reader (VersaMax Tunable Microplate reader Molecular Devices, USA). The cell viability (%) was calculated according to the following equation:

$$\text{Viability}(\%) = (OD_{570(\text{sample})} - OD_{620(\text{sample})}) / (OD_{570(\text{control})} - OD_{620(\text{control})}) \times 100\%$$

Where, the $OD_{570(\text{control})}$ represents the measurement from the wells treated with medium only and the $OD_{570(\text{sample})}$ from the wells treated with various amount of maleic chitosan solution.

Cytotoxicity of maleic Chitosan/PEGDA hydrogels

The evaluation of the cytotoxicity of maleic chitosan/PEGDA hydrogels was performed by Live-Dead assay (invitrogen). Specifically, we selected maleic chitosan/PEGDA (8000) with a 1:3 weight feed ratio in this study. The purified hydrogels were cut into round shape (diameter: 1cm) and put into the 24-well cell culture plates after 30 min UV sterilization. Cultured Bovine Endothelial Aorta Cells

were seeded at an appropriate cell density concentration (10, 000 cells/well) and incubated overnight. After 24 h treatment and incubation, the live-dead assay was performed according to the manufacturer protocol (*LIVE*/*DEAD*® Cell Viability Assays from invitrogen).

5.5 Results and Discussion

5.5.1 Characterization of maleic chitosan

The incorporation of double bonds onto chitosan backbone was confirmed by ^{1}H NMR, as indicated by the appearance of the proton signals (from –C**H**=C**H**–) at δ 5.95, 6.42, and 6.68 ppm (Figure 5.1). This was also confirmed by FTIR upon the appearance of an absorption band at 808.6 cm^{-1}, corresponding to the unsaturated H–C= (–CH=CH–) out-of-plane deformation (Figure 5.3a). Correspondingly, the presence of new peaks around δ 120~150 ppm in ^{13}C NMR spectrum were due to the C signals from the double bonds, while the peaks around δ 170~180ppm in ^{13}C NMR could be ascribed to C signals from the carbonyl groups because of the newly formed ester, amide bonds and carboxyl groups(Figure 5.1b).

The several signals from double bonds in both ^{1}H NMR and ^{13}C NMR imply that the substitution of maleic anhydride took place more than one place in chitosan structure. The total degree of substitution (DS) of maleic chitosan was around 1.17, with DS 0.42, and 0.75 at C_6 and C_2 positions, respectively. The detailed assignment of these peaks can be found in Chapter One.

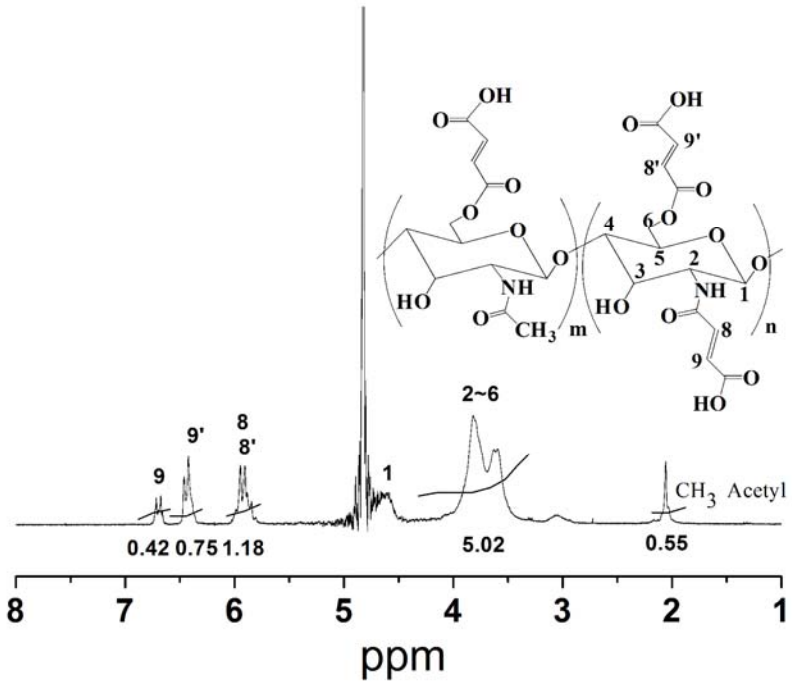

(a) ^{1}HNMR

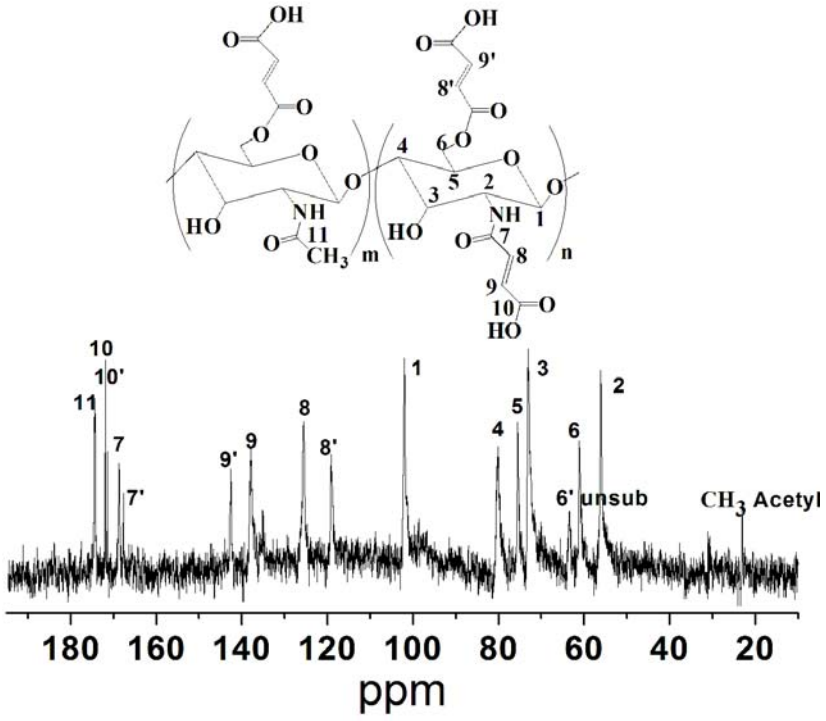

(b) ^{13}C NMR

Figure 5.1. (a) ^{1}H NMR and (b) ^{13}C NMR spectra of Maleic chitosan

5.5.2 Characterization and Properties of Maleic chitosan/PEGDA hybrid hydrogels

Theoretically, maleic chitosan contains double bond groups that could undergo free radical polymerization using a photoinitiator. But we found that maleic chitosan itself cannot form a hydrogel network using low concentration of maleic chitosan solution (e.g. 3.5wt% solution) or the resultant hydrogel, prepared using high concentration of maleic chitosan(e.g. 8.0 wt% solution), completely dissociate in water after swelling. This dissociation could partially arise from the formation of a relatively loose gel network because of the difficulty in self-polymerization between double bonds hindered by the end carboxyl groups.

In contrast, our group previously reported the successful gelation of maleic dextran macromers under UV light with a prolonged UV irradiation time (40 mins) [28]. The resultant hydrogels were very stable even after swelling. The difference between the reactivity of maleic chitosan and maleic dextran upon photopolymerization could be ascribed to the difference of their chain features. Specifically, we believe the branched chain of maleic dextran (due to the branched feature of dextran) might be more favorable to form a crosslinked network upon photopolymerization than the linear maleic chitosan as the branched maleic dextran can act as a crosslinker for itself. Therefore, in this study, PEGDA was added as a crosslinker to facilitate photopolymerization of maleic chitosan, with Irgacure 2959 acting as the photoinitiator to initiate photopolymerization in an aqueous system after 10 minutes UV irradiation. The initiator was previously reported to have minimal toxicity (cell death) over a broad range of mammalian cell types and species ranging from human fetal osteoblasts to bovine chondrocytes [29]. The hybrid hydrogels fabricated from low molecular weight PEGDA (M_n=700) usually became more and more opaque as the feed ratio of PEGDA to maleic chitosan precursors increased beyond 2:1, as shown in Figure 5.2 A. In contrast, the hybrid hydrogels fabricated

from high molecular weight PEGDA ($M_n \geqslant 2000$) are almost all transparent, even for those hybrid hydrogels prepared from high weight feed ratio of PEGDA to maleic chitosan (e.g. maleic chitosan/PEGDA(8000) hydrogel with a feed ratio 1:5, Figure 5.2 B).

The properties of these hydrogels, such as the swelling behavior, compression moduli and interior morphology were examined, and the dependence of these properties on the precursor feed ratios and the molecular weight of PEGDA, was examined as well. For convenience of discussion, the codes and the corresponding parameters including the feed ratios of macromer precursors used in the paper are summarized in Table 5.1.

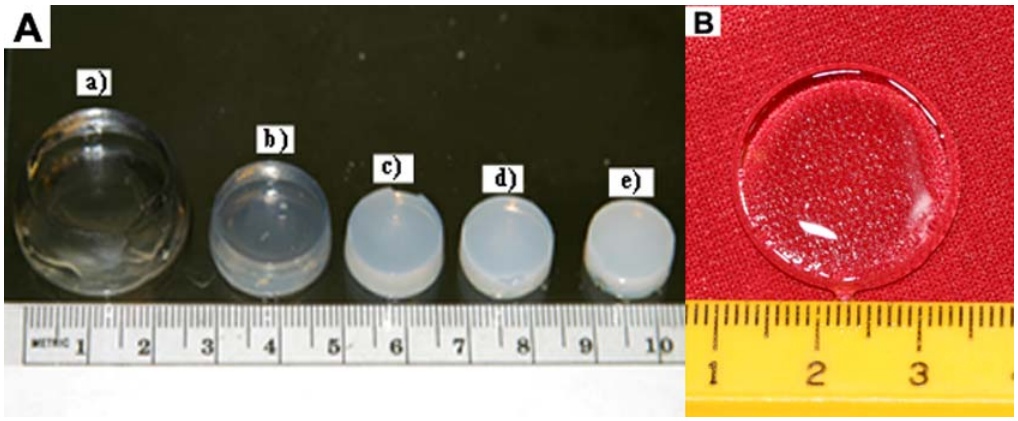

Figure 5.2. A) Digital image of Maleic chitosan-PEGDA hydrogels with different weight feed ratio of PEGDA (700) to maleic chitosan after reaching their swelling equilibrium: a).Maleic chitosan : PEGDA (700) = 1:1; b).Maleic chitosan : PEGDA (700) = 1:2; c) Maleic chitosan : PEGDA (700) = 1:3; d) Maleic chitosan : PEGDA(700) = 1:4; e) Maleic chitosan : PEGDA(700) = 1:5; B) Digital image of maleic chitosan-PEGDA(8000) with feed ratio of Maleic chitosan to PEGDA(8000) =1:5.

Table 5.1. Codes and corresponding feed ratios of maleic chitosan and PEGDA precursors for hybrid hydrogels.

Code	Molecular weight of PEGDA	Weight ratio of PEG-DA/ Maleic Chitosan	Double-bond ratio of PEG-DA/ Maleic Chitosan
MC-PEGDA1	**8000**	**2**	**0.134**
MC-PEGDA2	**8000**	**3**	**0.201**
MC-PEGDA3	**8000**	**4**	**0.267**
MC-PEGDA4	**8000**	**5**	**0.334**
MC-PEGDA (700)	**700**	**0.35**	**0.267**
MC-PEGDA (2000)	**2000**	**1**	**0.267**
MC-PEGDA (4000)	**4000**	**2**	**0.267**
MC-PEGDA (8000)	**8000**	**4**	**0.267**
Pure PEGDA	**8000**	**N/A**	**N/A**

5.5.2.1 Characterization of maleic chitosan/PEGDA hydrogels

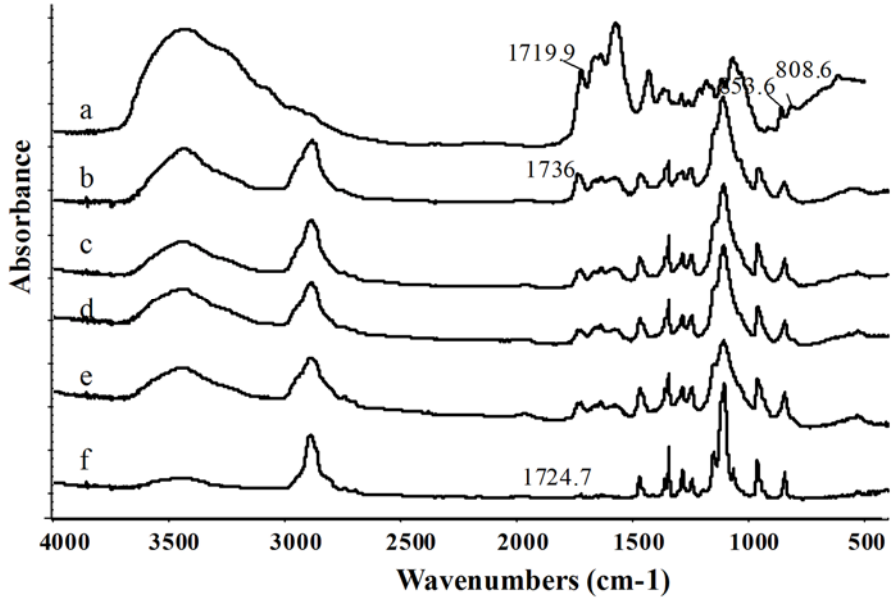

Figure 5.3. IR spectra of a) N, O-Maleic chitosan, b) Maleic Chitosan/PEGDA hydrogel with a weight feed ratio1/2), c) Maleic chitosan/PEGDA hydrogel with a weight feed ratio of 1/3, d) Maleic chitosan/PEGDA hydrogel with a weight feed ratio of 1/4 , e) Maleic chitosan/PEGDA hydrogel with a weight feed ratio of 1/5, f) PEGDA precursor (M_n=8000)

The FT-IR analysis was performed to ascertain the success of photopolymerization between maleic chitosan and PEGDA. The IR spectra of the hydrogel samples were compared with those of the corresponding precursors. As shown in Figure 5.3.f, the vital peaks present in the IR spectrum of PEGDA precursor (MW 8,000) were 2910 cm^{-1} for the alkyl–CH stretch, 1724.7 cm^{-1} for >C=O stretch (acrylate) and 1100 cm^{-1} for the ether (–C–O–C–) group. The main peaks in the IR spectrum of maleic chitosan precursor (Figure 5.3a) are: 3500~3200 cm^{-1} because of –OH and –NH stretch, 1720 cm^{-1} for the >C=O ester stretch and 808.6 cm^{-1} for the

–CH< (>CH=CH<) out-of-plane def. The IR spectra of all the hydrogel samples are similar, although they differed slightly among each other due to different weight feed ratios of the macromers precursors. Briefly, the intensity of the peak around 3500~3200 cm^{-1} (–OH and –NH stretch from maleic chitosan) decreases as a result of the increase in weight feed ratio of PEGDA to maleic chitosan (Figure 5.3b,c.d,e). The characteristic absorption peaks of >CH=CH< at 808.6 cm^{-1} (from maleic chitosan) almost disappeared in all gel samples. This observation indicated the success of crosslinking between maleic chitosan and PEGDA. Meanwhile, the shift of characteristic absorption peaks of the >C=O from both 1724cm^{-1}(ester groups of PEGDA due to conjugated with >C=C< before reaction) and 1719cm^{-1}(from ester groups of maleic chitosan due to conjugated with >C=C< before reaction) to an overlapped normal (saturated) ester group (1736cm^{-1}) in gel samples also suggested the coupling of the two macromer precursors.

5.5.2.2 Equilibrated swelling ratio & swelling kinetics of maleic chitosan/PEGDA in PBS and deionized water

The swelling kinetics of the maleic chitosan-PEGDA hydrogels were studied over a period of 5 days in DI water. As shown in Figure 5.4, all the maleic chitosan/PEGDA hydrogels of varied weight feed ratios generally showed a high swelling rate during the initial 3 hours, then leveled off thereafter, and finally reached their swelling equilibrium in about 2 days. Moreover, the swelling rate generally decreased with the increasing weight feed ratio of PEGDA to maleic chitosan, and are generally higher than that of pure PEGDA.

Equilibrated swelling ratio test was performed in both deionized water and PBS solution. Figure 5.5 shows the dependence of equilibrated swelling ratios at room temperature on the weight feed ratio of PEGDA to Maleic chitosan (M_n=8000) hybrid hydrogels. The equilibrated swelling ratio of hybrid hydrogels generally decreased

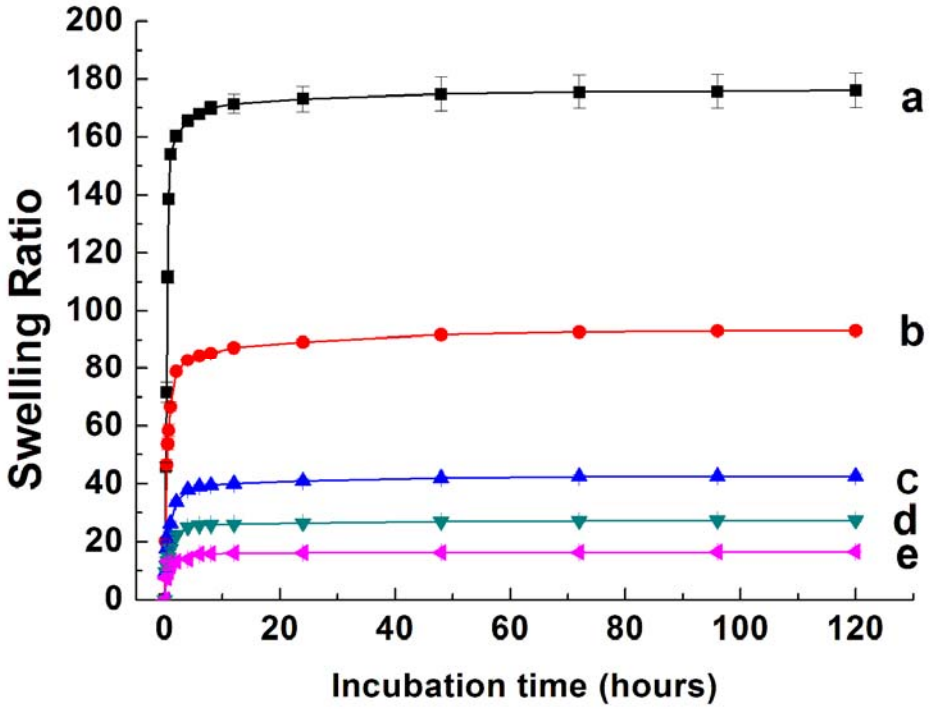

Figure 5.4. Swelling kinetics of maleic chitosan-PEGDA hydrogels with different weight feed ratios of PEGDA (8000) to maleic chitosan in DI water a).Maleic chitosan : PEGDA (8000) = 1:2; b).Maleic chitosan : PEGDA (8000) = 1:3; c) Maleic chitosan : PEGDA (8000) = 1:4; d) Maleic chitosan : PEGDA(8000) = 1:5; e) Pure PEGDA(8000) hydrogel (control).

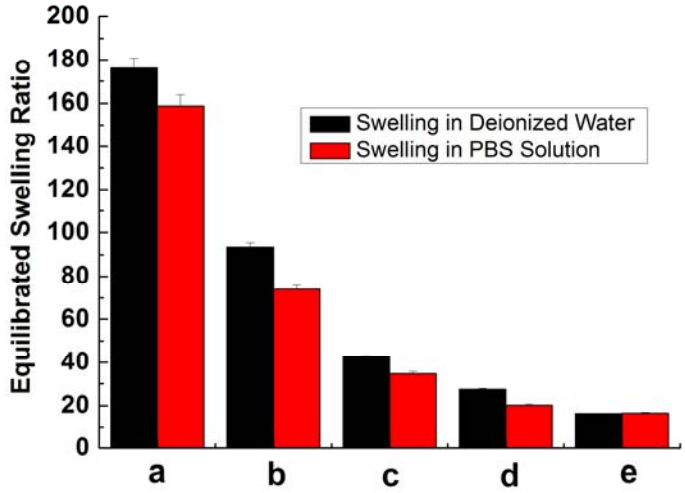

Figure 5.5. Dependence of equilibrated swelling ratio on the weight feed ratio of PEGDA (M_n=8000) to maleic chitosan in PBS (pH=7.4) solution and DI water. a) Maleic chitosan : PEGDA (8000) = 1:2; b) Maleic chitosan : PEGDA (8000) = 1:3; c) Maleic chitosan : PEGDA (8000) = 1:4; d) Maleic chitosan : PEGDA(8000) = 1:5 e) Pure PEGDA hydrogel (control)

with an increase in the weight feed ratio of PEGDA to maleic chitosan either in deionized water or PBS solution due to the increase in crosslinking density. For example, the hybrid hydrogel with a weight feed ratio of 2 has the highest equilibrium swelling ratio (176.1±4.5 and 158.8±4.9 in DI water and PBS, respectively.), while the hybrid hydrogel sample with a weight feed ratio of 5 has the smallest swelling ratio (27.4 ± 0.3 and 20.2 ± 0.46 in DI water and PBS, respectively). The swelling ratio of all maleic chitosan/PEGDA hybrid hydrogels are generally higher than that of pure PEGDA hydrogel (16.2 ± 0.21, 16.5± 0.34 in DI water and PBS, respectively) control sample, implying that the incorporation of carboxyl moieties did enhance the hydrophilicity of the hybrid hydrogels.

The fast swelling kinetics and high water retention ability of the hybrid hydrogels are due to their hydrophilic feature of the hybrid hydrogels. In contrast, Guo

et al. reported that a relatively hydrophobic hybrid hydrogel family containing amino acid-based poly (ester amide) (PEA)/PEGDA precursors. The hybrid hydrogel had a much slower swelling kinetics (around 12 hours before the swelling rate leveled off) and lower equilibrium swelling ratios (between 1 and 2400% in water).

The swelling ratios of maleic chitosan/ PEGDA hybrid hydrogels in DI water were always higher than that of the corresponding hydrogels in PBS solution (Figure 5.5, a,b,c,d), and the difference became smaller as the feed ratio of PEGDA to maleic chitosan precursors increased. No meaningful difference in swelling ratio between PBS and DI media was observed for the pure PEGDA hydrogel (Figure 5.5, e). This observation suggests that the free ions in PBS might interfere with the binding between water molecules and carboxyl groups in the gels.

To further understand the effect of ions on the swelling ratio of the hydrogels, we studied the effect of pH (varied H^+ concentration) on the swelling ratios of the hybrid hydrogels . The results are shown in Figure 5.6. As expected, the swelling ratios of the hybrid hydrogels are very sensitive to the change of pH, as indicated by the increasing swelling ratio with an increase in pH values, with the maximum swelling ratio at pH=11 and the lowest swelling ratio at pH=3 over the feed ratios studied. For example, for the hydrogels with a weight feed ratio of 2 (MC-PEGDA2), the swelling ratio at basic condition (pH=11) is almost 3 times than that at acidic condition (pH=3). This observation is consistent with the swelling behaviors of PEG-grafted poly (methacrylic acid) (PMAA) and maleic dextran hydrogels in Klier's [30] and Kim's [28] work, respectively. They proposed that hydrogen bond complexation between carboxyl groups and hydroxyl groups in hydrogel networks at acidic conditions led to the reduction in swelling ratio. Similarly, hydrogen bonds may also form in maleic chitosan/PEGDA hybrid gels due to the presence of both carboxyl and hydroxyl groups in acid conditions, thus resulted in lower swelling ratio.

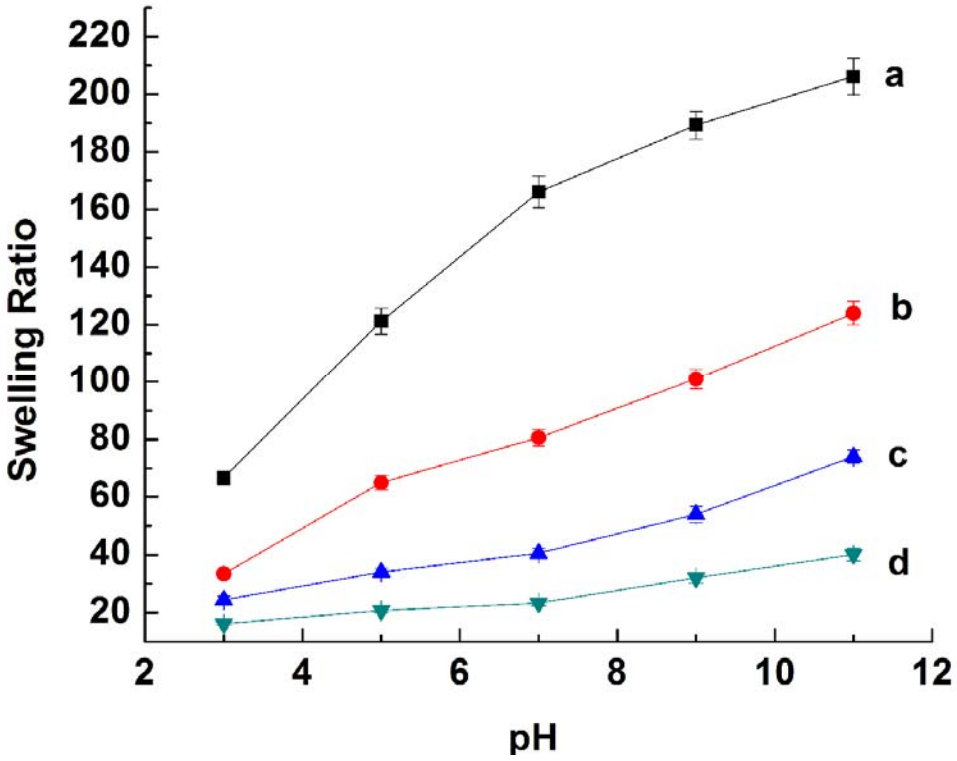

Figure 5.6 The swelling ratios of the hybrid hydrogels with different weight feed ratio in water as a function of the pH. a) Maleic chitosan : PEGDA (8000) = 1:2; b) Maleic chitosan : PEGDA (8000) = 1:3; c) Maleic chitosan : PEGDA (8000) = 1:4; d) Maleic chitosan: PEGDA(8000) = 1:5

We further investigated the effect of molecular weight of the co-precursor (PEGDA) on the swelling property of the hydrogels at a constant molar ratio of PEGDA to maleic chitosan (0.267, Table 5.1). As shown in Figure 5.7, the swelling ratio decreased as the molecular weight of PEGDA increased. At this molar ratio (0.267), maleic chitosan/PEGDA hydrogels could not be formed at all when PEGDA of molecular weight 700 was used. These observations suggest that low molecular weight of PEGDA might be less effective in crosslinking with maleic chitosan probably due to relatively short root-mean square distance of the molecules.

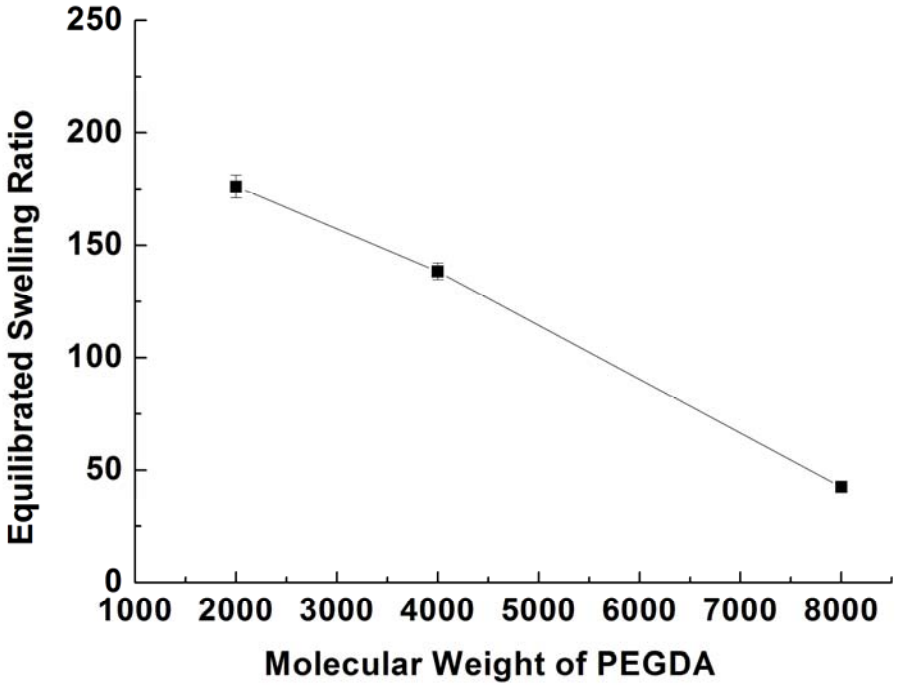

Figure 5.7. Effect of the molecular weight of PEGDA on the equilibrated swelling ratio of maleic chitosan/PEGDA hybrid hydrogels. Note: the data of maleic chitosan/PEGDA(700) was not listed here due to the failure of gel formation.

5.5.2.3 The mechanical property (compressive modulus) of maleic/PEGDA hydrogels

The mechanical property (compressive moduli) of maleic chitosan/PEGDA hydrogels was also evaluated using the Dynamic Mechanical Analyzer **(**DMA) in a controlled force (CF)-mode. Using DMA, the applicable range of compression forces was often limited. At a very low compression force, insufficient contacts between the geometry and the hydrogel surface might occur. The insufficient contacts at a low force could produce a deviation from linearity in the initial part of a typical stress-strain curve (Figure 5.8). In contrast, under a high compression force, the disk-like hydrogel samples showed a significant broadening of their diameter or even easily broke. The broadening of diameter at a high force causes a deformation in the horizontal direction and therefore results in an extra shear force. As illustrated in Fig 5.8, this could be observed as an upward deviation from the linear relation between the applied stress and the measured deformation in the CF-mode. Accordingly, a linear fit was applied to the curve in the medium force range in order to extract the storage moduli from the profiles (Figure 5.8, red-dotted line).

Typical stress-strain curves of maleic chitosan-PEGDA hydrogels with different weight feed ratio of PEGDA (8000) to maleic chitosan was shown in Figure 5.9. The calculated compressive moduli based on the linear fit approach described above are shown in Figure 5.10. The average modulus of maleic chitosan/PEGDA hydrogels increases with the increase of weight feed ratios, with 61± 1.9, 125.5± 11.1, 310.8± 23.7 and 560.4±18.1 KPa for the hybrid hydrogels with weight feed ratios from 2, 3, 4 and 5 respectively. This trend is a result of the increased crosslinking densities of the hydrogel networks due to the increased weight feed ratio of PEGDA to maleic chitosan.

We also tested the effect of molecular weight of the crosslinker, PEGDA, on the mechanical properties of the hydrogels by keeping a constant molar ratio of PEGDA to maleic chitosan (Table 5.1). As is shown in Figure 5.11, the compressive modulus appeared to increase as the molecular weight of PEGDA increases, with 60.9 ±6.5, 141.0±8.2, 310.8±23.7, for maleic chitosan/PEGDA (2000), maleic chitosan/PEGDA (4000) and maleic chitosan/PEGDA (8000), respectively. This trend could be directly relevant to the elastic chain length of PEGDA molecule. Each crosslinked chain of PEGDA can be considered as a small spring in a molecular level; therefore, their capability of resistance to compression depends on the length of the spring, with a longer chain more resistant to compression.

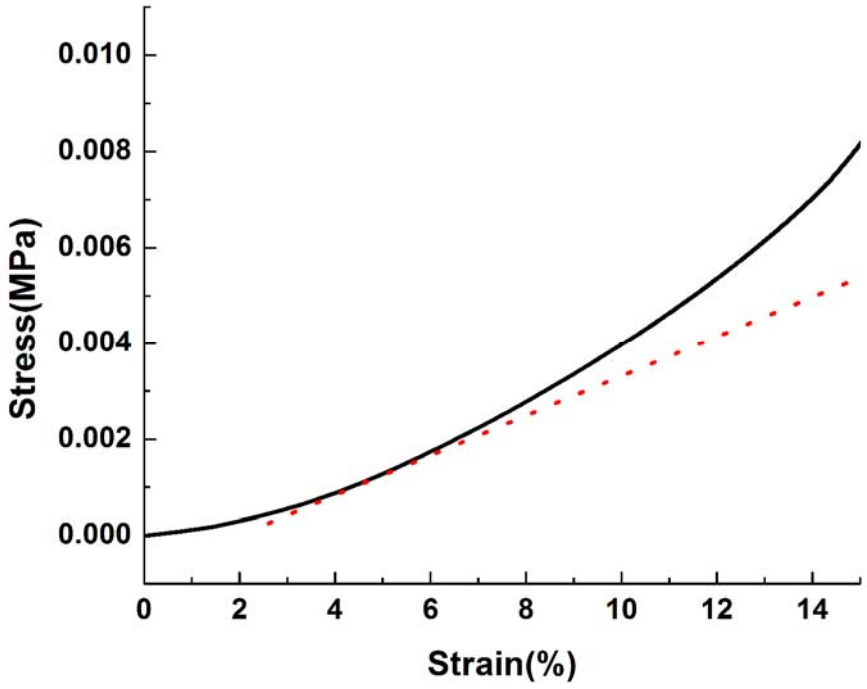

Figure 5.8. Typical compression profile (stress-strain curve) demonstrated by maleic chitosan /PEGDA(700) hydrogels with a weight feed ratio of 5:1 in the controlled force mode.

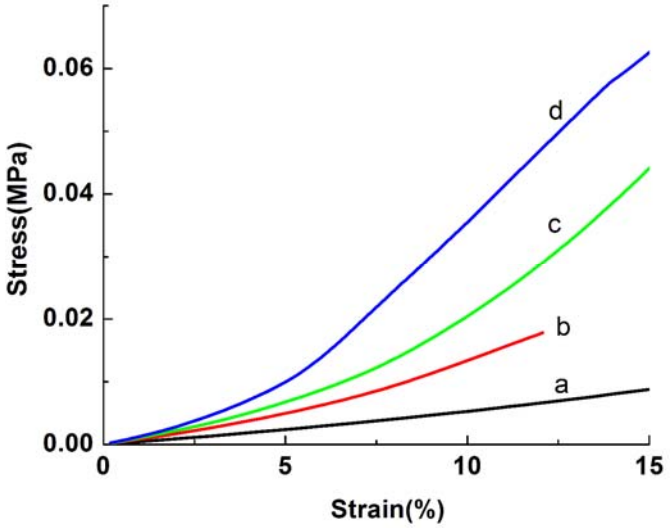

Figure 5.9. Stress-strain curves of Maleic chitosan-PEGDA hydrogels with different weight feed ratios of PEGDA (8000) vs maleic chitosan. a).Maleic chitosan : PEGDA (8000) = 1:2; b).Maleic chitosan : PEGDA (8000) = 1:3; c) Maleic chitosan : PEGDA (8000) = 1:4; d) Maleic chitosan : PEGDA(8000) = 1:5.

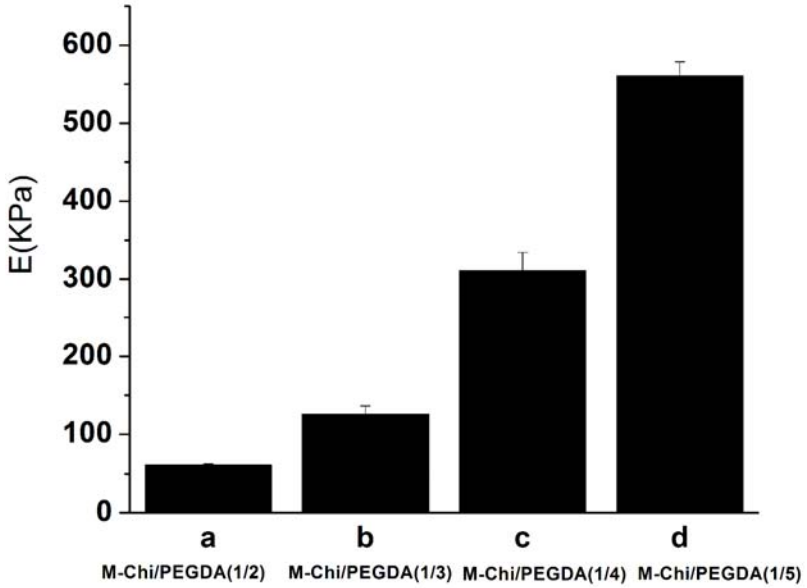

Figure 5.10. Calculated compression moduli of maleic chitosan-PEGDA hydrogels with different weight feed ratios of PEGDA (8000) to maleic chitosan. a) Maleic chitosan : PEGDA (8000) = 1:2; b) Maleic chitosan : PEGDA (8000) = 1:3; c) Maleic chitosan : PEGDA (8000) = 1:4; d) Maleic chitosan : PEGDA (8000) = 1:5

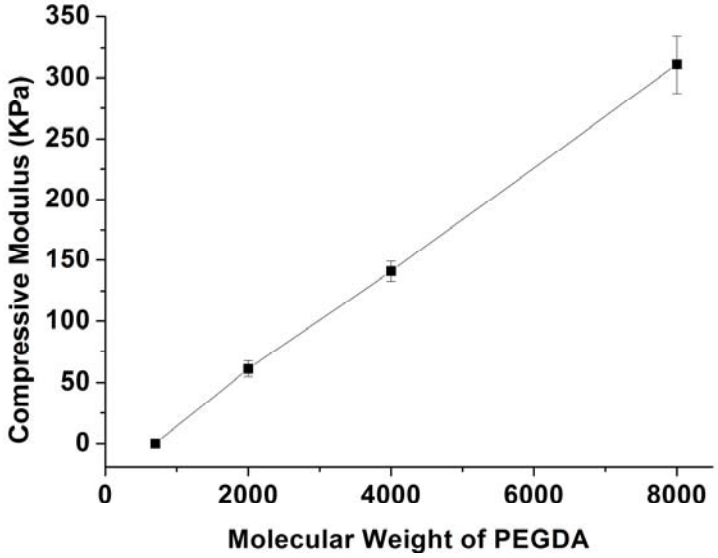

Figure 5.11. Effect of the molecular weight of PEGDA on the compressive modulus of maleic chitosan/PEGDA hybrid hydrogels with a constant double bond molar ratio (0.267) of PEGDA to maleic chitosan. Note: maleic chitosan/PEGDA (700) can not form a robust hydrogel in the study, so the compressive modulus was considered as zero in this plot.

5.5.2.4 Interior morphology (SEM) of maleic chitosan/PEGDA hydrogels

To understand the structure-function relationship of the hybrid hydrogels, we selectively examined the cross-section interior morphology of the maleic chitosan/PEGDA hybrid hydrogels. All the freeze-dried hydrogels display porous network structures (Figure 5.12). The average pore size of these honey-comb like porous structures decreased with an increase in the amount of cross-linker, PEGDA. For example, MCh-PEGDA5 (Fig. 5.12.g) had the smallest pore size with an average diameter 5μm, while the MC-PEGDA2 (Fig. 5.12.a) had the largest with an average diameter around 20μm.

Previous studies did suggest that the pore size of hydrogels depends on the actual crosslinking density, other than the molecular dimensions and hydrophilicity of the macromer [31]. The interior morphological data thus generally accords with the

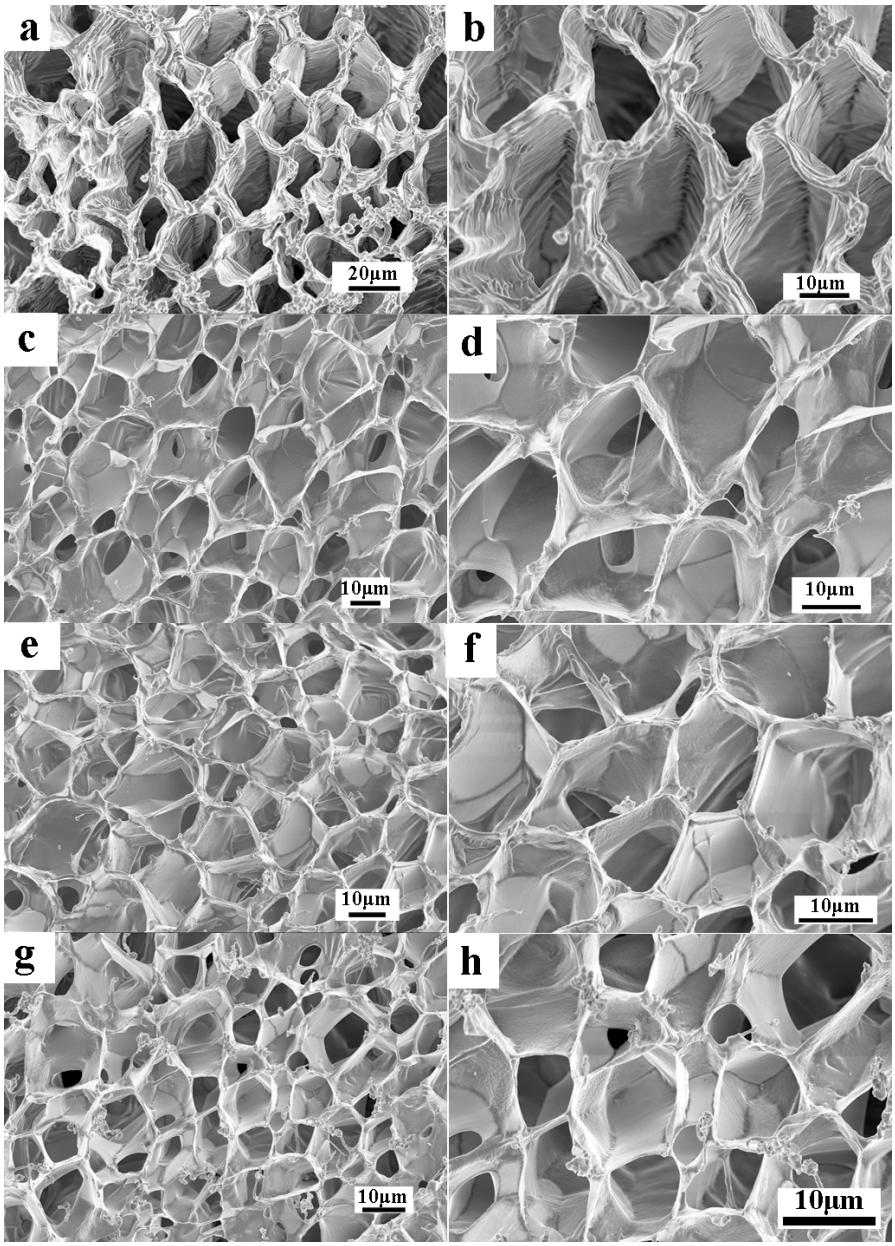

Figure 5.12. SEM images of Maleic chitosan-PEGDA hydrogels with different weight feed ratio of PEGDA (8000) vs maleic chitosan. a,b) Maleic chitosan : PEGDA (8000) = 1:2; c,d).Maleic chitosan : PEGDA (8000) = 1:3; e,f) Maleic chitosan : PEGDA (8000) = 1:4; g,h) Maleic chitosan : PEGDA(8000) = 1:5.

trends regarding swelling ratios and compressive moduli with the changes of weight feed ratio. Briefly, as PEGDA to maleic chitosan feed ratio increased, the crosslinking density of hydrogel networks increased, thus resulting in a tighter network structure reflected in a higher compressive modulus and a lower swelling ratio. Our results are also in agreement with previous studies regarding the effect of cross-linking densities on the swelling ratio and tensile properties of gels. For example, Ortega suggested that an increase in effective crosslink density with increasing crosslinking agent concentrations in tert-butyl acrylate-co-PEGDA gel networks led to decreasing equilibrium swelling ratios and increasing rubbery moduli [32].

5.5.3 Cytotoxicity of maleic chitosan and maleic chitosan/PEGDA hydrogels

The cytotoxicity of maleic chitosan and maleic chitosan/PEGDA hydrogels were both evaluated in this study. The cytotoxicity of maleic chitosan was assessed based on MTT assay, while that of maleic chitosan/PEGDA hydrogels was tested using a live-dead assay.

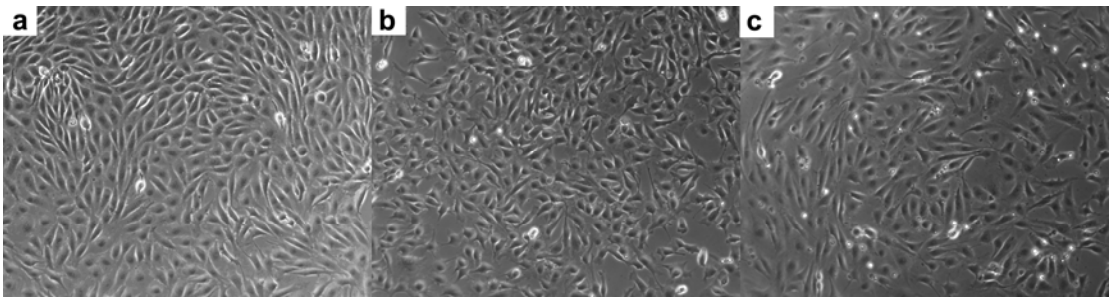

Figure 5.13. Typical light microscopy images of Bovine Endothelial Aorta Cells, a) cells treated with 0µl 5 wt% maleic chitosan solution for 48hours (control); b) cells treated with 60 µl 5 wt% maleic chitosan solution for 48hours; c) cells treated with 100 µl 5 wt% maleic chitosan solution for 48hours.

As shown in figure 5.13, no significant change of the morphology of the BAEC cells was detected under light microscope after 2 days' treatment, either with 60 µl or 100µl 5wt% maleic chitosan solution. Further, the data based on MTT assay indicated that more than 80% cell were still alive when treated with low dose of maleic chitosan solution (e.g. less than 10µl maleic chitosan solution) after 2 days (Figure 5.14). Even if treated with higher dose of maleic chitosan solution (e.g. as high as 100µl maleic chitosan solution), almost more than 60 percentage of the cells still survived after 2 days, indicative of low cytotoxicity of maleic chitosan to the cells (Figure 5.14). The low cycotoxicity of maleic chitodsan implies its potential as a biomaterial for various biomedical applications.

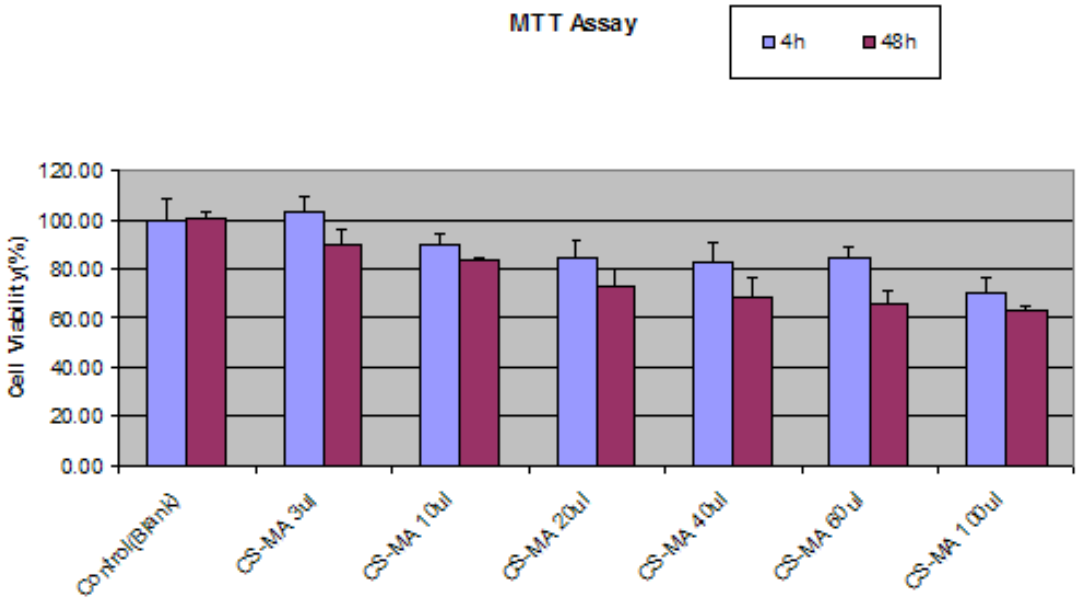

Figure 5.14. Scheme showing the Bovine Endothelial Aorta cell viability(%) after incubation in various amount of maleic chitosan solution for 4 h and 48 hours, respectively. All the data was based on the 3-(4,5-dimethylthiazol-2-yl)-2,5-diphenyltetrazolium bromide (MTT) assay. Cells in the absence of maleic chitosans were used as control samples. Error bars represent mean + SEM, * $P<0.05$, h: hour(s), number means the polymer concentration).

The MTT assay was not suitable to evaluate the cytotoxicity of maleic chitosan/PEGDA hydrogels because of the limited number of BAEC cells attached onto the hydrogel surface. Therefore, a live-dead assay was adopted to assess the cytotoxicity of maleic chitosan/PEGDA hydrogels. As we only aimed to test the viability of cells attached on the surface of the hydrogels in this study, the live-dead assay could be used as a preliminary evaluation of the hydrogel cytotoxicity.

In general, as shown in Figure 5.15, most of the attached BAEC cells were still alive and very few cells were observed dead on the hydrogel surface, implying that maleic chitosan/PEGDA hydrogel is not toxic to the BAEC cells, even though the hydrogel surface appears not to favor the attachment of BAEC cells. Further work regarding the enhancement of the BAEC cells attachment onto the hydrogel surface is being under investigation in our collaborative lab.

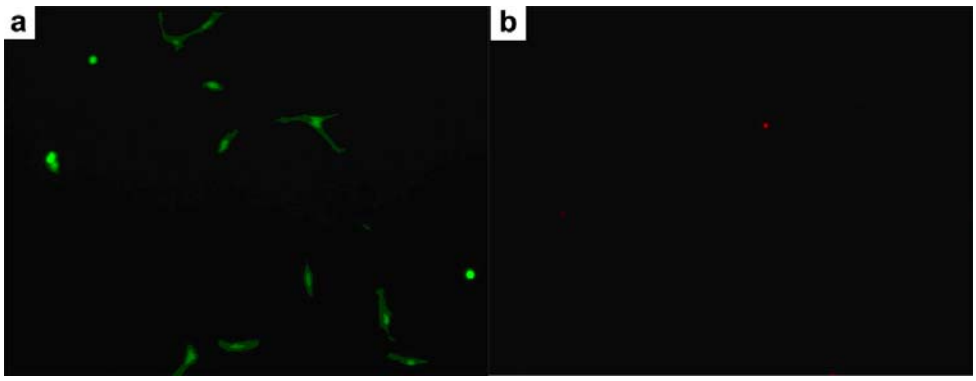

Figure 5.15. The live-dead assay for the BAEC cell attached on the hydrogel suface. a) the image showing the alive and healthy BAEC cells attached on the hydrogel surface, b) the image showing the dead or unhealthy cells on the hydrogel surface.

5.6 Conclusions

We reported here a new type of pH-sensitive biodegradable maleic chitosan/PEGDA hybrid hydrogels synthesized via UV-photopolymerization in

aqueous solutions. By varying the weight feed ratio of PEGDA to Maleic chitosan and the molecular weight of PEGDA, we were able to tune the swelling ratio, mechanical properties and pore sizes of hydrogels. The cytotoxicity data further indicated that maleic chitosan and maleic chitosan/PEGDA hydrogels are almost nontoxic to BAEC cells. We expect to use the new hydrogels as biomaterials for various biomedical applications.

5.7 Acknowledgement

This project was partially supported by the graduate student thesis funds from the College of Human Ecology at Cornell University and the Morgan Tissue Engineering Program. This work made use of the electron microscopy (SEM) and DMA facilities of the Cornell Center for Materials Research (CCMR) with support from the National Science Foundation Materials Research Science and Engineering Centers (MRSEC) program (DMR 0520404).

REFERENCES

1. Hoffman AS. Hydrogels for biomedical applications. *Advanced Drug Delivery Reviews* 2002;54(1):3-12.

2. Lee KY, Mooney DJ. Hydrogels for tissue engineering. *Chemical Reviews* 2001;101(7):1869-1879.

3. Peppas NA, Hilt JZ, Khademhosseini A, Langer R. Hydrogels in biology and medicine: From molecular principles to bionanotechnology. *Advanced Materials* 2006;18(11):1345-1360.

4. Ruan CM, Zeng KF, Varghese OK, Grimes CA. A magnetoelastic bioaffinity-based sensor for avidin. *Biosensors & Bioelectronics* 2004;19(12):1695-1701.

5. Kuang M, Wang DY, Bao HB, Gao MY, Mohwald H, Jiang M. Fabrication of multicolor-encoded microspheres by tagging semiconductor nanocrystals to hydrogel spheres. *Advanced Materials* 2005;17(3):267-270.

6. Lutolf MP, Hubbell JA. Synthetic biomaterials as instructive extracellular microenvironments for morphogenesis in tissue engineering. *Nature Biotechnology* 2005;23(1):47-55.

7. Decker C. Uv-Curing Chemistry - Past, Present, and Future. *Journal of Coatings Technology* 1987;59(751):97-106.

8. Nguyen KT, West JL. Photopolymerizable hydrogels for tissue engineering applications. *Biomaterials* 2002;23(22):00175-00178.

9. Kumar M. A review of chitin and chitosan applications. *Reactive & Functional Polymers* 2000;46(1):1-27.

10. Rabea EI, Badawy MET, Stevens CV, Smagghe G, Steurbaut W. Chitosan as antimicrobial agent: Applications and mode of action. *Biomacromolecules* 2003;4(6):1457-1465.

11. Rinaudo M. Chitin and chitosan: Properties and applications. *Progress in Polymer Science* 2006;31(7):603-632.

12. Singla AK, Chawla M. Chitosan: some pharmaceutical and biological aspects - an update. *Journal of Pharmacy and Pharmacology* 2001;53(8):1047-1067.

13. Dodane V, Vilivalam VD. Pharmaceutical applications of chitosan. *Pharmaceutical Science & Technology Today* 1998;1(6):246-253.

14. Borchard G. Chitosans for gene delivery. *Advanced Drug Delivery Reviews* 2001;52(2):145-150.

15. Khor E, Lim LY. Implantable applications of chitin and chitosan. *Biomaterials* 2003;24(13):2339-2349.

16. Madihally SV, Matthew HWT. Porous chitosan scaffolds for tissue engineering. *Biomaterials* 1999;20(12):1133-1142.

17. Suh JKF, Matthew HWT. Application of chitosan-based polysaccharide biomaterials in cartilage tissue engineering: a review. *Biomaterials* 2000;21(24):2589-2598.

18. Ono K, Saito Y, Yura H, Ishikawa K, Kurita A, Akaike T, et al. Photocrosslinkable chitosan as a biological adhesive. *Journal of Biomedical Materials Research* 2000;49(2):289-295.

19. Obara K, Ishihara M, Ishizuka T, Fujita M, Ozeki Y, Maehara T, et al. Photocrosslinkable chitosan hydrogel containing fibroblast growth factor-2 stimulates wound healing in healing-impaired db/db mice. *Biomaterials* 2003;24(20):3437-3444.

20. Amsden BG, Sukarto A, Knight DK, Shapka SN. Methacrylated glycol chitosan as a photopolymerizable biomaterial. *Biomacromolecules* 2007;8(12):3758-3766.

21. Poon YF, Bin Zhu Y, Shen JY, Chan-Park MB, Ng SC. Cytocompatible hydrogels based on photocrosslinkable methacrylated O-carboxymethylchitosan with tunable charge: Synthesis and characterization. *Advanced Functional Materials* 2007;17:2139-2150.

22. Varghese S, Elisseeff JH. Hydrogels for musculoskeletal tissue engineering. *Polymers for Regenerative Medicine* 2006:95-144.

23. Cruise GM, Hegre OD, Scharp DS, Hubbell JA. A sensitivity study of the key parameters in the interfacial photopolymerization of poly(ethylene glycol) diacrylate upon porcine islets. *Biotechnol Bioeng* 1998;57(6):655-665.

24. Cruise, G. M.; Scharp, D. S.; Hubbell, J. A. Characterization of permeability and network structure of interfacially photopolymerized poly(ethylene glycol) diacrylate hydrogels, *Biomaterials* 1998, 19, 1287–1294.

25. Roberts GAF, Domszy JG. Determination of the viscometric constants for chitosan. *International Journal of Biological Macromolecules* 1982;4(6):374-377.

26. Li Q, Wang J, Shahani S, Sun DDN, Sharma B, Elisseeff JH, et al. Biodegradable and photocrosslinkable polyphosphoester hydrogel. *Biomaterials* 2006;27(7):1027-1034.

27. Guo K, Chu CC. Synthesis and characterization of novel biodegradable unsaturated poly(ester amide)/poly(ethylene glycol) diacrylate hydrogels. *Journal of Polymer Science Part a-Polymer Chemistry* 2005;43(17):3932-3944.

28. Kim SH, Won CY, Chu CC. Synthesis and characterization of dextran-maleic acid based hydrogel. *Journal of Biomedical Materials Research* 1999;46(2):160-170.

29. Williams CG, Malik AN, Kim TK, Manson PN, Elisseeff JH. Variable cytocompatibility of six cell lines with photoinitiators used for polymerizing hydrogels and cell encapsulation. *Biomaterials* 2005;26(11):1211-1218.

30. Klier J, Scranton AB, Peppas NA. Self-associating networks of poly (methacrylic acid-*g*-ethylene glycol). *Macromolecules* 1990;23:4944–4949.

31. Wang D-AE, Jennifer H. *Photopolymerization.*: Marcel Dekker, Inc., New York,N.Y, 2004.

32. Ortega AM, Kasprzak SE, Yakacki CM, Diani J, Greenberg AR, Gall K. Structure-property relationships in photopolymerizable polymer networks: Effect of composition on the crosslinked structure and resulting thermomechanical properties of a (meth)acrylate-based system. *Journal of Applied Polymer Science* 2008;110(3):1559-1572.

CHAPTER 6

BIOMIMETIC MINERALIZATION OF ACID POLYSACCHARIDE-BASED HYDROGELS: TOWARDS POROUS 3-DIMENSIONAL BONELIKE BIOCOMPOSITES

Chao Zhong† and C. Chang Chu†, ‡,*

Fiber and Polymer Science Program, Department of Fiber science and Apparel design, Cornell University, Ithaca, New York 14853-4401

Biomedical Engineering Program, Cornell University, Ithaca, New York 14853-4401

Email: cz38@cornell.edu; cc62@cornell.edu*

† Department of Fiber science

‡ Biomedical Engineering Program

* To whom correspondence should be addressed. Phone: (607) 255-1938, Fax: (607) 255-1093.

Email: cc62@cornell.edu

6.1 Abstract

Biomimetic synthesis of bonelike composite materials is a promising strategy for the development of novel biomaterials for bone engineering applications. We report the use of a new acid polysaccharide-based hydrogel, maleic chitosan/PEGDA hybrid hydrogel as a 3-Dimensional (3-D) template for the growth of carbonated apatite, in conjunction with a modified simulated body fluid (SBF) mineralization approach. After mineralization, the porous gels became porous mineralized composites, with reduced pore sizes due to direct deposition of minerals along the wall of pores. The level of mineralization in the gels can be controlled by varying mineralization time, with 20.42±0.3%, 33.68±0.4% and 47.6±0.55 % (weight percentages) inorganic phase in the 3, 7 and 17-day mineralized dry samples, respectively. At 3 days, the mineral phase consisted of amorphous spherical nanoparticles embedded inside the surrounding organic layers; after 7 days, the mineral phase was plate-like calcium-deficient, carbonated-substituted crystalline hydroxyapatite. In contrast, only a very small amount of mineral phase was found to be randomly deposited inside a pure PEGDA hydrogel even after mineralization for 17 days. We suggest that the acid polysaccharide-based hydrogel not only provides reactive sites for the binding of mineral phase (because of the functionalized surface chemistry (carboxyl moieties), but also plays an important role in stabilizing amorphous inorganic nanophase at the very early stage. The new porous mineralized polysaccharide-based composites may be able to serve as scaffolds in bone tissue engineering.

KEYWORDS Maleic chitosan/PEGDA hydrogel, Biomineralization, Carbonated apatite and Bone tissue engineering

6.2 Introduction

Natural bone is an advanced composite material, comprising approximately 70% mineral (usually calcium-deficient, carbonate-substituted hydroxyapaptite nanocrystals) and 30% organics (including collagen, glycoproteins, proteoglycans and sialoproteins) by dry weight [1]. The organics themselves contain both proteins and polysaccharides, with the former being the focus of most theories of bone mineralization [2]. For example, it has been suggested that collagens serve as organic templates or frameworks for bone mineralization and that non-collagen anionic proteins can act as nucleators and inhibitors of mineral deposition [3, 4]. The role of polysaccharides has been given relatively little weight in most theories of bone mineralization despite several studies implying their importance in both bone formation and the maintenance of bone health, possibly modulating mineral size and crystallinity [5-9]. In particular, a recent study probing the interface between organic and inorganic phase in bone reveals that molecular constituents of the organic-mineral interface are predominantly polysaccharides (most likely glycosaminoglycan (GAG) sugars), rather than proteins as is widely assumed [2].

Biomimetic synthesis of bone-like composite materials using bone structure as a guide represents a promising strategy for development of novel biomaterials for various applications, including the direct treatment of bone defects and serving as bone engineering scaffolds [10]. Research efforts in this direction have focused mostly on the design and utilization of functional organic matrixes including collagens [11], peptides [12], peptide-amphiphile nanofibers [13], polymers (e.g. poly (propylene imine) dendrimer) [14] and polymer-based gels (e.g. poly-HEMA) [15] as the templates for the growth of inorganic phase (calcium phosphate) via several in-vitro biomimetic mineralization approaches. More detailed information in these topics can be found in several excellent reviews [1, 16, and 17]. In general, almost all these

synthetic strategies start from the assumption that proteins regulate normal bone biomineralization. However, the discovery that it is the GAGs that are intimately in association with mineral in bone underscores the importance of including polysaccharides in biomimetic strategies aimed at restoring or mimicking bone materials [2].

In this study, we report the use of an acid polysaccharide-based hydrogel, maleic chitosan/PEGDA hybrid hydrogel, as an organic template for the growth of carbonated apatite. The use of hydrogels as templates for biomimetic growth of bonelike minerals closely resembles the situations in bone, in which inherently hydrogel-like materials, collagen matrices, act as structural frameworks for mineral growth. Their intrinsic elasticity, porosity and water retention capacity of biodegradable hydrogels make them particularly good candidates as biomaterials for various biomedical applications including bone tissue engineering. The specific use of acid polysaccharide, maleic chitosan, accords with recent discovery regarding the importance of acid GAGs in bone mineralization. Using this new polysaccharide-based gel in conjunction with the simulated body fluid (SBF) biomimetic mineralization system [18], we were able to produce porous mineralized polysaccharide hydrogel composites. It is hoped that the new mineralized polysaccharide-based composites can serve as scaffolds in bone tissue engineering.

6.3 Experiments Section

6.3.1 Materials

2-Hydroxy-l-[4-(hydroxyethoxy) phenyl]-2-methyl-l-propanone (Irgacure 2959)) was donated by Ciba Specialty Chemicals Corporation. Maleic chitosan (Mn=5, 6000 and Degree of Substitution (DS) =1.2) and PEGDA (Mn=4000) was synthesized following our previous methods (Chapter 1 and 4). The Reagent-grade chemicals

$CaCl_2$, NaCl, KCl, $MgCl_2 \cdot 6H_2O$, K_2HPO_4, $NaHCO_3$, Na_2SO_4, and tris-hydroxymethyl aminomethane [$(CH_2OH)_3CNH_2$] and hydrochloric acid used for preparation of the SBF solutions were purchased from Sigma-Aldrich and used as received. Water used in all experiments was double distilled water.

6.3.2 Preparation of Maleic Chitosan-PEGDA hydrogel

Maleic chitosan-PEGDA hydrogels (with a weight feed ratio of maleic chitosan: PEGDA=1:3) were prepared via a photopolymerization approach. The specific selection of a weight feed ratio 1:3 was based on the observations that maleic chitosan/PEGDA hydrogel with this weight ratio has intermediate values of both equilibrated swelling ratio and compressive modulus among all the hydrogels with varied weight feed ratios studied (ranging from 1:1 to 1:5, Chapter 5).

Briefly, 3.5 % (w/v) maleic chitosan solution was prepared by dissolving 0.350 gram maleic chitosan in 10 mL distilled water in glass bottles. PEGDA (M_n=4000) with 1.05 gram (three times weight amount of maleic chitosan) was then added into maleic chitosan solution to form a mixed precursor solution. The photo initiator, 4-(2-hydroxyethoxy) phenyl-(2-hydroxy-2-propyl) ketone (Irgacure 2959) (10mg) was then added to the precursor solution with a concentration of 0.1% (m/v). The mixed solution was then stirred for 10 minutes at 50°C to ensure complete dissolution of the initiator. The homogenous, transparent solution (5mL in total) was first transferred to a custom-made 20 well Teflon plate (with 250μm volume per well) using a micropipette, and then irradiated by a long-wavelength UV lamp (365nm and 8W) at room temperature for 10mins. The resultant hydrogels with disk shapes were formed by photocrosslinking the unsaturated functional groups in maleic chitosan and PEGDA precursors (Scheme 6.1). After photopolymerization, the hydrogel samples were immersed in distilled water at room temperature for at least 3 days to leach out the unreacted chemicals. During this period, distilled water was replaced every 12 hours

to let the purified hydrogels reach equilibrium for different characterization. Detailed information regarding synthesis and characterization of Maleic chitosan-PEGDA can be found in Chapter 5.

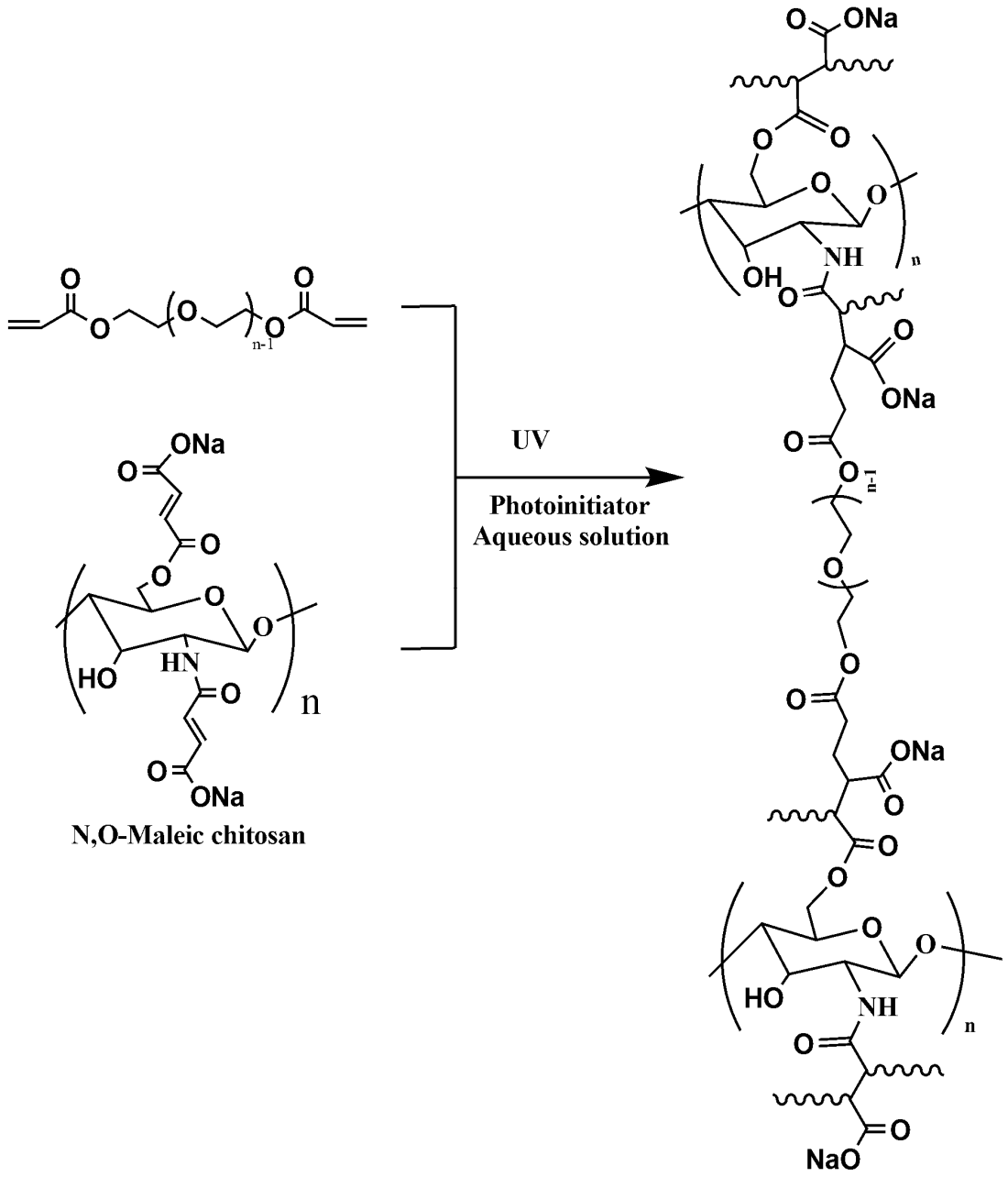

Scheme 6.1. UV-Photopolymerization between N,O-maleic chitosan and PEGDA leading to crosslinking structures

6.3.3 Biomimetic Mineralization

Direct mineralization of maleic chitosan-PEGDA hydrogel discs in simulated body fluid (SBF) without any pretreatments was carried out as a control experiment. The precipitation of minerals was completely inhibited even after 30-day mineralization due to the presence of great amount of carboxyl groups inside the hydrogel network. This observation is consistent with previous results regarding the inhibition of mineral deposition in the presence of acidic polymers (e.g. non-woven fabric composed of carboxymethylated chitin) or carboxyl group-containing crosslinked polymer networks(e.g. carboxymethylated chitin cross-linked by divinyl sulfone) in SBF [19,20].

Accordingly, we adopted a modified SBF mineralization procedure in this biomimetic mineralization study [19, 20]. Specifically, fresh maleic chitosan-PEGDA hydrogel discs were initially immersed in 10 mL 1mM $CaCl_2$ solution to allow Ca^{2+} ions to thoroughly bind with the carboxyl groups on the gel surface. After 2 hours, the gels were placed in 100 mL double-distilled water for 1 day to remove excessive Ca^{2+} and Cl^- ions. The purposes of these pre-handling procedures was to speed up mineralization process and try to reduce contaminants of free Ca^{2+} and Cl^- ions that might be introduced from these procedures.

The treated hydrogel discs were then transferred into 30 mL acellular simulated body fluid (SBF) of pH 7.40 and ionic concentrations (Na^+ 142.0 mM, K^+ 5.0 mM, Mg^{2+} 1.5 mM, Ca^{2+} 2.5 mM, Cl^- 147.8 mM, HCO^{3-} 4.2 mM, HPO_4^{2-} 1.0 mM and SO_4^{2-} 0.5 mM) nearly equal to those of human blood plasma. The SBF was prepared following a standard procedure [18] by dissolving reagent grade NaCl (8.035 g), $NaHCO_3$ (0.355g), KCl (0.225g), $K_2HPO_4{\cdot}3H_2O$ (0.231g), $MgCl_2{\cdot}6H_2O$ (0.311g), $CaCl_2$ (0.292g), and Na_2SO_4 (0.072g) into 1000 mL distilled water, and buffered at pH 7.40 with tris-hydroxymethyl aminomethane [$(CH_2OH)_3CNH_2$] and hydrochloric acid

at 36.5°C. After soaking for various periods (3, 7 and 17 days) at 37°C, the hydrogels were removed from the fluid, washed with distilled water for 3 times, and freeze-dried or air dried for later characterization.

6.3.4 Characterization

FT-IR

For FTIR characterization, mineralized maleic chitosan-PEGDA hydrogels were grounded into powder, mixed with KBr (sample/KBr 1:20 w/w), and compressed into KBr pellets. FTIR spectra were then obtained with a PerkinElmer (Madison, WI) Nicolet Magana 560 FTIR spectrometer with Omnic software for data acquisition and analysis. For comparison, pure maleic chitosan-PEGDA hydrogels were also grounded into powders and compressed into pellets for FTIR analysis.

SEM and Energy Dispersive X-ray (EDX) Spectroscopy

Both mineralized and unmineralized hydrogel samples were cut using a clean razor, and quickly frozen in liquid nitrogen and then freeze-dried in a Virtis Freeze Drier (Gardiner, NY) under vacuum at -42°C for 3 days until all water was sublimed. The dry hydrogel specimens were fixed on aluminum stubs and then coated with Au/Pd for interior morphology observation with a scanning electron microscope instrument (KECK FE-SEM, LEO 1550**)**. The experiments were performed at a low accelerating voltage (3 KeV), especially suitable for imaging the surface detail of low-density materials. The SEM facility was also equipped with EDX energy-dispersive spectrometer for microchemical analysis.

Wide-angle X-ray diffraction (WXRD)

WXRD was used to evaluate the crystal phase and crystallographic orientations of the inorganic phase grown onto the gel. The general area detection diffraction system (GADDS, Bruker-AXS, Inc., Madison, WI) was used at 45 kV and 40mA. The X-ray diffraction patterns of the specimens were obtained using a Scintag

θ-θ powder diffractometer (PAD X, Scintag, Inc., Cupertino, CA) with a solid-state intrinsic germanium detector. The specimen powders were scanned from 1° to 50° at 2°/min employing the Cu Kα X-ray radiation with a wavelength of 1.5405 Å. The *d* spacing information was recorded.

Thermogravimetric Analysis (TGA)

Air-dried unmineralized and mineralized hydrogel samples were used for TGA test. The amounts of both organic and inorganic components were evaluated using a thermogravimetric analyzer (TGA), model 2050, (TA Instruments, New Castle, DE). All specimens were scanned from 25 °C to 700 °C at a ramp rate of 10 °C/min. All TGA tests were carried out in nitrogen environment. All qualitative data based on the TGA curves in this study were obtained from triplicate samples and data were expressed as the means ± standard deviation.

Transmission Electron Microscopy (TEM)

A 3-day mineralized hydrogel sample was embedded in epoxy (Unicryl embedding kit, EMS) and microtomed (diamond knife) into slices of around 50 nm thick. TEM was performed on a FEI Technai T12 at 120 kV. Selected area electron diffraction (SAED) was recorded using the same equipment.

6.4 Results and Discussions

Maleic Chitosan/PEGDA hydrogel disks were used as 3-dimensional microporous templates for biomimetic mineralization in this study. As shown in Figure 6.1a, the gel was transparent before mineralization; however, it became opaque after mineralization for 17 days. A typical interior morphology of the freeze-dried hydrogel sample (before mineralization) was shown in Figure1b. The hydrogel has interconnected pore structures with an average pore size around 15μm (Figure 6.1b and c). After mineralization for 17 days, the hydrogel surprisingly still had a porous

structure (Figure 6.1d), even though the average pore size of the hydrogel was significantly decreased (around 5μm from 15 μm). This pore size reduction was due to the deposition of mineral phase directly on the wall surface of pores (Figure 6.1e).

Image of a higher resolution of the mineralized pores revealed that the surface of mineralized hydrogel became very rough due to the appearance of nanoscale inorganic phase (Figure 6.1f). Energy-dispersive X-ray spectroscopy (EDX) confirmed the presence of calcium (Ca) and phosphorus (P) elements in the inorganic phase (Figure 6.1d insert). Further, FTIR spectrum suggests, other than the feature peaks from organic phase (for example: 2920 cm^{-1} for the alkyl–CH stretch from PEGDA and several peaks between 1200-1400 cm^{-1} from maleic chitosan polysaccharide signals), the major inorganic phase is hydroxyapatite, as indicated by the presence of enhanced broad bands for O-H stretching at 3400 cm^{-1} and several sharp peaks of PO_4^{3-} including the bending modes at 602 and 560 cm^{-1}(ν_4) and the antisymmetric stretching vibration at 1089 and 1045 cm^{-1}(ν_3) (Figure 6.2). In addition, several weak peaks for CO_3^{2-} also appear in the FTIR spectrum. These include the out-of plane bending adsorption at 870 cm^{-1} (ν_2) and the splitting at 1417 and 1467cm-1 due to the asymmetric stretch of the carbonate ion (ν_3). The presence of CO_3^{2-} implies that OH^- and/or PO_4^{3-} sites of hydroxyapatite are likely to be partially substituted by carbonate ions. Moreover, the peaks at 1645 cm^{-1} suggests that the mineral phase may also contain small amounts of occluded water [21] and/or HPO_4^{2-} groups substituting on the phosphate sites [22]. The results are in accordance with the observations from XRD patterns (Figure 6.3). Compared with the reference XRD data of hydroxyapatite (Figure 6.4), the patterns of mineralized hydrogel sample almost match those of hydroxyapatite reflections, with several small peaks probably ascribed to the various substituted hydroxyapatites (Table 6.1).

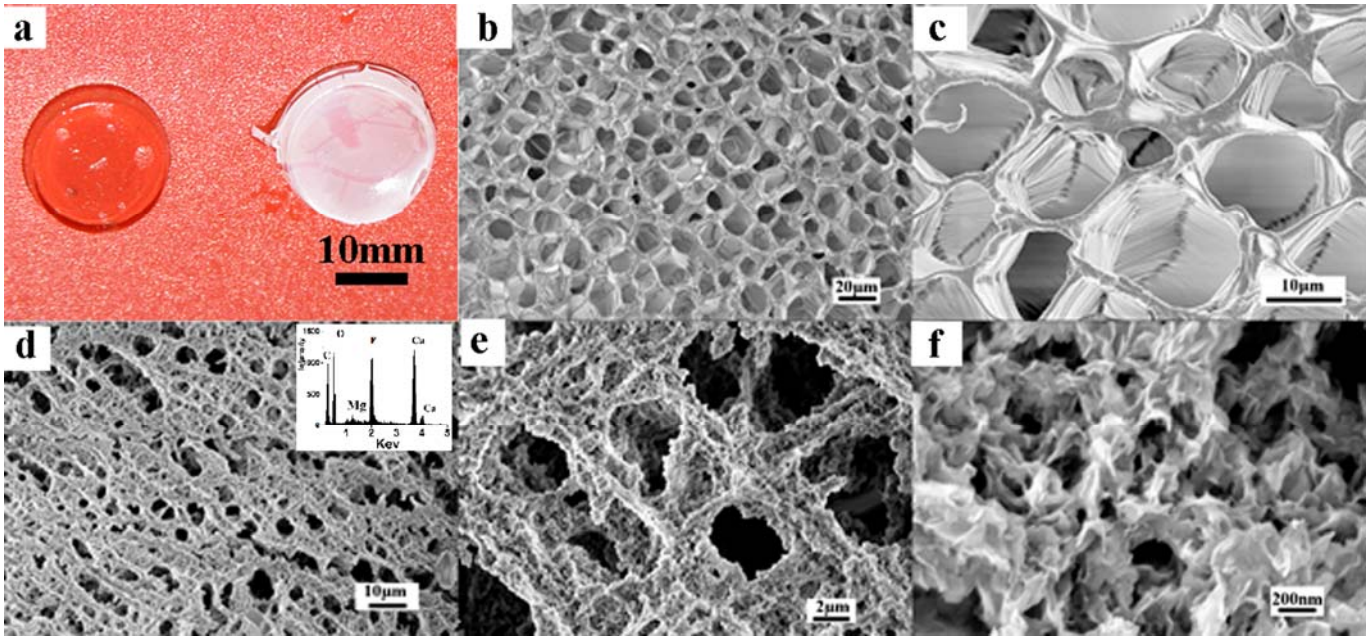

Figure 6.1. Images of unmineralized and mineralized Maleic Chitosan/PEGDA hydrogel (mineralization time 17days): (a) Digital Camera Image showing unmineralized gel (left) and mineralized hydrogel(right), (b-c) SEM images of unimineralized hydrogel, (d-f) SEM images of 17-day mineralized hydrogel.

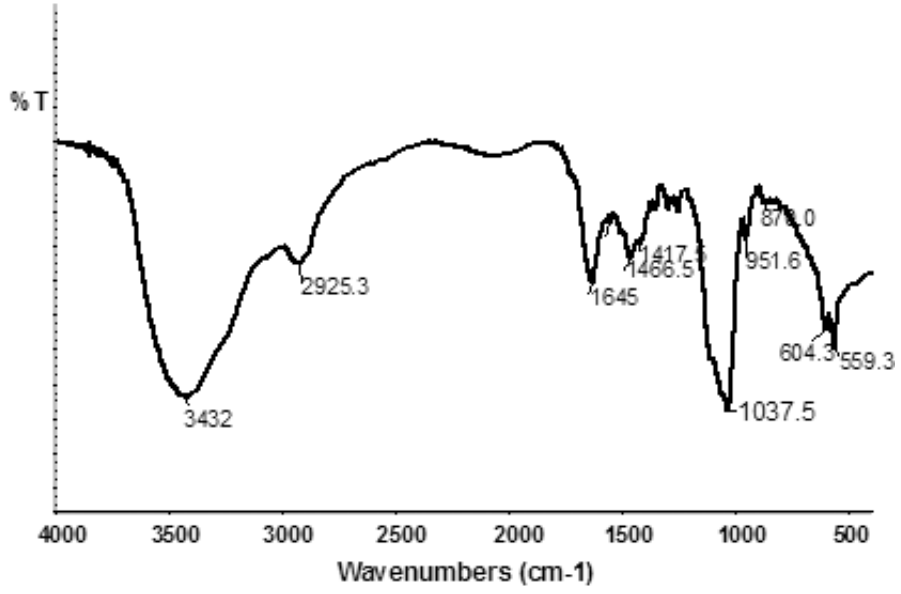

Figure 6.2. FTIR spectrum of 17-day mineralized gel

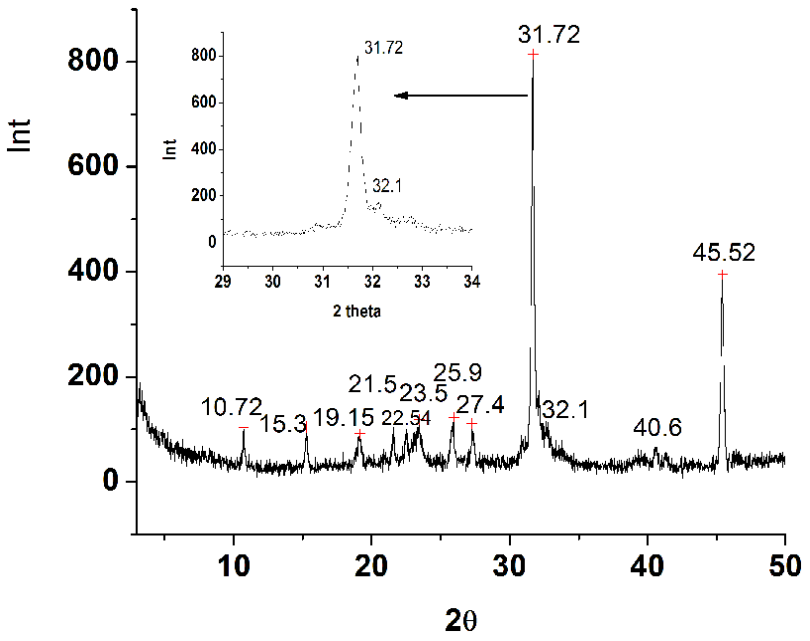

Figure 6.3. WXRD reflections of the CaP deposits formed on Maleic Chitosan/PEGDA hydrogels after 17-day incubation in SBF

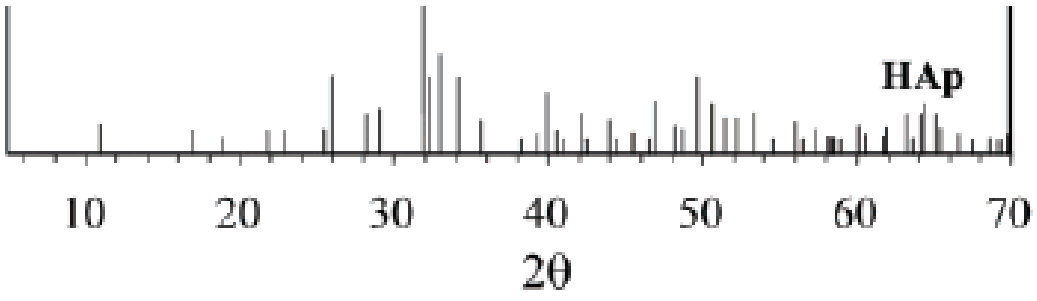

Figure 6.4. Standard XRD reflections of Hydroxyapatite pattern

Table 6.1. XRD reflections of the CaP deposits formed on maleic Chitosan/PEGDA hydrogels after 17days incubation in SBF

2θ	Reflection (hkl)	CaP phase
10.72	**100**	**HAP**
15.3		
19.15		
21.5		
22.54		
23.55		
25.80	**002**	**HAP (Hydroxyapatite)**
27.40		
31.72	**211**	**HAP**
32.1	**112**	**HAP**
39.3	**212**	**CHAP(Carbonated HAP)**
40.6	**221**	**HAP**
45.42	**203**	**HAP**

To understand the deposition process of mineral phase inside the maleic chitosan/PEGDA gel matrix, we examined the interior morphology of mineralized gels at the early mineralization stages. Typical SEM images of the hydrogels after mineralization for 3 and 7 days were shown in Figure 6.5. As expected, gels at the early mineralization stages also have a porous structure (Figure 6.5a and d), which is consistent with the results of 17-day mineralized gel we presented above. EDX data of both samples reveals that Ca and P elements are present in the samples (Figure 6.5a and d insert), indicative of initial deposition of mineral phases occurring even before these early stages. The EDX data showed that the Ca/P molar ratio decreased with mineralization time, with molar ratios of 1.64, 1.41 and 1.37 for 3-day, 7-day and 17-day mineralized sample, respectively. The Ca/P ratios in these samples are all below the stoichiometric 1.67 for hydroxyapatite [$Ca_{10}(PO_4)_6(OH)_2$], and thus belong to "calcium-deficient apatites", possibly involving cation substitutions at the Ca^{2+} sites, and/or the substitution at PO_4^{3-} sites by HPO_4^{2-} ions[23]. It is noted that the element Mg (small amounts) and the band of HPO_4^{2-} were indeed identified in corresponding EDS (Figure 6.1d, 6.5a and 6.5d insert) and FTIR spectra (Figure 6.2), respectively.

Although both 3 and 7-day mineralized hydrogels have similar porous structures, the detailed surface morphologies of these gels in nano-scale are different. Only small plate-like inorganic phases (similar to the 17-day mineralized gel, Figure 6.1f) were found on the surface of 7-day gel (Figure 6.5f). In contrast, spherical nanoparticles around 50nm were visualized and embedded within an organic-like matrix in the 3-day mineralized hydrogel sample (Figure 6.5b, c). This presence of spherical nanoparticles inside the organic hydrogel matrix seems to imply that amorphous calcium phosphate was likely to precipitate as early-stage products [24]. Under TEM observation (Figure 6.6a), spherical naonoparticle aggregates were glued together by continuous organic-like networks with amorphous feature confirmed by

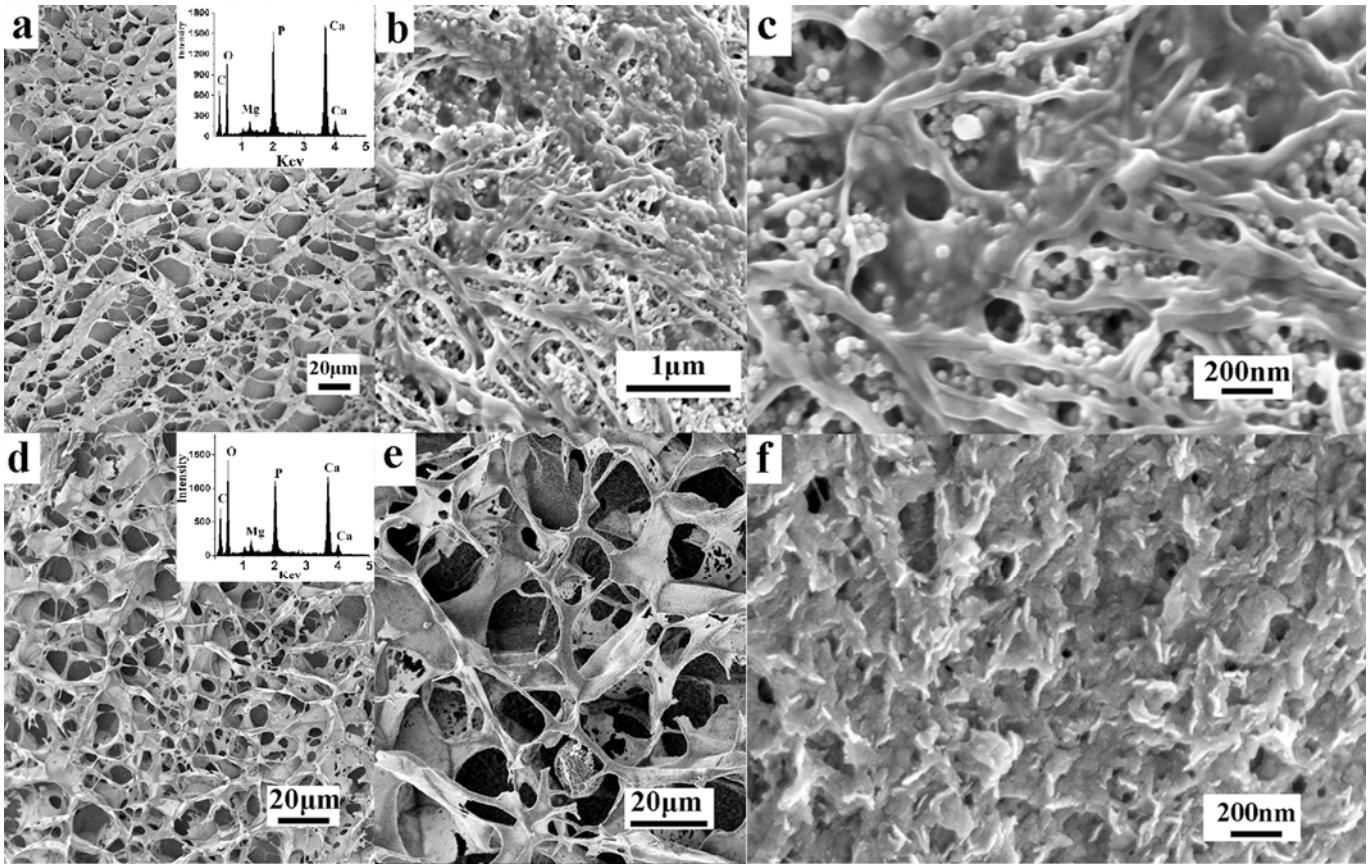

Figure 6.5. SEM Images of 3 and 7-day mineralized gel samples: a-c) 3-day mineralized gel sample, d-f) 7-day mineralized gel sample.

the appearance of diffuse rings in the SAED pattern (Figure 6.6b). The amorphous feature of 3-day mineralized hydrogel sample is further supported by the FTIR data shown in Figure 6.7. The broad, relatively unresolved phosphate bands at 590–610 cm^{-1} and around 1000 cm^{-1} are indicative of poor crystallinity of the 3-day hydrogel samples (Figure 6.7b), whereas, characteristic splitting of corresponding phosphate bands into peaks at 565/605 and 1050/1100 cm-1 suggest increasing crystallinity of the 7 or 17-day samples (Figure 6.7c and d)[21, 25].

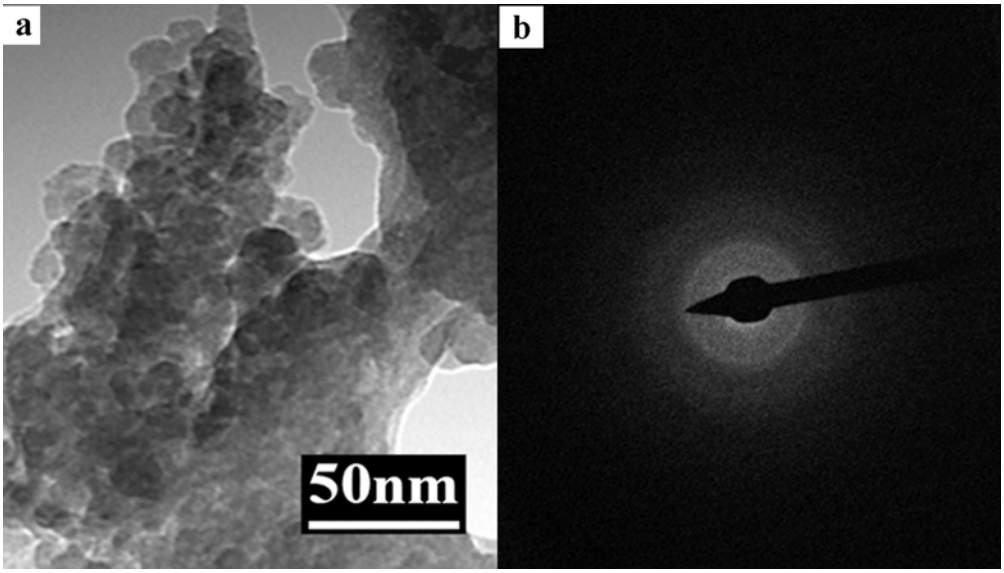

Figure 6.6. TEM image and Corresponding Selected Area Electron Diffraction (SAED) pattern of 3-day mineralized sample.

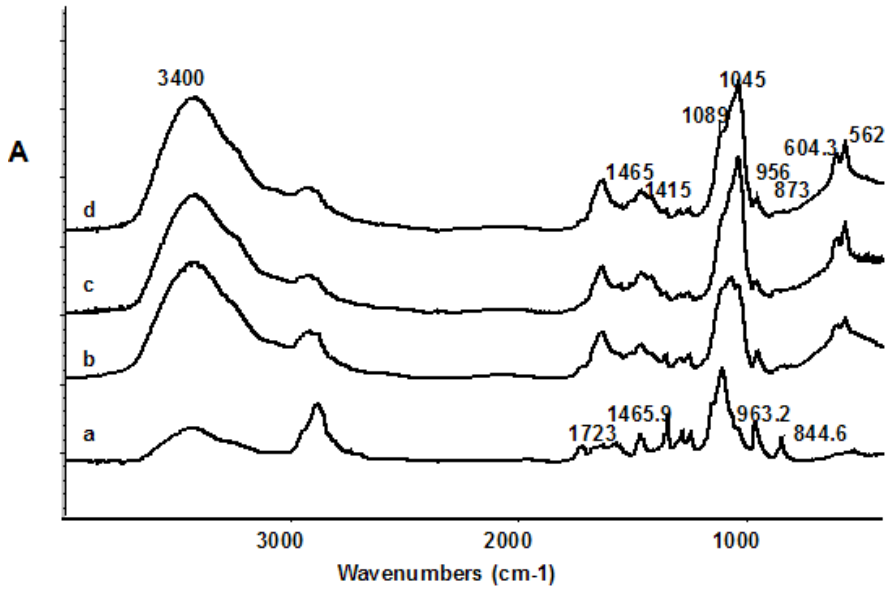

Figure 6.7. FTIR spectra of unmineralized and mineralized hydrogel samples with varied mineralization time: a) unmineralized control sample, b) 3-day mineralized sample, c) 7-day mineralized sample, d) 17-day mineralized sample.

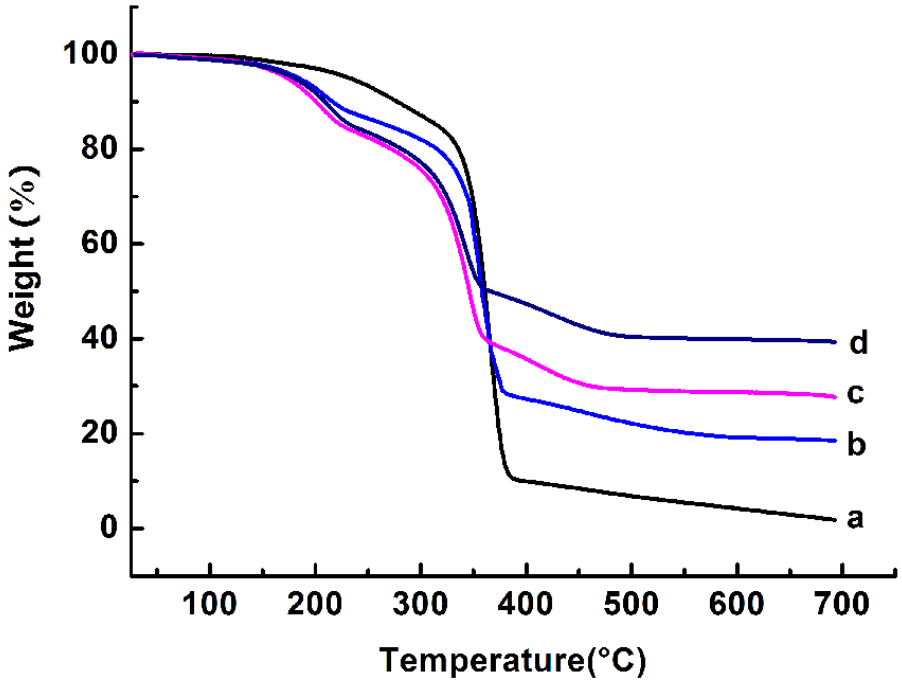

Figure 6.8. Thermogravimetric analysis (TGA) curves of unmineralized and mineralized hydrogel samples with varied mineralization time: a) unmineralized control sample, b) 3-day mineralized hydrogel sample, c) 7-day mineralized hydrogel sample, d) 17-day mineralized hydrogel sample.

The representative curves of thermogravimetric analysis of unmineralized and mineralized hydrogels were shown in Figure 6.8. For the unmineralized hydrogel, the major events of weight loss include the evaporation of occluded water at low temperature from 50-220°C, the decomposition of organic components from 220-380°C and burning of decomposed organic molecules from 380-700°C (Figure 6.8a). The weight of the unmineralized hydrogels when heated to 700°C was almost completely lost (98.2±0.5 %). Accordingly, inorganic phase primarily accounts for the remaining weight of mineralized hydrogels when heated to 700°C, albeit inorganic phase might also lose some weight during the heating process, as indicated by steeper slopes in the temperature zone between 360 and 450°C in the curves of mineralized

hydrogels (Figure 6.8c and d). Previous reports suggested the weight loss of carbonated apatite at this temperature range could be due to the condensation reaction of HPO_4^{2-} ions, as well as to the reaction between HPO_4^{2-} and CO_3^{2-} [26, 27]. Interestingly, the slope of the curve for 3-day mineralized sample in this temperature region is slightly different from those of 7 or 17-day samples. The difference probably arises from the fact that less HPO_4^{2-} substitute PO_4^{3-} in the poorly crystalline inorganic phase of 3-day mineralized sample, in consistence with a higher Ca/P ratio of the 3-day sample based on EDX analysis (Fig. 6.5a insert). We also noticed that the weight loss event at the organic decomposition region (in the temperature range between 300°C and 400°C) of the 7 and 17-day samples started and terminated at relatively lower temperatures than those of unmineralized and 3-day samples. This trend is probably in association with hydrolysis of the hydrogel in the SBF (for example: hydrolysis of any ester bonds in the hydrogels), as hydrolysis could result in less cross-linking densities of hydrogel network—thus lower temperature for the decomposition of organic components as mineralization progresses. Finally, based on the TGA data, we conclude that the amounts of inorganic phase in the mineralized hydrogel composites increases with immersion time in SBF, with the calculated weight mineral percentages (Formula S1-3, supporting information), 20.42±0.33%, 33.68±0.4% and 47.6±0.55 % for 3, 7 and 17-day mineralized samples, respectively (Table 6.2, supporting information).

In our control experiment without any pretreatments with $CaCl_2$ solution, we didn't observe any mineral deposition even after mineralization for 30 days due to the inhibition of mineral formation in the presence of large amount of carboxyl groups inside the gel network, in consistence with previous observations regarding the inhibition of mineral deposition in the presence of acidic polymers (e.g. non-woven fabric composed of carboxymethylated chitin) or carboxyl group-containing polymer

gels (e.g. carboxymethylated chitin cross-linked by divinyl sulfone) in SBF [19,20]. However, in our modified SBF mineralization procedures, we observed the presence of spherical ACP phase inside the porous hydrogels at an early mineralization stage (after 3-day mineralization) and crystalline apatite phase for 7-day and 17-day mineralized samples. These observations indicate that the pretreatment procedures allowed pre-binding of Ca^{2+} with carboxyl groups in the hydrogel networks, thus promoted the deposition of mineral phase inside the hydrogels. Furthermore, the unusual surface morphology (with spherical nanoparticles embedded in an organic-like matrix, Figure 6.5b, c) of the 3-day mineralized sample indicates that strong interactions might exist between the organic maleic chitosan/PEGDA hydrogel phase and the spherical-like inorganic phase, i.e., high-affinity adhesion. In contrast, when pure PEGDA hydrogels was used as control sample for mineralization study under the same mineralization conditions, no apparent deposition took place inside the hydrogel after 3-day mineralization. In fact, even after mineralization for 17 days, we could only occasionally observe very small amount of minerals randomly distributed inside PEGDA hydrogels (Figure 6.9).

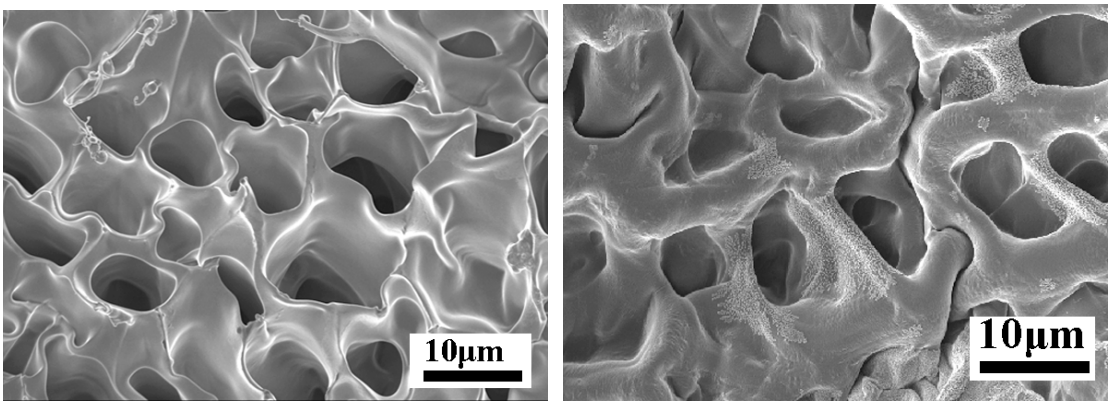

Figure 6.9. SEM images of PEGDA hydrogel (control sample, left) and PEGDA hydrogel after immersion in SBF for 17 days (right). Mineralization was only observed to be randomly deposited in some area of the gel surface.

These findings lead us to suggest that our polysaccharide-based scaffold may facilitate interactions/adhesions at the interfaces between organic and inorganic phases due to the functionalized surface chemistry (rich in carboxyl groups at the surface of hydrogels) under appropriate mineralization conditions and may also play important roles in mediating the formation and even the stabilization of amorphous spherical nanoparticles at the early stage. There are literatures describing that various negatively charged functional surfaces, fibers and/or polymers may favor the nucleation/ deposition of mineral phase and promote adhesions between inorganic and organic phase.

For example, Tanahashi et al. reported that negatively charged groups on self-assembled monolayers (SAMs) strongly induced apatite formation in SBF but the positively charged and uncharged groups did not [28]. Spoerke et al. used a gel network composed of peptide amphiphile nanofibers as a 3-D matrix for biomimetic mineralization study [29]. Functionally enriched in concentrated arrays of acidic and phosphorylated residues, the surfaces of nanofibers were believed to act as favorable sites for nucleation of hydroxyapatite [29]. Song et al. reported that carboxyl groups in pHEMA hydrogels through urea-mediated hydrolysis could act as mineral-binding ligands for calcium phosphate phase and afforded high-affinity integration of inorganic phase with pHEMA hydrogels, even though the mineralized hydrogels in their study did not display porous structures due to fast mineral deposition [3,15].

None of the studies cited above describe the formation of nano amorphous calcium phosphate phase despite the use of various negatively charged functional surfaces/templates. In contrast, our study found amorphous spherical nanoparticles were embedded inside the 3-day mineralized hydrogel in our study. We thus believe that not only the negatively charged moieties, but also the unique structure of polysaccharide-based hydrogel itself contribute importantly to the formation and

stabilization of amorphous phase in early stage. Note that we had previously observed that maleic chitosan could induce the formation of amorphous calcium carbonate films in our previous study [30]. It is also relevant that the stabilization of amorphous calcium phosphate in the early stage of bone mineralization is believed to be mediated by anionic macromolecules attached to collagen [31-33]. Finally, increasing evidence from biomineralization studies indicates that ACP phase might act as precursor phases for biogenic apatites, such as the fin bones of zebrafish [34] and the newly formed murine tooth enamel [35]. Accordingly, our *in vitro* mineralization study here might provide insight into biogenic mechanisms that form and stabilize the ACP phase.

6.5 Conclusions

Using a modified SBF mineralization approach, we have demonstrated that porous polysaccharide hydrogel-based composite materials with controlled mineral levels can be produced using maleic chitosan-PEGDA hydrogels as an organic matrix for the growth of minerals. We believe this is the first report using an acid polysaccharide-based hydrogel to template the growth of apatite-like inorganic phase. We suggest the our polysaccharide-based hydrogel not only promotes the deposition of mineral phase inside the 3D network under appropriate mineralization conditions, but also allows good interfacial interactions between organic and mineral phases, possibly by providing favorable reactive sites for mineral binding through the functionalized surface chemistry (carboxyl moieties). Furthermore, the polysaccharide component inside the hydrogel network may also play important roles in mediating the morphology, size and crystallinity of the inorganic nanophase. These observations also suggest a possible role of polysaccharides (primarily acid GAGs) in stabilizing the boundary between organic and mineral phase in natural bone. Finally, these studies suggest that polysaccharide macromolecules, particularly acid polysaccharides, may

prove to be excellent biomaterial scaffolds for the design of new useful bone-like biocomposites.

6.6 Acknowledgment

This project was partially supported by the graduate student thesis funds from the College of Human Ecology at Cornell University and the Morgan Tissue Engineering Program. This work made use of the electron microscopy (SEM and TEM) and XRD facilities of the Cornell Center for Materials Research (CCMR) with support from the National Science Foundation Materials Research Science and Engineering Centers (MRSEC) program (DMR 0520404).

APPENDIX

Determination of weight percentage of inorganic phase in mineralized gel samples based on calculations derived from TGA curves (shown below, the figure is the same as Figure 6.8.)

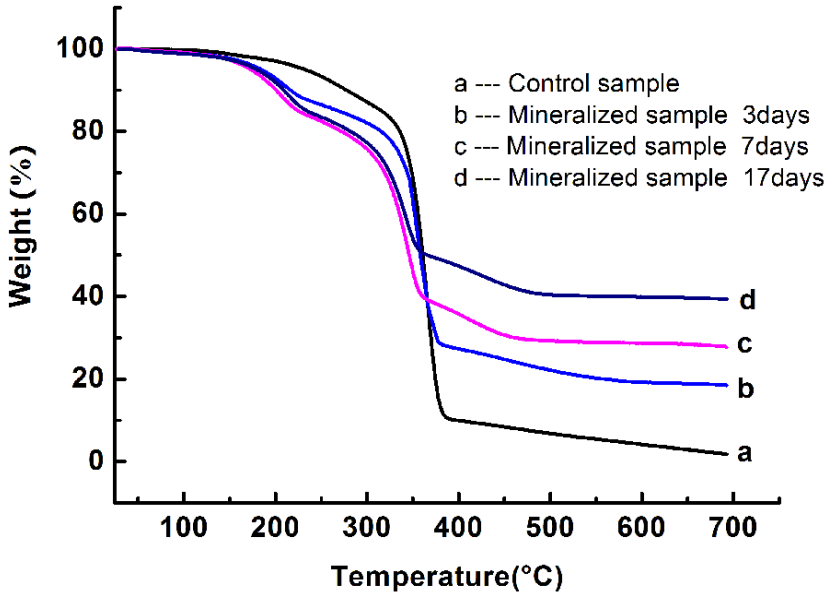

Table 6.2. Weight percentage of the samples at transition temperatures based on TGA curves shown in the above picture.

Samples	Control sample	Mineralized 3 days	Mineralized 7 days	Mineralized 17 days
Inflection point1(T_1)	220°C	220°C	220°C	220°C
Weight% at T_1	95.89%	89.3%	85.68%	87.29%
Inflection point 2 (T_2)	383°C	379°C	360°C	354°C
Weight% at T_2	11.39%	28.78%	40.07%	52.05%
T_3=700	700°C	700°C	700°C	700°C
Weight% at T_3	1.74%	18.45%	27.69%	39.32%
X		6.911%	5.209%	4.024%
Z		1.254%	0.939%	0.726%
Y		20.62%	33.92%	47.32%

Define X as: Weight loss percentage from organic part in mineralized sample in the temperature range between T_2~700°C).

Define Y as: Weight percentage of inorganic phase in the mineralized gel composite (Y);

Define Z as: Weight percentage of remaining organic part in mineralized sample when heated to 700°C.

We have the following formulas calculate X and Z:

$(W_{Control\ (T1)} - W_{Control\ (T2)})/ (W_{Control\ (T2)} - W_{Control\ (T3)}) = (W_{mineralized\ sample\ (T1)} - W_{mineralized\ sample\ (T2)} /X$; (Formula S1)

$(W_{Control\ (T1)} - W_{Control\ (T2)})/ (W_{mineralized\ sample\ (T1)} - W_{mineralized\ sample\ (T2)}) = 1.74\%/Z$; (Formula S2)

Based on the calculated X, Z values, we can calculate Y using the following formula:

$Y= (W_{Control\ (T2)} - X – Z)$ (Formula S3)

REFERENCES

1. Salgado AJ, Coutinho OP, Reis RL. Bone tissue engineering: State of the art and future trends. *Macromolecular Bioscience* 2004;4(8):743-765.

2. Wise ER, Maltsev S, Davies ME, Duer MJ, Jaeger C, Loveridge N, et al. The organic-mineral interface in bone is predominantly polysaccharide. *Chemistry of Materials* 2007;19(21):5055-5057.

3. Song J, Saiz E, Bertozzi CR. A new approach to mineralization of biocompatible hydrogel scaffolds: An efficient process toward 3-dimensional bonelike composites. *Journal of the American Chemical Society* 2003;125(5):1236-1243.

4. Boskey AL. Biomineralization: An overview. *Connective Tissue Research* 2003;44:5-9.

5. Boskey AL, Spevak L, Doty SB, Rosenberg L. Effects of bone CS-proteoglycans, DS-decorin, and DS-biglycan on hydroxyapatite formation in a gelatin gel. *Calcified Tissue International* 1997;61(4):298-305.

6. Boskey AL, Stiner D, Binderman I, Doty SB. Effects of proteoglycan modification on mineral formation in a differentiating chick limb-bud mesenchymal cell culture system. *Journal of Cellular Biochemistry* 1997;64(4):632-643.

7. Rees SG, Wassell DTH, Shellis RP, Embery G. Effect of serum albumin on glycosaminoglycan inhibition of hydroxyapatite formation. *Biomaterials* 2004;25(6):971-977.

8. Septier D, Hall RC, Lloyd D, Embery G, Goldberg M. Quantitative immunohistochemical evidence of a functional gradient of chondroitin 4-sulphate

dermatan sulphate, developmentally regulated in the predentine of rat incisor. *Histochemical Journal* 1998;30(4):275-284.

9. Takagi M, Maeno M, Yamada T, Miyashita K, Otsuka K. Nature and distribution of chondroitin sulphate and dermatan sulphate proteoglycans in rabbit alveolar bone. *Histochemical Journal* 1996;28(5):341-351.

10. Burg KJL, Porter S, Kellam JF. Biomaterial developments for bone tissue engineering. *Biomaterials* 2000;21(23):2347-2359.

11. Cui FZ, Li Y, Ge J. Self-assembly of mineralized collagen composites. *Materials Science & Engineering R-Reports* 2007;57(1-6):1-27.

12. Daculsi G, Pilet P, Cottrel M, Guicheux G. Role of fibronectin during biological apatite crystal nucleation: Ultrastructural characterization. *Journal of Biomedical Materials Research* 1999;47(2):228-233.

13. Hartgerink JD, Beniash E, Stupp SI. Self-assembly and mineralization of peptide-amphiphile nanofibers. *Science* 2001;294(5547):1684-1688.

14. Donners J, Nolte RJM, Sommerdijk N. Dendrimer-based hydroxyapatite composites with remarkable materials properties. *Advanced Materials* 2003;15(4):313-316.

15. Song J, Malathong V, Bertozzi CR. Mineralization of synthetic polymer scaffolds: A bottom-up approach for the development of artificial bone. *Journal of the American Chemical Society* 2005;127(10):3366-3372.

16. Palmer LC, Newcomb CJ, Kaltz SR, Spoerke ED, Stupp SI. Biomimetic Systems for Hydroxyapatite Mineralization Inspired By Bone and Enamel. *Chemical Reviews* 2008;108(11):4754-4783.

17. Kretlow JD, Mikos AG. Review: Mineralization of synthetic polymer scaffolds for bone tissue engineering. *Tissue Engineering* 2007;13(5):927-938.

18. Kokubo T, Takadama H. How useful is SBF in predicting in vivo bone bioactivity? *Biomaterials* 2006;27(15):2907-2915.

19. Kawashita M, Nakao M, Minoda M, Kim HM, Beppu T, Miyamoto T, et al. Apatite-forming ability of carboxyl group-containing polymer gels in a simulated body fluid. *Biomaterials* 2003 ;24(14):2477-2484.

20. Kokubo T, Hanakawa M, Kawashita M, Minoda M, Beppu T, Miyamoto T, et al. Apatite formation on non-woven fabric of carboxymethylated chitin in SBF. *Biomaterials* 2004;25(18):4485-4488.

21. Tadic D, Peters F, Epple M. Continuous synthesis of amorphous carbonated apatites. *Biomaterials* 2002;23(12):2553-2559.

22. Guicciardi S, Galassi C, Landi E, Tampieri A, Satou K, Pezzotti G. Rheological characteristics of slurry controlling the microstructure and the compressive strength behavior of biomimetic hydroxyapatite. *Journal of Material Research* 2001 16(1):163-170.

23. Chou YF, Chiou WA, Xu YH, Dunn JCY, Wu BM. The effect of pH on the structural evolution of accelerated biomimetic apatite. *Biomaterials* 2004;25(22):5323-5331.

24. Lowenstam HA, Weiner S. Transformation of Amorphous Calcium-Phosphate to Crystalline Dahllite in the Radular Teeth of Chitons. *Science* 1985;227(4682):51-53.

25. Gadaleta SJ, Paschalis EP, Betts F, Mendelsohn R, Boskey AL. Fourier transform infrared spectroscopy of the solution-mediated conversion of amorphous

calcium phosphate to hydroxyapatite: New correlations between X-ray diffraction and infrared data. *Calcified Tissue International* 1996;58(1):9-16.

26. Amjad Z, editor. *Calcium Phosphates in Biological and Industrial Systems*. Boston:Kluwer Academic Publishers, 1998.

27. Landi E, Tampieri A, Celotti G, Langenati R, Sandri M, Sprio S. Nucleation of biomimetic apatite in synthetic body fluids: dense and porous scaffold development. *Biomaterials* 2005;26(16):2835-2845.

28. Tanahashi, M. Matsuda, T. Surface functional group dependence on apatite formation on self-assembled monolayers in a simulated body fluid. *Journal of Biomedical Materials Research* 1997; 34(3): 305-315.

29. Spoerke ED, Anthony SG, Stupp SI. Enzyme Directed Templating of Artificial Bone Mineral. *Advanced Materials* 2009, 21(4):425-430.

30. Zhong, C.; Chu, C. C., Acid Polysaccharide-Induced Amorphous Calcium Carbonate (ACC) Films: Colloidal Nanoparticle Self-Organization Process. *Langmuir* 2009, 25, 3045-3049.

31. Boskey AL. Osteopontin and Related Phosphorylated Sialoproteins - Effects on Mineralization. *Annals of the New York Academy of Sciences* 1995;760:249-256.

32. Hunter GK, Goldberg HA. Modulation of Crystal-Formation by Bone Phosphoproteins - Role of Glutamic Acid-Rich Sequences in the Nucleation of Hydroxyapatite by Bone Sialoprotein. *Biochemical Journal* 1994;302:175-179.

33. George A, Bannon L, Sabsay B, Dillon JW, Malone J, Veis A, et al. The carboxyl-terminal domain of phosphophoryn contains unique extended triplet amino acid repeat sequences forming ordered carboxyl-phosphate interaction ridges that may

be essential in the biomineralization process. *Journal of Biological Chemistry* 1996, 271(51):32869-32873.

34. Mahamid, J.; Sharir, A.; Addadi, L.; Weiner, S. Amorphous calcium phosphate is a major component of the forming fin bones of zebrafish: Indications for an amorphous precursor phase. *Proceedings of the National Academy of Sciences of the United States of America* 2008, 105, 12748-12753.

35. Beniash, E.; Metzler, R. A.; Lam, R. S. K.; Gilbert, P. Transient amorphous calcium phosphate in forming enamel. *Journal of Structural Biology* 2009, 166, 133-143.

CHAPTER 7

CONCLUSIONS

As noted in the opening chapter, the research reported in this dissertation had two major goals: (1) to understand the roles of acid polysaccharide templates on $CaCO_3$ nucleation and growth; and (2) to build the foundation of new biomimetic materials to fabricate new bonelike biocomposites. The experimental designs used to pursue these goals were inspired by the strategies used by biological organisms to control mineralization. In particular, the use of polysaccharide macromolecules was based on recent observations regarding their roles in the formation of biominerals, including their possible roles in stabilizing the organic/inorganic interface in bone.

In pursuit of the first goal, calcium carbonate was grown in the presence of a soluble acid polysaccharide, maleic chitosan. The first step in this process was the synthesis of maleic chitosan, accomplished by chemically modifying chitosan, a partially deacetylated product of chitin, which is itself a biological macromolecule involved in many biominerals.

Although chitosan is typically resistant to chemical modification, because its hydrogen bonding renders it insoluble in common polar (e.g. DMSO) and unpolar (e.g. benzene) organic solvents, it was found that two chitosan salts (methanesulfonic and tolunesulfonic chitosan salts) are in fact soluble in formamide and DMSO, thereby permitting them to be used as precursors in the synthesis of maleic chitosan. These two chitosan salts were subsequently used to develop the blueprint to synthesize maleic chitosan with precisely controlled substitution of maleic anhydride on chitosan. The discovery and subsequent application of these two chitosan salts are significant because these chitosan salts may act as novel precursors permitting many other types

of chemical modifications, such as the α-amino acid NCA (N-carboxyanhydrides) ring opening reactions. In addition, it also provides a model for producing other precursors for the chemical modification of chitosan.

The second step in pursuit of the first goal was to achieve biomimetic growth of calcium carbonate using the soluble maleic chitosan as the template via classical ammonium carbonate diffusion. This acid polysaccharide had a significant influence on the growth and morphology of calcium carbonate, particularly in the early stage of crystallization at a high supersaturation of $CaCO_3$.

Two major findings emerged from this crystallization study. First, it demonstrated that amorphous calcium carbonate (ACC) films can be produced and stabilized in the presence of maleic chitosan. The direct deposition of the ACC films onto TEM grids revealed that the ACC films were formed through a colloid nanoparticle self-organization process and that nanoparticles less than 10 nm were responsible for this self-organization. These findings provide insights into the general formation mechanism of ACC films obtained in other additive/ template systems and may contribute to the understanding of the stabilization of ACC phase in biological systems.

Second, special etching techniques revealed that amorphous cores (ACC cores) were always located inside biomimetic polycrystalline calcium carbonate spherulites. In addition, the resulting crystals possess combined structure features from two independent types of $CaCO_3$ biominerals: the coexistence of calcite and ACC of composite skeletal elements and the radially-ordered structure of spherulitic biominerals in nature. Moreover, calcium carbonate spherulites are formed through a two-step crystallization process with the formation of ACC films at the very early stage followed by the growth of needle-like calcite subunits that start from the center of the ACC films. Collectively, these findings suggest that ACC cores are a necessary

initial phase in the crystallization of biomimetic $CaCO_3$ spherulites, possibly acting as nuclei for crystallization. This new function goes beyond the previously known functions of both biogenic and synthetic ACC phases. These findings, in conjunction with previous studies of spherulites in plants and animals, raise the possibility that amorphous cores might be a common but frequently overlooked phenomenon in spherulites. Therefore, the findings in this study provide new insights into the formation of spherulites in nature, particularly spherulitic biominerals. They may also have important implications for the understanding and eventual treatment of diseases such as Alzheimer's and kidney stones in which amorphous cores have been observed. Finally, this study offers a novel view on the mechanism of non-classical (unconventional) crystallization.

As stated above, the second goal of this dissertation was to build the foundation of new biomimetic materials to fabricate new bonelike biocomposites for potential applications in bone engineering. To this end, this dissertation reports on the use of a polysaccharide-based hydrogel as a 3D template for biomimetic synthesis of carbonated apatite.

The first step was the preparation and characterization of a biocompatible and biodegradable hydrogel, maleic chitosan/PEGDA hydrogel, using aqueous-based UV-photopolymerization. The 3D microporous hydrogel templates were then used for the fabrication of carbonated apatite using a modified simulated body fluid (SBF) biomineralization technique. The results demonstrate the fabrication of porous bonelike polysaccharide-based biocomposites with tunable weight contents of inorganic phase.

Further observations revealed that the mineral phase of the composite consisted of amorphous calcium phosphate spherical nanoparticles embedded inside the surrounding organic maleic chitosan/PEGDA hydrogel layers at the end of 3-day

biomimetic mineralization. The mineral phase became plate-like, calcium-deficient, carbonated-substituted crystalline hydroxyapatite after 7-day mineralization (including both 7 day and 17 day samples). In contrast, only very small amounts of mineral phase were found randomly deposited inside the pure PEGDA hydrogel control even after 17-day mineralization. These data suggest that maleic chitosan-based hydrogel not only promotes the deposition of mineral phase inside the 3D network under appropriate mineralization conditions, but also allows good interfacial interactions between organic and mineral phases, possibly by providing favorable reactive sites for mineral binding through the carboxyl moieties in maleic chitosan segments. Furthermore, the maleic chitosan polysaccharide component inside the hydrogel network may also play an important role in the formation and stabilization of amorphous calcium phosphate (ACP) at an early stage.

This *in vitro* mineralization study might provide a clue into biogenic mechanisms in forming and stabilizing the ACP phase. Moreover, it implies that polysaccharide macromolecules, particularly acid polysaccharides like maleic chitosan, could be the potential scaffolds for the design of new bonelike biocomposites.